NTNU – Trondheim
Norwegian University of
Science and Technology

Numerical Modelling of the Optical Properties of Truncated and Coated Prolate Spheroidal Nanoparticles

Sindre Vegard Stavseng

Master of Science in Physics and Mathematics
Submission date: June 2013
Supervisor: Ingve Simonsen, IFY

Norwegian University of Science and Technology
Department of Physics

Abstract

The optical properties of an island film of truncated and coated prolate spheroidal particles are studied numerically by implementing support for this island geometry in the GranFilm software. The underlying theory of the calculations is based on the work on optical properties of surfaces by Bedeaux and Vlieger. The implementation is tested numerically and compared in the appropriate limits to earlier implementations of other geometries. The tests show that the implementation was carried out successfully. Finally, the GranFilm software is used to study and characterize the plasmonic resonance modes of various supported metallic islands. This includes the observation of plasmonic hybridization in a truncated metallic nanoshell.

Sammendrag

I dette arbeidet blir de optiske egenskapene til en film av trunkerte, prolate sfæroidiske nanopartikler med coating regnet ut numerisk ved å implementere støtte for denne geometrien i software-pakken GranFilm . Teorien bak disse beregningene er basert på arbeidet rundt optiske egenskaper til overflater av Bedeaux og Vlieger. Implementasjonen testes så numerisk og sammenlignes med andre geometrier i de relevante grensene. Disse testene viser at implementasjonen kan sies å være vellykket. Avslutningsvis anvendes programmet til å studere og karakterisere de plasmoniske resonansmodene til ulike typer metall-øyer på et substrat. Dette inkluderer blant annet observasjonen av plasmonisk hybridisering i et trunkert metallisk nanoskall.

Preface

This Master's thesis is the final part of the five-year MSc. programme Applied Physics and Mathematics at the Norwegian University of Science and Technology (NTNU) in Trondheim. My specialization has been in Applied Physics. The work in this thesis was carried out during the spring semester of 2013, with Professor Ingve Simonsen at the Department of Physics, NTNU, as supervisor.

This work has given me the opportunity to delve into an interesting branch of physics, and also given me experience in programming and numerics, which has been very educative. A big part of this work has consisted of programming and debugging, of which details are not included in this report. Some mathematical details on the implementation and testing of the program are, however, included. For anyone interested in the specifics of the GRANFILM implementation, the source code is freely available.

The work in this Master's thesis has been a continuation of my Specialization project [1] from the fall of 2012. For completeness, parts of the report from this project are therefore included in this thesis. In fact, the chapters 2–5 in this report are only slightly modified versions of the same chapters in [1].

I would like to thank my supervisor, Professor Ingve Simonsen, for his valuable advice and guidance, as well as for many interesting discussions, throughout this work.

Sindre Stavseng,
Trondheim, June 2013.

Contents

1. Introduction

Optical properties of thin films and rough surfaces has long been a field of great scientific interest. In particular, supported metallic nanostructures have recently received a lot of attention due to their characteristic optical properties in the visible range.

A common application which exploits these properties is the optical monitoring and characterization of thin-film growth [2, 3]. Such films are often produced by depositing material on a substrate in vacuum conditions. If the substrate is poorly wetted by the material, three-dimensional clusters, or islands, are formed in a so-called Volmer-Weber growth mode [2]. Optical methods can be advantageous when monitoring such growth, because of their non-disturbing nature and the possibility of *in situ*[1] and real-time measurements. Other surface probing techniques often involve charged particles, which may disturb the particle growth, or other more practical issues which make it difficult to perform the measurements *in situ* or in real-time [2].

The optical measurement often used in these techniques is called Surface Differential Reflectance Spectroscopy (SDRS) [3], which is performed by measuring the difference in reflectance between the bare and coated substrate for different wavelengths in and around the visible range. The SDR spectrum is also denoted by $\Delta R/R$.

For the case of island films, the wavelengths of the visible light (380–740 nm) can be more than two orders of magnitude longer than the size of a typical island (around 2–20 nm). One does therefore not immediately expect the light to be able to resolve the structure of the islands, due to the diffraction limit of visible light. Although this is true for imaging, it turns out that it is still possible to extract information about the the size and shape of the islands from their optical properties. This is due to so-called *plasmon resonances*, which arise from oscillations in the charge density of the islands when they are subjected to an external field. The energies at

---

[1] In place, during the process.

which these resonances occur depend on the dielectric properties of the islands, but are also highly sensitive to their size and shape. This can be utilized in the characterization of the islands.

In recent years, this ability to study metallic nanostructures using light in and around the visible frequency range has gained a lot of attention, and is now often referred to as the field of *plasmonics* or *nanoplasmonics*. This is in part due to the interesting physics of plasmonic interactions, but can also be attributed to the wide range of applications which exploit these properties. Some examples of such applications are new methods of spectroscopy [4] and biomedical applications ranging from home pregnancy tests [5] and other advanced biosensors [6] to possible cancer treatments [4].

In the 1970's Bedeaux and Vlieger [7], developed a model for the optical properties of boundary layers on a surface, where the thickness of a layer is small compared to the wavelength of the incident light. This model is particularly useful for island films, and improved upon the earlier models, like the one introduced by Maxwell Garnett at the turn of the nineteenth century [7]. The Bedeaux-Vlieger model introduces *effective boundary conditions* dependent on so-called *surface susceptibilities*. These determines the far-field behaviour of the electromagnetic field, and lets one calculate the optical properties of the surface without knowing the exact behaviour of the fields close to the surface.

GranFilm [8] is a software package developed by I. Simonsen and R. Lazzari, which calculates the optical properties of island films (or *granular* films) by modelling the particle clusters as spherical or spheroidal islands and applying the Bedeaux-Vlieger model. An example of the use of this software can be seen in Fig. 1.1, where a film of silver islands is supported on a MgO substrate. The surface differential reflectance spectrum (SDRS) is calculated and compared to the measured spectrum of the sample. The resulting curve can be seen in Fig. 1.1b. The peak and the valley in the spectrum are due to the plasmon excitations, and their positions on the energy axis are highly dependent on the shapes and sizes of the islands.

The software currently includes the possibility of modelling the clusters as spherical or oblate spheroidal particles, truncated by the substrate. Additionally, the particles may also have an arbitrary number of coating layers. One example where such a coating layer is relevant is the case of a film of metallic islands that have been exposed to oxygen, and where an oxide layer has been built up on the surface of the islands. Another

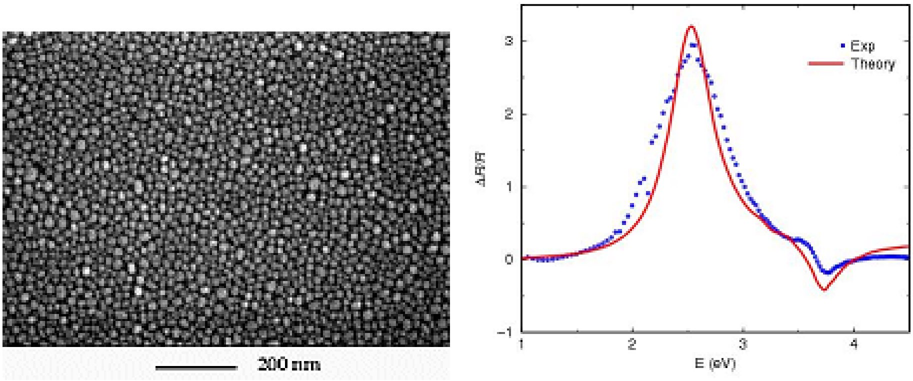

(a)

(b)

Figure 1.1: (a) A granular film of silver islands on a substrate of magnesium oxide. (b) The differential reflectance of the surface as calculated using GranFilm and measured in an experiment. Pictures taken from [8].

case where this could be useful is for metallic nano-shells, which have been found to have many interesting properties [9].

One particle shape which is currently not supported in GranFilm is truncated prolate spheroidal islands with coating layers. After deriving the set of equations for the potential multipole expansion in this geometry in my specialization project [1], it is now the subject of this thesis to implement, test and apply this functionality in GranFilm. In particular, the goals of this thesis can be stated as follows:

- Implement numerically the equations derived in [1] for the optical properties of truncated and coated prolate spheroidal island films into the existing GranFilm 2.0 framework.
- Test the implementation in the appropriate limits, in order to ensure that it is correct.
- Use the GranFilm software to study the resonance modes of various spheroidal and spherical island films in detail.

In his MSc. thesis the spring of 2012, E. Aursand developed the corresponding equations for the case of coated and truncated *oblate* spheroids, and implemented these results in GranFilm. For consistency, many of the same numerical tests as used in his thesis, were also used in this work in order to verify the correctness of the implementation.

Roughly speaking, this report consists of two parts. The first part, chapters 2–5, covers some theoretical background and the analytical derivation of the optical properties of truncated and coated prolate spheroidal island films. These chapters are slightly edited versions of the same chapters in [1], and are included here for the sake of completeness. An exception is the new section 2.3, which covers some theory on plasmonics. The second part consists of chapters 6–8. Specifically, chapter 6 covers the implementation and the subsequent testing of the new functionality in the GranFilm software, while chapter 7 covers the modelling and characterization of the plasmonic resonance modes of various island films. Chapter 8 contains a summary of the results and some concluding remarks.

In addition to this, some technical details of the implementation are included in the Appendices. These can hopefully serve as helpful supplements to anyone interested in doing further work on the new parts of the GranFilm source code.

2. Background

In this chapter, the theory for calculating optical properties of granular films, as developed by Bedeaux and Vlieger [7], will be presented. In this model the non-flat surface is treated as a perturbation to the simple case of a flat interface between two media. The perturbation is introduced in a formalism called *excess quantities* which leads to a set of *effective boundary conditions* for the surface region.

For completeness a short recapitulation of the optical properties of flat surfaces is included in section 2.1. In section 2.2, the theory of non-sharp interfaces is presented. In section 2.3, the field of *plasmonics* is introduced and discussed briefly. This is later used to describe the resonance phenomena observed in granular thin films.

2.1. Optical properties of a sharp interface

In the simplest form, a surface can be seen as a flat discontinuity between two media with different electric and magnetic properties. An example of such a sharp interface can be seen in Figure 2.1, where light incident on the interface between two different media (denoted by + and −) is partly reflected and partly transmitted. The relations between the incident, reflected and transmitted parts of the wave is what we call the optical properties of this particular surface.

The starting point when finding these relations is Maxwell's equations [10]

$$\begin{aligned} \boldsymbol{\nabla}\cdot\mathbf{D} &= \rho_f, & \boldsymbol{\nabla}\times\mathbf{E} &= -\frac{\partial\mathbf{B}}{\partial t}, \\ \boldsymbol{\nabla}\cdot\mathbf{B} &= 0, & \boldsymbol{\nabla}\times\mathbf{H} &= \mathbf{J}_f + \frac{\partial\mathbf{D}}{\partial t}, \end{aligned} \tag{2.1}$$

where $\mathbf{E}$ is the electric field, $\mathbf{B}$ is the magnetic induction, $\mathbf{D}$ is the electric displacement field, $\mathbf{H}$ is the magnetic field, ρ_f is the free charge and $\mathbf{J}_f$ is the free current. From these equations a set of boundary conditions for

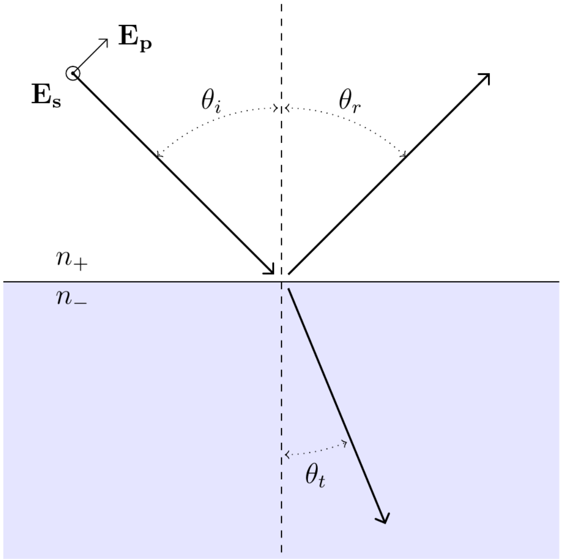

Figure 2.1: A light beam is partly transmitted and partly reflected on an interface between two media with refractive indices n_+ and n_-. Note the two possible orientations of the electric field vector $\mathbf{E}$, corresponding to s- and p-polarized light.

the interface between two media can be found [10]

$$\begin{aligned} D_+^\perp = D_-^\perp, \quad \mathbf{E}_+^{\|} = \mathbf{E}_-^{\|}, \\ B_+^\perp = B_-^\perp, \quad \mathbf{H}_+^{\|} = \mathbf{H}_-^{\|}, \end{aligned} \tag{2.2}$$

where the subscript + or − denotes the field just above or just below the interface, respectively. The superscript ⊥ denotes the component normal to the surface, while || denotes the tangential component.

From the boundary conditions the relation between the amplitudes of the incident and transmitted wave (t), and between the amplitudes of the incident and reflected wave (r), can be found. These relations are called the *Fresnel coefficients*, and are given by [10]

$$\begin{aligned} r_s &= \frac{n_+ \cos\theta_i - n_- \cos\theta_t}{n_+ \cos\theta_i + n_- \cos\theta_t} \\ t_s &= \frac{2n_+ \cos\theta_i}{n_+ \cos\theta_i + n_- \cos\theta_t} \\ r_p &= \frac{n_- \cos\theta_i - n_+ \cos\theta_t}{n_+ \cos\theta_t + n_- \cos\theta_i} \\ t_p &= \frac{2n_+ \cos\theta_i}{n_+ \cos\theta_t + n_- \cos\theta_i}. \end{aligned} \tag{2.3}$$

Here n_+ and n_- are the refractive indices of medium + and medium −, respectively, θ_i is the angle of incidence, θ_r is the angle of reflection and θ_t is the angle of transmission. See Figure 2.1 for an illustration. From the same derivation, the laws of reflection and refraction (also known as Snell's law) are found:

$$\begin{aligned} \theta_i &= \theta_r \\ n_+ \sin\theta_i &= n_- \sin\theta_r. \end{aligned} \tag{2.4}$$

The subscripts s and p of the reflection and transmission coefficients in Eq. (2.3) denote the two possible orientations of the electric field $\mathbf{E}$ in the incident light. In the case that $\mathbf{E}$ lies in the plane defined by the incident and reflected wave vectors, we have so-called p-polarized light (from *parallel*). If $\mathbf{E}$ is directed normal to this plane, *i.e.* parallel to the surface, we have s-polarization (from the German word for orthogonal, *senkrecht*). See Figure 2.1 for an illustration of s- and p-polarization.

2.2. Optical properties of non-sharp interfaces

Calculation of the electromagnetic field close to the surface of a non-sharp interface quickly becomes very complex. It is therefore in general not possible to calculate the Fresnel coefficients of such a surface directly as done in the previous section. Using the formalism of Bedeaux and Vlieger, however, one can find expressions for these coefficients, and thus the macroscopic optical properties of the interface, without having exact knowledge about the electromagnetic fields close to the surface.

2.2.1. Excess fields and effective boundary conditions

An *excess* of a field is defined as the difference between the real fields and the bulk fields extrapolated to the surface. For the electric field $\mathbf{E}$, the excess field can be written as

$$\mathbf{E}_{\text{ex}}(\mathbf{r},t) = \mathbf{E}(\mathbf{r},t) - \mathbf{E}^{-}(\mathbf{r},t)\theta(-z) - \mathbf{E}^{+}(\mathbf{r},t)\theta(z) \tag{2.5}$$

where $\mathbf{E}$ is the actual field and $\mathbf{E}^{\pm}$ are the fields in the bulk regions above $(+)$ and below $(-)$ the surface, extrapolated to the surface at $z = 0$. The fields are cut off using the Heaviside unit step function, denoted by $\theta(z)$. It is clear from the definition that the excess fields are only significantly different from zero in the region close to the surface, since $\mathbf{E}(\mathbf{r}) = \mathbf{E}^{\pm}(\mathbf{r})$ as $z \to \pm\infty$. Excesses of other quantities are defined in the same way.

Inserting Eq. (2.5) and its equivalents into the Maxwell equations (2.1), we get the following equations for the excess fields

$$\begin{aligned}
\boldsymbol{\nabla} \times \mathbf{E}_{\text{ex}}(\mathbf{r},t) + \hat{\mathbf{z}} \times \Big[\mathbf{E}_{\|}^{+}(\mathbf{r}_{\|},t) - \mathbf{E}_{\|}^{-}(\mathbf{r}_{\|},t)\Big]_{z=0}\delta(z) & \\
= -\frac{\partial}{\partial t}\mathbf{B}_{\text{ex}}(\mathbf{r},t) & \qquad (2.6\text{a}) \\
\boldsymbol{\nabla} \cdot \mathbf{D}_{\text{ex}}(\mathbf{r},t) + \Big[D_z^{+}(\mathbf{r}_{\|},t) - \Big[D_z^{-}(\mathbf{r}_{\|},t)\Big]_{z=0}\delta(z) = \rho_{\text{ex}}(\mathbf{r},t) & \qquad (2.6\text{b}) \\
\boldsymbol{\nabla} \times \mathbf{H}_{\text{ex}}(\mathbf{r},t) + \hat{\mathbf{z}} \times \Big[\mathbf{H}_{\|}^{+}(\mathbf{r}_{\|},t) - \mathbf{H}_{\|}^{-}(\mathbf{r}_{\|},t)\Big]_{z=0}\delta(z) & \\
= \frac{\partial}{\partial t}\mathbf{D}_{\text{ex}}(\mathbf{r},t) + \mathbf{J}_{\text{ex}}(\mathbf{r},t) & \qquad (2.6\text{c}) \\
\boldsymbol{\nabla} \cdot \mathbf{B}_{\text{ex}}(\mathbf{r},t) + \Big[B_z^{+}(\mathbf{r}_{\|},t) - \Big[B_z^{-}(\mathbf{r}_{\|},t)\Big]_{z=0}\delta(z) = 0. & \qquad (2.6\text{d})
\end{aligned}$$

The subscript $\|$ indicates the projection of a vector into the xy-plane, while the subscript z means the z-component of the vector. The vector $\hat{\mathbf{z}}$ is the unit vector normal to the dividing reference surface, which is defined as $z = 0$. It has also been used that $\nabla\theta(z) = \delta(z)$. By integrating Eq. (2.6) along the z-axis, we get the following boundary conditions for the fields in the bulk media, extrapolated to the reference surface

$$\Big[E_x^+(\mathbf{r}_\parallel,t) - E_x^-(\mathbf{r}_\parallel,t)\Big]_{z=0} = \frac{\partial}{\partial x}E_z^s(\mathbf{r}_\parallel,t) - \frac{\partial}{\partial t}B_y^s(\mathbf{r}_\parallel,t) \tag{2.7a}$$

$$\Big[E_y^+(\mathbf{r}_\parallel,t) - E_y^-(\mathbf{r}_\parallel,t)\Big]_{z=0} = \frac{\partial}{\partial y}E_z^s(\mathbf{r}_\parallel,t) + \frac{\partial}{\partial t}B_x^s(\mathbf{r}_\parallel,t) \tag{2.7b}$$

$$\Big[D_z^+(\mathbf{r}_\parallel,t) - D_z^-(\mathbf{r}_\parallel,t)\Big]_{z=0} = -\boldsymbol{\nabla}_\parallel \cdot \mathbf{D}_\parallel^s(\mathbf{r}_\parallel,t) + \rho^s(\mathbf{r}_\parallel,t) \tag{2.7c}$$

$$\begin{aligned}\Big[H_x^+(\mathbf{r}_\parallel,t) - H_x^-(\mathbf{r}_\parallel,t)\Big]_{z=0} &= \frac{\partial}{\partial x}H_z^s(\mathbf{r}_\parallel,t) \\ &\quad + \frac{\partial}{\partial t}D_y^s(\mathbf{r}_\parallel,t) + J_y^s(\mathbf{r}_\parallel,t)\end{aligned} \tag{2.7d}$$

$$\begin{aligned}\Big[H_y^+(\mathbf{r}_\parallel,t) - H_y^-(\mathbf{r}_\parallel,t)\Big]_{z=0} &= \frac{\partial}{\partial y}H_z^s(\mathbf{r}_\parallel,t) \\ &\quad - \frac{\partial}{\partial t}D_x^s(\mathbf{r}_\parallel,t) - J_x^s(\mathbf{r}_\parallel,t)\end{aligned} \tag{2.7e}$$

$$\Big[B_z^+(\mathbf{r}_\parallel,t) - B_z^-(\mathbf{r}_\parallel,t)\Big]_{z=0} = -\boldsymbol{\nabla}_\parallel \cdot \mathbf{B}_\parallel^s(\mathbf{r}_\parallel,t). \tag{2.7f}$$

The superscript s indicates a *total excess quantity*, *i.e.* that an excess quantity has been integrated along the entire z-axis. The operator

$$\boldsymbol{\nabla}_\parallel = \left[\frac{\partial}{\partial x}, \frac{\partial}{\partial y}\right] \tag{2.8}$$

is the gradient operator in the xy-plane, while $\mathbf{r}_\parallel = [x, y]$ is the position vector in the xy-plane. The boundary conditions in Eq. (2.7) can be viewed as the *effective boundary conditions* for the fields in the bulk media far away from the surface.

In order to relate these boundary conditions to the physical properties of the surface, polarization and magnetization densities can be introduced. The total excess polarization and magnetization densities are given by [7]

$$\mathbf{P}^s(\mathbf{r}_\parallel,t) \equiv \Big[\mathbf{D}_\parallel^s(\mathbf{r}_\parallel,t), -\varepsilon_0 E_z^s(\mathbf{r}_\parallel,t)\Big] \tag{2.9}$$

and

$$\mathbf{M}^s(\mathbf{r}_\parallel,t) \equiv \Big[\frac{1}{\mu_0}\mathbf{B}_\parallel^s(\mathbf{r}_\parallel,t), -H_z^s(\mathbf{r}_\parallel,t)\Big], \tag{2.10}$$

respectively. The superscript s again indicates a *total excess*. Here ε_0 and μ_0 are the electric permittivity and magnetic permeability of vacuum, respectively. It should be noted that these total excesses are the proper expressions for the surface polarization and magnetization in every particular surface system, and can not be obtained by integrating some excess polarization or magnetization along the z-axis [7].

The effective boundary conditions in Eq. (2.7) can now be rewritten in terms of the total excess surface polarization and magnetization densities in Eqs. (2.9) and (2.10):

$$\begin{aligned}
\Big[\mathbf{E}_{\parallel}^{+}(\mathbf{r}_{\parallel},t) - \mathbf{E}_{\parallel}^{-}(\mathbf{r}_{\parallel},t)\Big]_{z=0} &= \mu_0 \hat{\mathbf{z}} \times \frac{\partial}{\partial t}\mathbf{M}_{\parallel}^{s}(\mathbf{r}_{\parallel},t) \\
&\quad - \frac{1}{\varepsilon_0}\boldsymbol{\nabla}_{\parallel} P_z^{s}(\mathbf{r}_{\parallel},t) && \text{(2.11a)} \\
\Big[D_z^{+}(\mathbf{r}_{\parallel},t) - D_z^{-}(\mathbf{r}_{\parallel},t)\Big]_{z=0} &= \rho^{s}(\mathbf{r}_{\parallel},t) - \boldsymbol{\nabla}_{\parallel}\cdot\mathbf{P}_{\parallel}^{s}(\mathbf{r}_{\parallel},t) && \text{(2.11b)} \\
\Big[\mathbf{H}_{\parallel}^{+}(\mathbf{r}_{\parallel},t) - \mathbf{H}_{\parallel}^{-}(\mathbf{r}_{\parallel},t)\Big]_{z=0} &= -\,\hat{\mathbf{z}} \times \mathbf{J}_{\parallel}^{s}(\mathbf{r}_{\parallel},t) - \boldsymbol{\nabla}_{\parallel} M_z^{s}(\mathbf{r}_{\parallel},t) \\
&\quad - \hat{\mathbf{z}} \times \frac{\partial}{\partial t}\mathbf{P}_{\parallel}^{s}(\mathbf{r}_{\parallel},t) && \text{(2.11c)} \\
\Big[B_z^{+}(\mathbf{r}_{\parallel},t) - B_z^{-}(\mathbf{r}_{\parallel},t)\Big]_{z=0} &= -\,\mu_0\boldsymbol{\nabla}_{\parallel}\cdot\mathbf{M}_{\parallel}^{s}(\mathbf{r}_{\parallel},t). && \text{(2.11d)}
\end{aligned}$$

Notice that if all current and charge densities on the interface are zero, as well as the surface polarization and magnetization densities, these boundary conditions reduce to those for a sharp interface defined in Eq. (2.2), as they should.

In time-dependent problems it can often be convenient to introduce a *generalized electric displacement field*, defined in terms of the Fourier transformed displacement field and current density as

$$\mathbf{D}'(\mathbf{r},\omega) \equiv \mathbf{D}(\mathbf{r},\omega) + \frac{i}{\omega}\mathbf{J}(\mathbf{r},\omega), \tag{2.12}$$

where ω is the frequency. The surface polarization density can now also be written in generalized form as

$$\mathbf{P}'^{s}(\mathbf{r}_{\parallel},\omega) \equiv \Big[\mathbf{D}'^{s}_{\parallel}(\mathbf{r}_{\parallel},\omega), -\varepsilon_0 E_z^{s}(\mathbf{r}_{\parallel},\omega)\Big]. \tag{2.13}$$

By Fourier transforming Eq. (2.11) and using conservation of charge, which can be written in the frequency domain as

$$i\omega\rho(\mathbf{r},\omega) = \boldsymbol{\nabla}\mathbf{J}(\mathbf{r},\omega), \tag{2.14}$$

the boundary conditions can now be rewritten using Eq. (2.13):

$$\begin{aligned}
\Big[\mathbf{E}_{\parallel}^{+}(\mathbf{r}_{\parallel},\omega) - \mathbf{E}_{\parallel}^{-}(\mathbf{r}_{\parallel},\omega)\Big]_{z=0} &= -\, i\omega\mu_0\hat{\mathbf{z}}\times\mathbf{M}_{\parallel}^{s}(\mathbf{r}_{\parallel},\omega) \\
&\quad -\frac{1}{\varepsilon_0}\boldsymbol{\nabla}_{\parallel}P'^{s}_{z}(\mathbf{r}_{\parallel},\omega) && \text{(2.15a)}\\
\Big[D_z^{+}(\mathbf{r}_{\parallel},\omega) - D_z^{-}(\mathbf{r}_{\parallel},\omega)\Big]_{z=0} &= -\,\boldsymbol{\nabla}_{\parallel}\cdot\mathbf{P}'^{s}_{\parallel}(\mathbf{r}_{\parallel},\omega) && \text{(2.15b)}\\
\Big[\mathbf{H}_{\parallel}^{+}(\mathbf{r}_{\parallel},\omega) - \mathbf{H}_{\parallel}^{-}(\mathbf{r}_{\parallel},\omega)\Big]_{z=0} &= i\omega\hat{\mathbf{z}}\times\mathbf{P}'^{s}_{\parallel}(\mathbf{r}_{\parallel},\omega) - \boldsymbol{\nabla}_{\parallel}M_z^{s}(\mathbf{r}_{\parallel},\omega) && \text{(2.15c)}\\
\Big[B_z^{+}(\mathbf{r}_{\parallel},\omega) - B_z^{-}(\mathbf{r}_{\parallel},\omega)\Big]_{z=0} &= -\,\mu_0\boldsymbol{\nabla}_{\parallel}\cdot\mathbf{M}_{\parallel}^{s}(\mathbf{r}_{\parallel},\omega). && \text{(2.15d)}
\end{aligned}$$

In the following the notation will be simplified by dropping the primes, and **D** and **P** will now denote the generalized displacement field and the generalized surface polarization density, respectively.

2.2.2. Constitutive relations

In order for these boundary conditions to have any practical use, we need relations characteristic of the surface that link the interfacial polarization and magnetization densities, $\mathbf{P}^s(\mathbf{r}_{\parallel},\omega)$ and $\mathbf{M}^s(\mathbf{r}_{\parallel},\omega)$, and the bulk fields extrapolated to the surface. These *constitutive relations* are in the case of no spatial dispersion given by [7]

$$\mathbf{P}^s(\mathbf{r}_{\parallel},\omega) = \xi_{\mathbf{e}}^{\mathbf{s}}(\omega)\cdot\Big[\bar{\mathbf{E}}_{\parallel}(\mathbf{r}_{\parallel},\omega), \bar{D}_z(\mathbf{r}_{\parallel},\omega)\Big] \tag{2.16a}$$

$$\mathbf{M}^s(\mathbf{r}_{\parallel},\omega) = \xi_{\mathbf{m}}^{\mathbf{s}}(\omega)\cdot\Big[\bar{\mathbf{H}}_{\parallel}(\mathbf{r}_{\parallel},\omega), \bar{B}_z(\mathbf{r}_{\parallel},\omega)\Big]. \tag{2.16b}$$

Here $\xi_{\mathbf{e,m}}^{\mathbf{s}}(\omega)$ are *constitutive tensors* and the bar indicates that the average of the two corresponding extrapolated fields over the dividing surface ($z = 0$) should be used. For an arbitrary field a, this average is simply

$$\bar{a}(\mathbf{r}_{\parallel},\omega) \equiv \frac{1}{2}\Big[a^{-}(\mathbf{r}_{\parallel},\omega)|_{z=0} + a^{+}(\mathbf{r}_{\parallel},\omega)|_{z=0}\Big] \tag{2.17}$$

In the case of an isotropic, homogeneous and symmetric interface, the constitutive tensor for the polarization is given by [7, 3]

$$\xi_{\mathbf{e}}^{\mathbf{s}}(\omega) = \begin{bmatrix} \gamma_e(\omega) & 0 & 0 \\ 0 & \gamma_e(\omega) & 0 \\ 0 & 0 & \beta_e(\omega) \end{bmatrix}, \tag{2.18}$$

where $\gamma_e(\omega)$ and $\beta_e(\omega)$ are the first order *surface susceptibilities*. Physically, these surface susceptibilities describe the ability of the surface to be polarized in directions parallel (γ) or perpendicular (β) to the surface. By substituting Eq. (2.18) into Eq. (2.16a), we now get the following relations for the surface polarization density

$$\mathbf{P}^s(\mathbf{r}_{\|}, \omega) = \gamma_e(\omega)\bar{\mathbf{E}}_{\|}(\mathbf{r}_{\|}, \omega) \tag{2.19a}$$

$$P_z^s(\mathbf{r}_{\|}, \omega) = \beta_e(\omega)\bar{D}_z(\mathbf{r}_{\|}, \omega). \tag{2.19b}$$

In the following, the discussion will be limited to non-magnetic materials, and $\mathbf{M}^{\mathrm{s}}$ will thus be equal to zero. It will therefore not be necessary to specify a constitutive tensor for the magnetization. In order to simplify notation, the subscript and explicit frequency dependence will from now on be dropped from the surface susceptibilities, so that $\gamma = \gamma_e(\omega)$ and $\beta = \beta_e(\omega)$.

Eqs. (2.16a) and (2.18) do not take into account the possible spatial dispersion at the interface. These effects can be described by introducing the second order surface susceptibilities δ and τ. These coefficients are smaller than the first order coefficients γ and β by a factor d/λ, where d is the thickness of the surface region and λ is the optical wavelength. They can therefore be neglected in the limit where the surface layer is thin compared to the wavelength of the light [7, 3].

In the derivation of the effective boundary conditions, the dividing surface between the two bulk media was chosen at some plane $z = 0$ in the boundary region. The exact position of the dividing surface is obviously just a mathematical convenience, and should not have any physical relevance. The measurable physical quantities of the surface can therefore not depend on this choice of dividing surface. It turns out that the surface susceptibilities depend on this choice, however, it is possible to construct so-called *invariants* or combinations of the surface susceptibilities that are independent of the dividing surface. All measurable quantities can then be given in terms of these combinations. An extensive discussion on such invariants can be found in [7].

2.2.3. Reflection and transmission coefficients

The Fresnel coefficients of the surface may now be calculated using the same procedure as the one outlined in section 2.1, but this time using the effective boundary conditions in Eq. (2.15) and the constitutive relation in

Eq. (2.19). From this derivation one finds that the laws of reflection and refraction, Eq. (2.4), remain unmodified. Assuming non-magnetic media ($\mathbf{M}^s = 0$) and no spatial dispersion ($\delta = 0,\ \tau = 0$), the following reflection and transmission coefficients can be found for s-polarized light [7, 3]

$$r_s(\omega) = \frac{n^- \cos\theta_i - n^+ \cos\theta_t + i(\omega/c)\gamma}{n^- \cos\theta_i + n^+ \cos\theta_t - i(\omega/c)\gamma}, \tag{2.20}$$

$$t_s(\omega) = \frac{2n^- \cos\theta_i}{n^- \cos\theta_i + n^+ \cos\theta_t - i(\omega/c)\gamma}. \tag{2.21}$$

For p-polarized light the coefficients take the form

$$r_p(\omega) = \frac{\kappa^-(\omega) - i(\omega/c)\gamma\cos\theta_i\cos\theta_t + i(\omega/c)n^-n^+\varepsilon^-\beta\sin^2\theta_i}{\kappa^+(\omega) - i(\omega/c)\gamma\cos\theta_i\cos\theta_t - i(\omega/c)n^-n^+\varepsilon^-\beta\sin^2\theta_i} \tag{2.22}$$

and

$$t_p(\omega) = \frac{\left[1 + (\omega/2c)^2\varepsilon^-\gamma\beta\sin^2\theta_i\right]}{\kappa^+(\omega) - i(\omega/c)\gamma\cos\theta_i\cos\theta_t - i(\omega/c)n^-n^+\varepsilon^-\beta\sin^2\theta_i}, \tag{2.23}$$

where

$$\kappa^\pm(\omega) = (n^+ \cos\theta_i \pm n^- \cos\theta_t)\Big(1 - \frac{\omega^2}{4c^2}\varepsilon^-\gamma\beta\sin^2\theta_i\Big). \tag{2.24}$$

Here $n^\pm$ is the refractive index for the bulk regions above (+) and below (−) the surface. For non-magnetic materials $n = \sqrt{\varepsilon}$, where ε is the relative permittivity of the medium. The angles of incidence and transmission are given by θ_i and θ_t, respectively. The constant $c = 1/\sqrt{\varepsilon_0\mu_0}$ is the speed of light in vacuum.

We notice from Eqs. (2.20) – (2.23) that the coefficients for the s-polarized wave only involves the surface susceptibility γ, while the coefficients for the p-polarized wave involve both γ and β (remember that γ corresponds to an excitation of a mode parallel to the surface, while β corresponds to an excitation of a mode normal to the surface). This makes sense, since the s-polarized light only has an **E**-component parallel to the surface, while the p-polarized light has **E**-components both parallel and perpendicular to the surface.

It is also worth noting that in the limit of a disappearing boundary region where $\gamma = \beta = 0$, *i.e.* a perfectly sharp interface, Eqs. (2.20) – (2.23) reduce to the ordinary Fresnel coefficients, Eq. (2.3), as expected.

2.3. Plasmonics

The interaction between light and a non-sharp interface consisting of metallic nanoparticles on a surface can also be described in terms of *plasmonics*. Plasmonics or *nanoplasmonics* is the study of the interaction between electromagnetic radiation and metallic nanostructures of sizes much smaller than the wavelength [11]. The name is derived from *plasmon* which is the quasiparticle resulting from the quantization of oscillations in a plasma. An example of such plasma oscillations is the collective oscillations of the charge density in a metal.

This section is not meant to be a comprehensive review of the field of plasmonics, but rather an introduction to some of the terms used in later chapters. A thorough treatment of this subject can be found in several textbooks, such as [11].

The combination of visible light and metallic particles of nanometer-size leads to characteristic behaviours which cannot be reproduced at other scales and spectral ranges. Nanoplasmonics can therefore be said to unfold on a characteristic length scale between 2 and 20 nm [5]. This is due to the strong frequency dependence in the properties of the materials, and most of the physics in the interaction between the light and the metallic islands is therefore contained in the complex dielectric functions of the materials [12].

In later chapters, metallic island particles of different shapes and sizes on a substrate will be studied. The plasmons excited in such nanoparticles are so-called *localized* surface plasmons, since they do not propagate[1]. These plasmons are quanta of the excitations of the conduction electrons in the metallic island, due to the coupling with the electromagnetic field [11]. The free electrons are periodically displaced from the ion lattice, driven by the incident light. The displacement results in a build-up of opposite charges on opposite sides of the particle, which leads to a restoring force on the electrons. The result is a damped electron oscillator.

The frequency of the surface plasmon depends not only on the properties of the island material, but also on its size and shape and the properties of the surrounding material(s). An important property of the surface plasmon is the so-called *quality factor* Q, which is a measure of how many oscillations the surface plasmon undergoes before it decays, and therefore is related to the lifetime of the plasmon. The quality factor Q can be expressed through the real and imaginary parts of the complex dielectric

---

[1] Unlike the *surface plasmon polaritons* (SPP's), which *do* propagate.

function of the metal in the following way [5]

$$Q = -\frac{\mathrm{Re}[\varepsilon_m]}{\mathrm{Im}[\varepsilon_m]}. \tag{2.25}$$

2.3.1. Plasmonic hybridization

When combining simple plasmonic systems into more complex ones, the plasmon resonances of the new structure can be found by combining the fundamental resonances of the individual parts, as demonstrated by [9].

The simplest example of this is the combination of a metallic sphere and a spherical cavity in a metal into a spherical shell. Such a cavity or *void* can also support a plasmon mode, very similar to that of a solid spherical particle. It turns out that the plasmon modes of the combined system can be found from a *hybridization* of the dipolar modes of the two simpler systems. It can be shown [11] that the dipolar plasmon in the metallic sphere will have a resonance frequency of

$$\omega_{sp} = \frac{\omega_B}{\sqrt{3}}, \tag{2.26}$$

while the spherical cavity plasmon has a resonance frequency of

$$\omega_c = \sqrt{\frac{2}{3}}\omega_B, \tag{2.27}$$

where ω_B is the bulk plasma frequency of the metal. When combining the two geometries, these two fundamental resonances will interact with each other and split into two new plasmons, a low energy symmetric one ($-$) and a high energy antisymmetric one ($+$), such that

$$E_- < E_{sphere} < E_{cavity} < E_+, \tag{2.28}$$

where E_{sphere} and E_{cavity} are the energies of the plasmon in the original metallic sphere system and spherical cavity system, respectively. This is illustrated in Figure 2.2.

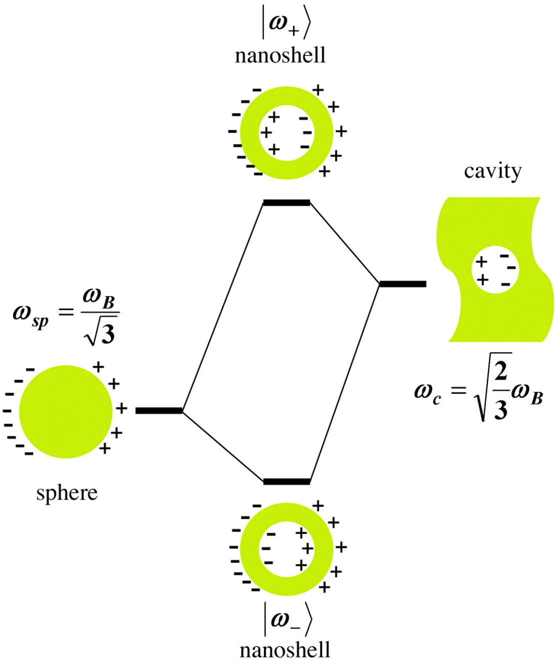

Figure 2.2: Schematic of the energy levels showing the hybridization of the dipolar plasmons in the metallic shell system resulting from the interaction between the sphere and cavity plasmons. The two shell plasmons are split into a high energy antisymmetric mode and a low energy symmetric mode. Figure from [9].

3. Island geometry

In the previous chapter it was outlined how one can calculate the macroscopic optical properties of a general boundary layer between two bulk media, once the *surface susceptibilities* of that boundary are known. These coefficients in general depend on the properties of the specific boundary, and must be calculated for each individual case. In this and the following chapter, a boundary consisting of a thin film of truncated and coated prolate spheroidal particles is treated, and the surface susceptibilities for this system are calculated from the particle polarizabilities using a quasi-static approximation.

The system considered in the following is depicted in Figure 3.1. It consists of a film of identical prolate spheroidal particles on a substrate, with the symmetry axis of the particles perpendicular to the substrate. The particles may have a number of concentric *coating layers*, and may also be *truncated* by the substrate.

When calculating the surface susceptibilities of this boundary layer, the assumption is made that the film of particles (or *islands*) is of low coverage. This simplifies the problem considerably, since it means that the polarizability of a single island can be calculated first, and then later corrected for interactions with neighboring islands. The calculation of the single island polarizability is performed in chapter 4.

In this chapter the geometry of this single island system is studied in detail, and concepts are introduced which will be needed when performing the calculations in the next chapter. In sections 3.1 and 3.2 prolate spheroids in general and the prolate spheroidal coordinate system are discussed. In sections 3.3 – 3.5 some definitions and relations to be used in later chapters are defined.

3.1. Spheroids

A spheroid is generated by rotating an ellipse around one of its axes. Rotation around the minor axis yields an *oblate* spheroid, while rotation

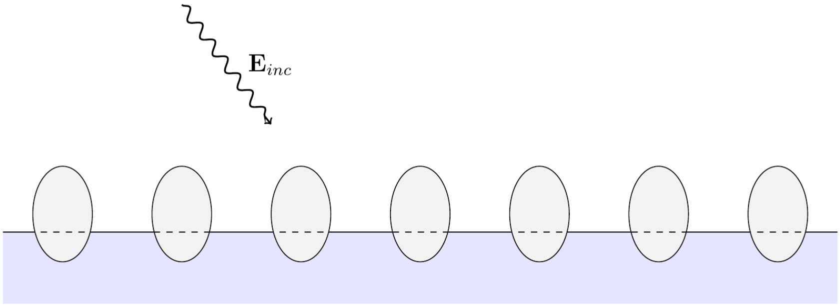

Figure 3.1: Cross-section of the surface system. A flat substrate is covered by prolate spheroidal islands with their axis of symmetry orthogonal to the substrate. The density of islands is assumed to be low. The island size is small compared to the wavelength of the incident light.

around the major axis yields a *prolate* spheroid. The equation describing a prolate spheroid is

$$\frac{x^2 + y^2}{R_{\|}} + \frac{z^2}{R_{\perp}} = 1 \tag{3.1}$$

where $R_{\|}$ is the semiminor and $R_{\perp}$ is the semimajor axis of the ellipse (cf. Fig. 3.2). The subscripts of these radii denote the fact that the prolate spheroid in our system will have its symmetry axis (*i.e.* the major axis) orthogonal to the substrate.

In order to define a spheroid, one needs two parameters. These can be the two radii $R_{\|}$ and $R_{\perp}$, but in many cases it can be advantageous to use another pair of parameters. An important property of a spheroid is the distance from the center to the two focal points, which lie on the major axis of the rotated ellipse, *i.e.* on the axis of revolution of the prolate spheroid. This distance, called the *focal radius*, is denoted by a in the following, and is given by the two radii [13]

$$a = \sqrt{R_{\perp}^2 - R_{\|}^2}. \tag{3.2}$$

Another important property of the prolate spheroid is the so-called *elongation parameter* ξ_0, defined as

$$\xi_0 = \frac{R_{\perp}}{a} = \frac{R_{\perp}}{\sqrt{R_{\perp}^2 - R_{\|}^2}}, \tag{3.3}$$

with $1 \leq \xi_0 < \infty$. A spheroid can now be defined by the two numbers

a, ξ_0, which leads to the radii

$$\begin{aligned} R_\perp &= a\xi_0 \\ R_\parallel &= a\sqrt{\xi_0^2 - 1}. \end{aligned} \tag{3.4}$$

At the limits of the two parameters a, ξ_0, the spheroid takes the form

$$\begin{aligned} \xi_0 \to \infty, a \to 0, a\xi_0 = R &: \text{ Sphere with radius } R \\ \xi_0 \to 1 &: \text{ Needle with length } 2a. \end{aligned} \tag{3.5}$$

The parameters a, ξ_0 are important when defining the prolate spheroidal coordinate system (ξ, η, ϕ), which is used later. In these coordinates, ξ is the 'radial' component, and a surface of constant $\xi = \xi_0$ is a prolate spheroid with a ξ_0 of this value.

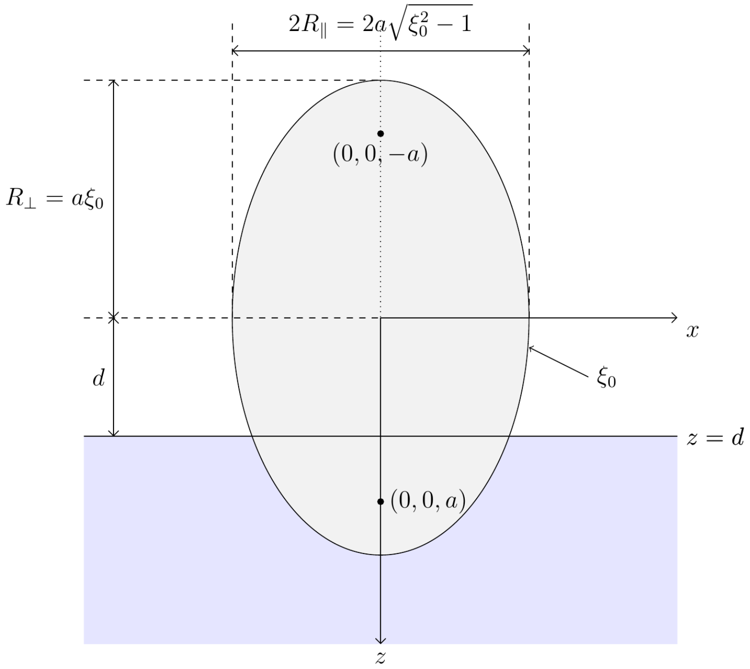

Figure 3.2: Cross-section of a single prolate spheroidal island, truncated by the substrate, including all important spheroid parameters. Here the Cartesian coordinate system with origin in the spheroid center is also specified.

3.2. Prolate spheroidal coordinates

A coordinate system fit for the spheroidal symmetry of our system is the prolate spheroidal coordinate system (ξ, η, ϕ). This is an orthogonal coordinate system, similar in many ways to the spherical coordinates (r, θ, ϕ). The mapping from Cartesian coordinates to prolate spheroidal ones is defined as follows

$$\begin{aligned}\xi &\equiv \frac{\rho_1 + \rho_2}{2a}, \\ \eta &\equiv \frac{\rho_1 - \rho_2}{2a}, \\ \phi &\equiv \arctan\left(\frac{y}{x}\right),\end{aligned} \tag{3.6}$$

where

$$\begin{aligned}\rho_1 &\equiv \sqrt{(z+a)^2 + x^2 + y^2}, \\ \rho_2 &\equiv \sqrt{(z-a)^2 + x^2 + y^2}.\end{aligned} \tag{3.7}$$

Here ρ_1 and ρ_2 are the distances from a point (x, y, z) to the two foci lying on the z-axis and ϕ is the angle between the x-axis and the projection of the vector from the origin to the point (x, y, z) on the (x, y)-plane.

The values of ξ, η, ϕ have the following ranges

$$\begin{aligned}1 \leq \xi &< \infty, \\ -1 \leq \eta &\leq 1, \\ 0 \leq \phi &< 2\pi.\end{aligned} \tag{3.8}$$

The prolate spheroidal coordinates can be seen as a generalization of the spherical coordinates (r, θ, ϕ). Whereas in spherical coordinates surfaces of constant r are concentric spheres, in prolate spheroidal coordinates the surfaces of constant ξ are concentric prolate spheroids.

The transformation back to Cartesian coordinates can be performed as follows

$$\begin{aligned}x &= a\sqrt{(\xi^2 - 1)(1 - \eta^2)}\cos\phi, \\ y &= a\sqrt{(\xi^2 - 1)(1 - \eta^2)}\sin\phi, \\ z &= a\xi\eta.\end{aligned} \tag{3.9}$$

It will in later sections be necessary to express the normal derivative at the substrate surface in terms of prolate spheroidal coordinates. Since the substrate is lying in the xy-plane, this corresponds to finding the derivative with respect to z. This can be written in prolate spheroidal coordinates

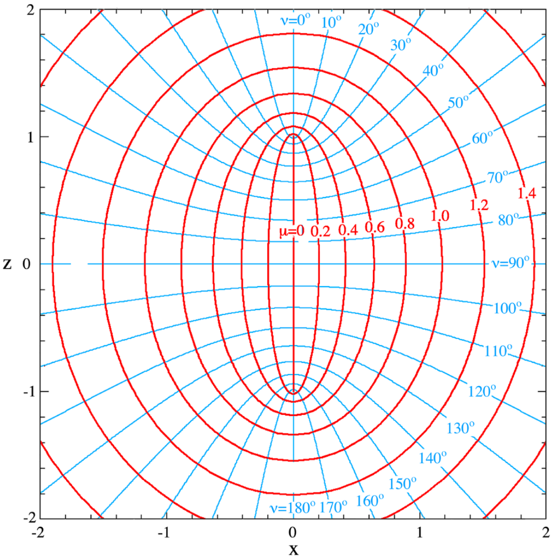

Figure 3.3: Illustration of the prolate spheroidal coordinate system in the xz-plane, *i.e.* for $\phi = 0$. Here the angle ϕ corresponds to a rotation around $z = 0$. The red lines are surfaces of constant ξ (denoted by μ in this figure), while the blue lines are surfaces of constant $\nu = \arccos \eta$. Note that the red and blue lines are always orthogonal, making the prolate spheroidal coordinates an orthogonal coordinate system. Picture taken from [14].

as

$$\begin{aligned}\frac{\partial}{\partial z} &= \frac{\partial \xi}{\partial z}\frac{\partial}{\partial \xi} + \frac{\partial \eta}{\partial z}\frac{\partial}{\partial \eta} + \frac{\partial \phi}{\partial z}\frac{\partial}{\partial \phi} \\ &= \frac{\partial}{\partial z}\left(\frac{\rho_1+\rho_2}{2a}\right)\frac{\partial}{\partial \xi} + \frac{\partial}{\partial z}\left(\frac{\rho_1-\rho_2}{2a}\right)\frac{\partial}{\partial \eta} \\ &= \frac{\eta}{a}\frac{(\xi^2-1)}{(\xi^2-\eta^2)}\frac{\partial}{\partial \xi} + \frac{\xi}{a}\frac{(1-\eta^2)}{(\xi^2-\eta^2)}\frac{\partial}{\partial \eta}.\end{aligned} \tag{3.10}$$

In any coordinate systems it is useful to know how an infinitesimal step ds in an arbitrary direction depends on the coordinates. This is described by the *metric tensor*, which in prolate spheroidal coordinates takes the form

$$\mathrm{d}s^2 = g_{\xi\xi}\mathrm{d}\xi^2 + g_{\eta\eta}\mathrm{d}\eta^2 + g_{\phi\phi}\mathrm{d}\phi^2 \tag{3.11}$$

where ds is a curve element and $g_{\xi\xi}, g_{\eta\eta}, g_{\phi\phi}$ are the diagonal elements of the metric tensor. All off-diagonal elements of the tensor are zero because the prolate spheroidal coordinate system is an orthogonal system. These elements are given by [13]

$$\begin{aligned}
g_{\xi\xi} &= \left(\frac{\partial x}{\partial \xi}\right)^2 + \left(\frac{\partial y}{\partial \xi}\right)^2 + \left(\frac{\partial z}{\partial \xi}\right)^2 = a^2\frac{\xi^2-\eta^2}{\xi^2-1} \\
g_{\eta\eta} &= \left(\frac{\partial x}{\partial \eta}\right)^2 + \left(\frac{\partial y}{\partial \eta}\right)^2 + \left(\frac{\partial z}{\partial \eta}\right)^2 = a^2\frac{\xi^2-\eta^2}{1-\eta^2} \\
g_{\phi\phi} &= \left(\frac{\partial x}{\partial \phi}\right)^2 + \left(\frac{\partial y}{\partial \phi}\right)^2 + \left(\frac{\partial z}{\partial \phi}\right)^2 = a^2(\xi^2-1)(1-\eta^2).
\end{aligned} \tag{3.12}$$

3.3. Truncation

In order to completely specify the island in our system, we must also introduce a third parameter. This is the so-called *truncation ratio* t_r, which determines where on the major axis the spheroid is truncated by the substrate placed at $z = d$. The truncation ratio is defined as

$$t_r = \frac{d}{R_\perp} = \frac{d}{a\xi_0} \tag{3.13}$$

and is defined in the range $(-1 < t_r < 1)$. When $(0 < t_r < 1)$, the center of the spheroid lies above the substrate, while a spheroid with its center below the substrate (sometimes called a *spheroidal cap*), has $(-1 < t_r < 0)$. A *hemispheroid* has a truncation ratio of 0.

3.4. Concentric prolate spheroids

The spheroidal nanoparticles of our system may have an arbitrary number of coating layers with different properties. In order to simplify calculations of the boundary conditions, these layers of coating will be treated as *concentric spheroids*. Concentric spheroids differs from concentric spheres by the fact that it is not sufficient for the spheroids to have the same center for them to be concentric. As is seen from Eq. (3.6), the parameter a is a constant in the prolate spheroidal coordinate system. This means that in order for us to treat boundaries between different coating layers as spheroidal surfaces of constant ξ in the same system of coordinates, we must ensure that all these spheroids have the same focal distance a. An example of concentric spheroids can be seen in Fig. 3.4.

3.4.1. Numbering convention

In the next sections, the medium above the substrate (the *ambient*) will be denoted medium 1 and the substrate medium 2. The numbering of

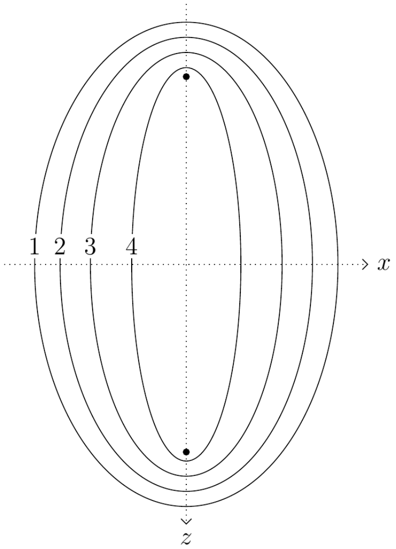

Figure 3.4: Cross-section of $S = 4$ concentric spheroids, *i.e.* spheroids with a common center and parameter a. The black dots indicate the position of the focus points, which are common for all the spheroids 1–4.

other media will be based on the number of layers in the island. The spheroidal interfaces between layers of the island will be assigned a number $s = 1, 2, 3, ..., S$, where S is the total number of spheroidal interfaces. Now $s = 1$ corresponds to the outer surface of the particle, while $s = S$ corresponds to the innermost interface. If $S = 1$, we have an uncoated particle. The different media adjacent to s are now named according to Fig. 3.5, so that all odd-numbered media lie above the substrate, while all even-numbered media lie below.

Each spheroidal interface s now has its own set of parameters $R_{\perp,s}$, $R_{\|,s}$, $\xi_{0,s}$ and $t_r^{(s)}$. The focus distance a is the same for all the concentric spheroids, as mentioned above. By introducing a radius ratio

$$\chi_s = \frac{R_{\perp,s}}{R_{\perp,1}} \leq 1, \tag{3.14}$$

where $R_{\perp,1}$ is the semimajor axis of the outermost spheroid, one can express all these parameters in terms of this ratio and the parameters of the

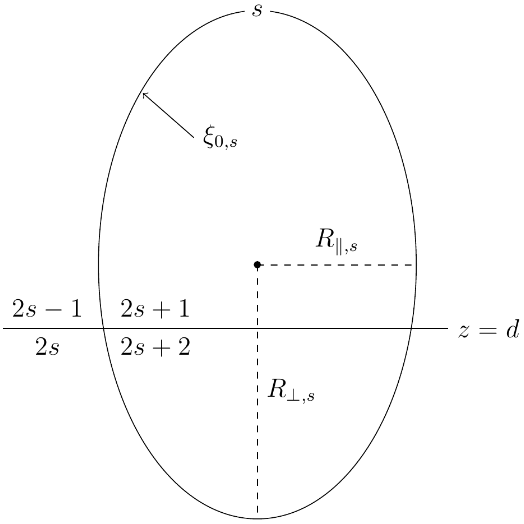

Figure 3.5: Illustration of the numbering convention used in this text for different media adjacent to the spheroidal interface s.

outermost layer. One then gets the following relations

$$\begin{aligned}
R_{\perp,s} &= \chi_s R_{\perp,1} \\
R_{\parallel,s} &= \sqrt{R_{\perp,s}^2 - a^2} = \sqrt{(\chi_s R_{\perp,1})^2 - a^2} \\
\xi_{0,s} &= \frac{R_{\perp,s}}{a} = \frac{\chi_s R_{\perp,1}}{a} \\
t_r^{(s)} &= \frac{t_r^{(1)}}{\chi_s}
\end{aligned} \tag{3.15}$$

The geometry of our system can now be completely specified by the parameters a, $\xi_{0,1}$, $t_r^{(1)}$ and χ_s.

The number of different regions N of our system depends on the truncation ratio, since the substrate may or may not divide the spheroidal interface s into two regions. From Eqs. (3.15) and (3.13), we see that if $t_r^{(s)} \geq 1$, or equivalently $\chi_s \leq t_r^{(1)}$, the spheroid s is not truncated by the substrate. If none of the spheroidal layers are truncated, we have $S+2$ media: One for each layer, in addition to the ambient and the substrate. If all spheroids are truncated we get two different media for each layer, *i.e.* $2S+2$ media in total. Hence, the total number of regions N lies somewhere in the range $S+2 \leq N \leq 2S+2$.

3.5. Transformations between z-shifted coordinates

In the calculations of the potential in the different regions, a few different coordinate systems will be used to account for multipoles in different positions. All coordinate systems, however, will be prolate spheroidal coordinates with the same parameter a. The only difference is the position of the origin, which for all coordinate systems will lie on the z-axis.

In order to be able to express the solutions in terms of one set of coordinates, we therefore need a mapping between two prolate spheroidal coordinate systems (ξ, η, ϕ) and (ξ', η', ϕ') where the latter has been shifted a distance Δz along the z-axis. The two first coordinate transformations can be written as the functionals $\xi'[\Delta z, a](\xi, \eta)$ and $\eta'[\Delta z, a](\xi, \eta)$, while for the last coordinate we have $\phi = \phi'$. From [7] we have

$$\begin{aligned}\xi'[\Delta z, a](\xi, \eta) = \frac{1}{2}\sqrt{2}\xi \Bigg\{ & 1 + \frac{(\Delta z)^2}{a^2\xi^2} - \frac{2\Delta z}{a\xi}\eta + \frac{\eta^2}{\xi^2} \\ & + \left[\left(1 + \frac{(\Delta z)^2}{a^2\xi^2} - \frac{2\Delta z}{a\xi}\eta + \frac{\eta^2}{\xi^2} \right)^2 \right. \\ & \left. - \frac{4}{\xi^2}\left(\frac{\Delta z}{a\xi} - \eta \right)^2 \right]^{\frac{1}{2}} \Bigg\}^{\frac{1}{2}}\end{aligned} \tag{3.16}$$

$$\begin{aligned}\eta'[\Delta z, a](\xi, \eta) = \sqrt{2}\left(\eta - \frac{\Delta z}{a\xi} \right) \Bigg\{ & 1 + \frac{(\Delta z)^2}{a^2\xi^2} - \frac{2\Delta z}{a\xi}\eta + \frac{\eta^2}{\xi^2} \\ & + \left[\left(1 + \frac{(\Delta z)^2}{a^2\xi^2} - \frac{2\Delta z}{a\xi}\eta + \frac{\eta^2}{\xi^2} \right)^2 \right. \\ & \left. - \frac{4}{\xi^2}\left(\frac{\Delta z}{a\xi} - \eta \right)^2 \right]^{\frac{1}{2}} \Bigg\}^{-\frac{1}{2}}\end{aligned} \tag{3.17}$$

4. Polarizability calculations

In order to find the surface susceptibilities of the film of prolate spheroidal islands, we first need to find the *polarizability* of a single island. It turns out that in the limit of small islands, compared to the wavelength of the incident radiation, this is equivalent to finding the electrostatic potential in all regions inside and around the island.

The system treated in this chapter is depicted in Fig. 4.1. Note that the parts of the spheroid below the substrate are treated as separate regions with individual dielectric functions $\varepsilon(\omega)$. In many real systems these regions are either part of the substrate or the island, but as will be clear in later sections, it is convenient mathematically to treat them as separate regions. In an actual system, they can later be made a part of *e.g.* the substrate simply by setting $\varepsilon(\omega)$ in all regions below the substrate boundary equal.

In sections 4.1 – 4.9 the potential problem is solved using a multipole expansion in the quasi-static limit. The multipole expansion coefficients are then used for finding the island polarizability and subsequently the surface susceptibilities in sections 4.10 and 4.11.

4.1. Laplace's equation and boundary conditions

Since the size of the islands is assumed small compared to the wavelength of the incoming light, one can treat the incoming radiation as a homogeneous field and neglect retardation effects, *i.e.* consider the propagation of the field to be instantaneous over the region in question. This is called the quasi-static limit, and lets one describe the system using electrostatics. By removing all time derivatives, and also assuming no free charge or current present, the two first Maxwell equations (2.1) can be written

$$\boldsymbol{\nabla}\cdot\mathbf{D}=0,\qquad \boldsymbol{\nabla}\times\mathbf{E}=0. \tag{4.1}$$

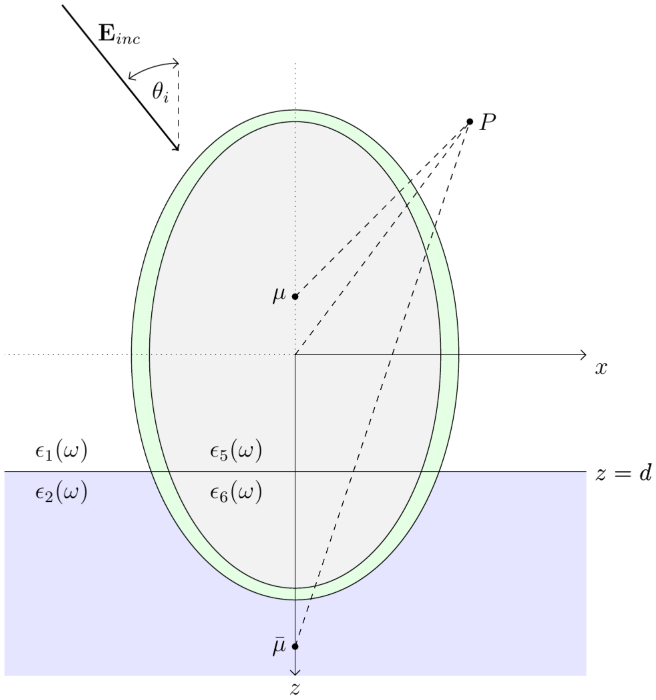

Figure 4.1: Cross-section of a single island with one coating layer, *i.e.* $S = 2$. All regions are assumed to have their own dielectric function $\varepsilon(\omega)$. The multipole expansion points μ and $\bar{\mu}$ are placed on the z-axis, equidistant from the substrate at $z = d$.

The electric field $\mathbf{E}$ can in electrostatics be expressed from the gradient of a scalar potential ψ

$$\mathbf{E}(\mathbf{r}) = -\boldsymbol{\nabla}\psi(\mathbf{r}). \tag{4.2}$$

By noting that $\mathbf{E} = \mathbf{D}/\varepsilon$ and inserting Eq. (4.2) into Eq. (4.1), we get the Laplace equation for the electric potential

$$\nabla^2\psi(\mathbf{r}) = 0. \tag{4.3}$$

Eq. (4.3) has infinitely many solutions, but combined with a set of boundary conditions, there is one unique solution for our system, as dictated by the *uniqueness theorem* [10].

The boundary conditions for the potential $\psi(\mathbf{r})$ on the interface between two media (denoted by $+$ and $-$), which follow from Eqs. (4.2) and (2.2), can be expressed like this

$$\psi_+(\mathbf{r}^+) = \psi_-(\mathbf{r}^-), \tag{4.4a}$$

$$\varepsilon_+(\omega)\frac{\partial}{\partial n}\psi_+(\mathbf{r}^+) = \varepsilon_-(\omega)\frac{\partial}{\partial n}\psi_-(\mathbf{r}^-), \qquad \forall\, \mathbf{r} \in \partial\Omega_{+-}. \tag{4.4b}$$

Here $\varepsilon_\pm(\omega)$ are the dielectric functions for medium + and −, $\partial\Omega_{+-}$ is the interface between medium + and medium −, $\mathbf{r}^\pm$ is a point on the interface just inside medium + or − and $\frac{\partial}{\partial n} = \hat{\mathbf{n}}\cdot\boldsymbol{\nabla}$ is the normal derivative at the interface.

Another condition is the requirement of a finite-valued potential $\psi(\mathbf{r})$ everywhere, *i.e.* that

$$|\psi(\mathbf{r})| < \infty, \quad \forall\, \mathbf{r}. \tag{4.5}$$

This means that we in particular must ensure that the potential is finite when $\mathbf{r} = 0$ and as $\mathbf{r} \to \infty$.

4.2. General solution of Laplace's equation

It turns out that Laplace's equation is separable in prolate spheroidal coordinates (defined in section 3.2), with the following complete set of functions as solutions [7]

$$\psi^{(1)}_{\ell m}(\mathbf{r}) = P^m_\ell(\xi) Y^m_\ell(\arccos\eta, \phi) \tag{4.6a}$$

$$\psi^{(2)}_{\ell m}(\mathbf{r}) = Q^m_\ell(\xi) Y^m_\ell(\arccos\eta, \phi) \tag{4.6b}$$

$$\ell = 0{,}1, 2, ...;\ m = 0, \pm1, \pm2, ... \pm \ell.$$

Here $P^m_\ell(\xi)$ and $Q^m_\ell(\xi)$ are the associated Legendre functions of first and second order, respectively. The first order functions $P^m_\ell(\xi)$ are given by

$$P^m_\ell(\xi) \equiv (-i)^m \frac{(\xi^2-1)^{m/2}}{2^\ell \ell!} \left(\frac{\mathrm{d}}{\mathrm{d}\xi}\right)^{\ell+m} (\xi^2-1)^\ell, \tag{4.7}$$

and has the symmetry property

$$P^m_\ell(-\xi) = (-1)^{\ell+m} P^m_\ell(\xi). \tag{4.8}$$

The second order functions $Q^m_\ell(\xi)$ are given by

$$\begin{aligned} Q^m_\ell(\xi) \equiv &(-1)^m \frac{(\xi^2-1)^{m/2}}{2^\ell \ell!} \left(\frac{\mathrm{d}}{\mathrm{d}\xi}\right)^{m} \left\{ \left(\frac{\mathrm{d}}{\mathrm{d}\xi}\right)^{\ell} \left[\ln\left(\frac{\xi+1}{\xi-1}\right)(\xi^2-1)^\ell\right] \right. \\ &\left. - \frac{1}{2}\ln\left(\frac{\xi+1}{\xi-1}\right)\left(\frac{\mathrm{d}}{\mathrm{d}\xi}\right)^{\ell}(\xi^2-1)^\ell \right\}, \end{aligned} \tag{4.9}$$

for $1 \leq \xi < \infty$ and $m \geq 0$. For $m < 0$, one has the relations

$$\begin{aligned} P_\ell^m(\xi) \equiv& (-1)^m \frac{(\ell+m)!}{(\ell-m)!} P_\ell^{-m}(\xi), \\ Q_\ell^m(\xi) \equiv& \frac{(\ell+m)!}{(\ell-m)!} Q_\ell^{-m}(\xi). \end{aligned} \tag{4.10}$$

The spherical harmonics, $Y_\ell^m(\arccos\eta, \phi)$, are defined as

$$Y_\ell^m(\arccos\eta, \phi) \equiv \sqrt{\frac{(2\ell+1)(\ell-m)!}{4\pi(\ell+m)!}} (-1)^m P_\ell^m(\eta) e^{im\phi}, \tag{4.11}$$

where, again, $P_\ell^m(\eta)$ are the associated Legendre functions of first order, as defined by Eq. (4.7). For the spherical harmonics we have the orthonormality relation

$$\int_0^{2\pi} \mathrm{d}\phi \int_{-1}^{1} d\xi \, [Y_\ell^m(\arccos\eta, \phi)]^* \, Y_{\ell'}^{m'}(\arccos\eta, \phi) = \delta_{\ell\ell'}\delta_{mm'}, \tag{4.12}$$

where the asterisk denotes a complex conjugation and δ is the Kronecker delta. Another useful relation involving spherical harmonics is the following:

$$\int_0^{2\pi} \mathrm{d}\phi \, [Y_\ell^m(\arccos\eta, \phi)]^* \, Y_{\ell'}^{m'}(\arccos\eta', \phi) = \delta_{mm'} \zeta_{\ell\ell'}^m P_\ell^m(\eta) P_{\ell'}^{m'}(\eta'). \tag{4.13}$$

This follows from the orthogonality relation

$$\int_0^{2\pi} \mathrm{d}\phi \; e^{i(m-m')\phi} = 2\pi\delta_{mm'}. \tag{4.14}$$

Here the quantity $\zeta_{\ell\ell'}^m$ is introduced, which is defined as

$$\zeta_{\ell\ell'}^m \equiv \frac{1}{2} \sqrt{\frac{(2\ell+1)(2\ell'+1)(\ell-m)!(\ell'-m)!}{(\ell+m)!(\ell'+m)!}}. \tag{4.15}$$

From Eq. (4.8) we see that the spherical harmonics Y_ℓ^m have the following symmetry in the coordinate η

$$Y_\ell^m(\arccos(-\eta), \phi) = (-1)^{\ell+m} Y_\ell^m(\arccos\eta, \phi). \tag{4.16}$$

4.3. Multipole expansion of the potential

Since we are interested in the potentials far from the substrate relative to the size of the islands, it is convenient to express the potential as a *multipole expansion* [10] in terms of the complete set of solutions in Eq. (4.6). In a region $\xi_1 \leq \xi \leq \xi_2$ without any sources, the general solution of Laplace's equation in prolate spheroidal coordinates can now be written

$$\begin{aligned}\psi(\mathbf{r}) = &\sum_{\ell m} A_{\ell m} \widetilde{Z}_\ell^m(\xi, a) Y_\ell^m(\arccos\eta, \phi) \\ &+ \sum_{\ell m} B_{\ell m} \widetilde{X}_\ell^m(\xi, a) Y_\ell^m(\arccos\eta, \phi),\end{aligned} \tag{4.17}$$

where $A_{\ell m}$ and $B_{\ell m}$ are the so-called *expansion coefficients* and $0 \leq \ell < \infty$, $-\ell \leq m \leq \ell$. For convenience the following functions have been introduced here

$$\widetilde{X}_\ell^m(\xi, a) \equiv i^m \frac{(\ell - m)!}{(2\ell - 1)!!} a^\ell P_\ell^m(\xi), \tag{4.18a}$$

$$\widetilde{Z}_\ell^m(\xi, a) \equiv \frac{(2\ell + 1)!!}{(\ell + m)!} a^{-\ell-1} Q_\ell^m(\xi), \tag{4.18b}$$

where the double factorial is defined as follows

$$n!! \equiv \begin{cases} 1 \cdot 3 \cdot 5 \cdot \ldots \cdot (n-2) \cdot n & \text{for } n \text{ odd} \\ 2 \cdot 4 \cdot 6 \cdot \ldots \cdot (n-2) \cdot n & \text{for } n \text{ even} \\ 1 & \text{for } n = 0, -1. \end{cases} \tag{4.19}$$

It can be shown [7] that in the long distance (and spherical) limit ($\xi \to \infty$), the functions $\widetilde{X}_\ell^m(\xi, a)$ and $\widetilde{Z}_\ell^m(\xi, a)$ become

$$\begin{aligned}&\widetilde{X}_\ell^m(\xi, a) \simeq (\xi a)^\ell \simeq r^\ell \quad \text{for } \xi \to \infty \\ &\widetilde{Z}_\ell^m(\xi, a) \simeq (\xi a)^{-\ell-1} \simeq r^{-\ell-1} \quad \text{for } \xi \to \infty.\end{aligned} \tag{4.20}$$

These functions thus describe the 'radial' part of the solution, in analogy to the radial part of the general solution in spherical coordinates. The response of the island can now be described by a multipole placed on the z-axis somewhere inside the island. This multipole is denoted by μ in the following, and its position in the main coordinate system with origin at the center of the island by $\mathbf{P}_\mu = (0, 0, \mu_z)$, where μ_z can be both positive and negative.

In order to model the interaction between the islands and the substrate, the *method of images* [10] is used. The potential due to the induced charge distribution in the substrate is then described by placing a second *image multipole* below the substrate, at the position of the first expansion point, mirrored over the substrate. This multipole is denoted by $\bar{\mu}$, and is positioned at $\mathbf{P}_{\bar{\mu}} = (0, 0, \bar{\mu}_z) = (0, 0, 2d - \mu_z)$ in the main coordinate system, where the substrate is placed at $z = d$.

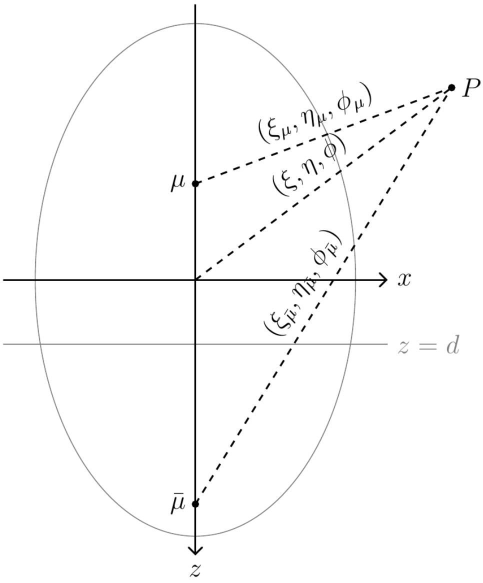

Figure 4.2: The four different coordinate systems used in the calculations. The main prolate spheroidal (ξ, η, ϕ) and cartesian (x, y, z) coordinate systems have their origin in the center of the island. The two other spheroidal systems $(\xi_\mu, \eta_\mu, \phi_\mu)$ and $(\xi_{\bar{\mu}}, \eta_{\bar{\mu}}, \phi_{\bar{\mu}})$ have their origin at the positions of the island (μ) and image ($\bar{\mu}$) multipoles, respectively. Note that since all three spheroidal coordinate systems share the same z-axis, $\phi = \phi_\mu = \phi_{\bar{\mu}}$.

In addition to the main coordinate system (ξ, η, ϕ), we now have two additional prolate spheroidal coordinate systems $(\xi_\mu, \eta_\mu, \phi_\mu)$ and $(\xi_{\bar{\mu}}, \eta_{\bar{\mu}}, \phi_{\bar{\mu}})$ centered at the expansion points $\mathbf{P}_\mu$ and $\mathbf{P}_{\bar{\mu}}$, respectively. These three coordinate systems, which all have the same parameter a, are shown in Figure 4.2. Using the functionals in Eq. (3.16) and Eq. (3.17) introduced in section 3.5, these coordinate systems can be related in the following way

$$\begin{aligned}
\xi_\mu &= \xi'[\Delta z = \mu_z, a](\xi,\eta) \\
\xi_{\bar{\mu}} &= \xi'[\Delta z = 2d - \mu_z, a](\xi,\eta) \\
\eta_\mu &= \eta'[\Delta z = \mu_z, a](\xi,\eta) \\
\eta_{\bar{\mu}} &= \eta'[\Delta z = 2d - \mu_z, a](\xi,\eta) \\
\phi_\mu &= \phi_{\bar{\mu}} = \phi
\end{aligned} \tag{4.21}$$

4.4. Potential in different regions

Since the Laplace equation (4.3) is homogeneous and linear, we can construct linear combinations of solutions that are also guaranteed to be solutions. In order to find the potentials in the different regions, we therefore need to sum up the contributions from the island multipoles, the image multipoles and the incoming radiation in each region. This will satisfy Laplace's equation, but in order to also satisfy the boundary conditions in Eq. (4.4), we need to determine the coefficients in front of the different contributions in all regions.

By noting that solutions on the form of Eq. (4.9) are singular in the origin (*i.e.* for $\xi = 1$), we can conclude that the potential in regions containing the origin cannot be represented by these solutions. Solutions on the form of Eq. (4.7) satisfy the Laplace equation in the origin and everywhere else, but do not approach a finite value as $\xi \to \infty$. These solutions can therefore not be used in regions where ξ is unlimited, that is, in the ambient (region 1) and the substrate (region 2).

For the regions below the substrate, there are no contributions from the image multipoles, as dictated by the principles of the method of images; Image charges do not contribute in the region where they are located [10].

We can now write up the expression for the potential in the ambient, by adding the contributions from the incoming field, the induced charge distribution in the island and the image multipoles in the substrate. In this region ξ is unlimited, so only solutions that approach zero as $\xi \to \infty$ are acceptable. We can therefore conclude that the second sum of Eq. (4.17) is zero, and the potential takes the form

$$\begin{aligned}
\psi_1(\mathbf{r}) = \psi_{\text{inc}}(\mathbf{r}) &+ {\sum_{\ell m}}' A^{(1)}_{\ell m} \widetilde{Z}^m_\ell(\xi_\mu, a) Y^m_\ell(\arccos \eta_\mu, \phi_\mu) \\
&+ {\sum_{\ell m}}' \bar{\mathcal{A}}^{(1)}_{\ell m} \widetilde{Z}^m_\ell(\xi_{\bar{\mu}}, a) Y^m_\ell(\arccos \eta_{\bar{\mu}}, \phi_{\bar{\mu}})
\end{aligned} \tag{4.22}$$

Here the term $\psi_{\rm inc}(\mathbf{r})$ denotes the potential corresponding to the incident radiation. $A^{(1)}_{\ell m}$ and $\bar{\mathcal{A}}^{(1)}_{\ell m}$ are the expansion coefficients corresponding to the island multipoles and image multipoles, respectively. The prime above the summation symbol indicates that the $\ell = 0$ term is excluded from the summation. This is due to the fact that there are no free charges in the system [7].

Similarly, in the substrate the potential can be written in the following way, with contributions from the island multipoles and the incoming radiation. In this region too, ξ is limitless, so only the first sum in Eq. (4.17) is a valid solution. Note that the image multipoles are not part of the solution here,

$$\psi_2(\mathbf{r}) = \psi_{\rm tr}(\mathbf{r}) + \sum_{\ell m}{}' A^{(2)}_{\ell m} \widetilde{Z}^m_\ell(\xi_\mu, a) Y^m_\ell(\arccos\eta_\mu, \phi_\mu). \tag{4.23}$$

Here the term $\psi_{\rm tr}(\mathbf{r})$ corresponds to the incident radiation, transmitted into the substrate.

The potential inside a coating layer above the substrate will have contributions from both the island multipoles and the image multipoles, and since $1 < \xi_1 \leq \xi \leq \xi_2 < \infty$, all the terms in (4.17) must be used for both multipoles,

$$\begin{aligned}\psi_3(\mathbf{r}) =& \psi^{(3)}_0 + \sum_{\ell m}{}' A^{(3)}_{\ell m} \widetilde{Z}^m_\ell(\xi_\mu, a) Y^m_\ell(\arccos\eta_\mu, \phi_\mu)\\ &+ \sum_{\ell m}{}' B^{(3)}_{\ell m} \widetilde{X}^m_\ell(\xi_\mu, a) Y^m_\ell(\arccos\eta_\mu, \phi_\mu)\\ &+ \sum_{\ell m}{}' \bar{\mathcal{A}}^{(3)}_{\ell m} \widetilde{Z}^m_\ell(\xi_{\bar{\mu}}, a) Y^m_\ell(\arccos\eta_{\bar{\mu}}, \phi_{\bar{\mu}})\\ &+ \sum_{\ell m}{}' \bar{\mathcal{B}}^{(3)}_{\ell m} \widetilde{X}^m_\ell(\xi_{\bar{\mu}}, a) Y^m_\ell(\arccos\eta_{\bar{\mu}}, \phi_{\bar{\mu}}).\end{aligned} \tag{4.24}$$

Here $\psi^{(3)}_0$ is a constant.

In the innermost region of the spheroidal island, above the substrate, only solutions on the form of the second sum of (4.17) can be used, since

$\widetilde{Z}_\ell^m(\xi, a)$ diverges in the origin,

$$\begin{aligned}\psi_5(\mathbf{r}) =&\psi_0^{(5)} + \sum_{\ell m}{}^{\prime} B_{\ell m}^{(5)} \widetilde{X}_\ell^m(\xi_\mu, a) Y_\ell^m(\arccos \eta_\mu, \phi_\mu) \\ &+ \sum_{\ell m}{}^{\prime} \bar{\mathcal{B}}_{\ell m}^{(5)} \widetilde{X}_\ell^m(\xi_{\bar{\mu}}, a) Y_\ell^m(\arccos \eta_{\bar{\mu}}, \phi_{\bar{\mu}}).\end{aligned} \tag{4.25}$$

Expressions for the potential in all other regions could also be written up, in the same was as is done for these four regions. It is, however, more convenient to use a general expression for the potential in any given region. This is found in the next section.

4.5. General expressions for the potential

Using the numbering convention introduced in section 3.4 (cf. Fig. 3.5), the potentials in the different regions can now be written in a more general form. Using this convention, all regions above the substrate are odd-numbered, while all regions below the substrate are even-numbered. We therefore get the following expression for the potential in region i above the substrate:

$$\begin{aligned}\psi_i(\mathbf{r}) =&\delta_{i,1}\psi_{\text{inc}}(\mathbf{r}) + \psi_0^{(i)} \\ &+ \sum_{\ell m}{}^{\prime} \left[A_{\ell m}^{(i)} \widetilde{Z}_\ell^m(\xi_\mu, a) + B_{\ell m}^{(i)} \widetilde{X}_\ell^m(\xi_\mu, a) \right] Y_\ell^m(\arccos \eta_\mu, \phi_\mu) \\ &+ \sum_{\ell m}{}^{\prime} \left[\bar{\mathcal{A}}_{\ell m}^{(i)} \widetilde{Z}_\ell^m(\xi_{\bar{\mu}}, a) + \bar{\mathcal{B}}_{\ell m}^{(i)} \widetilde{X}_\ell^m(\xi_{\bar{\mu}}, a) \right] Y_\ell^m(\arccos \eta_{\bar{\mu}}, \phi_{\bar{\mu}}).\end{aligned} \tag{4.26}$$

For a region below the substrate we get

$$\begin{aligned}\psi_{i+1}(\mathbf{r}) = \delta_{i,1}\psi_{\text{tr}}(\mathbf{r}) + \psi_0^{(i+1)} + \sum_{\ell m}{}^{\prime} \Big[& A_{\ell m}^{(i+1)} \widetilde{Z}_\ell^m(\xi_\mu, a) \\ &+ B_{\ell m}^{(i+1)} \widetilde{X}_\ell^m(\xi_\mu, a) \Big] Y_\ell^m(\arccos \eta_\mu, \phi_\mu),\end{aligned} \tag{4.27}$$

with i odd. Here the terms ψ_0 are constant terms, and the prime above the summation still indicates that the $\ell = 0$ terms are excluded.

In order to completely specify the system, we now need to determine all the unknowns in these two expressions, *i.e.* the incident and transmitted potentials $\psi_{\text{inc}}(\mathbf{r})$ and $\psi_{\text{tr}}(\mathbf{r})$, the multipole expansion coefficients $A_{\ell m}$, $B_{\ell m}$, $\bar{\mathcal{A}}_{\ell m}$ and $\bar{\mathcal{B}}_{\ell m}$ in all regions and the constant term ψ_0 in all regions. This will be done in the following sections, by enforcing the boundary conditions on our system.

4.6. Boundary conditions at the substrate surface

At the substrate surface, we have interfaces between all media i above the substrate and $i+1$ below the substrate (with i odd). Here the boundary conditions given by Eq. (4.4) must be fulfilled, *i.e.* the potential and its normal derivative times the permittivity must be continuous at the interface.

By inserting the potentials in Eqs. (4.26) and (4.27) into the first boundary condition, Eq. (4.4a), the following relations between the coefficients are found [1]

$$\begin{aligned}\psi_0^{(i+1)} &= \psi_0^{(i)} \\ A_{\ell m}^{(i+1)} &= A_{\ell m}^{(i)} + (-1)^{\ell+m}\bar{\mathcal{A}}_{\ell m}^{(i)} \\ B_{\ell m}^{(i+1)} &= B_{\ell m}^{(i)} + (-1)^{\ell+m}\bar{\mathcal{B}}_{\ell m}^{(i)}.\end{aligned} \tag{4.28}$$

By inserting the potentials in Eqs. (4.26) and (4.27) into the second boundary condition, Eq. (4.4b), while using Eqs. (3.10) and (4.16), it can be shown [1] that the following set of relations for the coefficients also holds

$$\begin{aligned}\varepsilon_i A_{\ell m}^{(i)} - \varepsilon_i(-1)^{\ell+m}\bar{\mathcal{A}}_{\ell m}^{(i)} &= \varepsilon_{i+1} A_{\ell m}^{(i+1)} \\ \varepsilon_i B_{\ell m}^{(i)} - \varepsilon_i(-1)^{\ell+m}\bar{\mathcal{B}}_{\ell m}^{(i)} &= \varepsilon_{i+1} B_{\ell m}^{(i+1)}.\end{aligned} \tag{4.29}$$

When combining the results in Eqs. (4.28) and (4.29), we can now express all the unknown multipole coefficients in our system in terms of $A_{\ell m}^{(i)}$ and $B_{\ell m}^{(i)}$ (with i odd):

$$\begin{aligned}A_{\ell m}^{(i+1)} &= \frac{2\varepsilon_i}{\varepsilon_i+\varepsilon_{i+1}} A_{\ell m}^{(i)} &&= \mathcal{T}_i A_{\ell m}^{(i)} \\ B_{\ell m}^{(i+1)} &= \frac{2\varepsilon_i}{\varepsilon_i+\varepsilon_{i+1}} B_{\ell m}^{(i)} &&= \mathcal{T}_i B_{\ell m}^{(i)} \\ \bar{\mathcal{A}}_{\ell m}^{(i)} &= (-1)^{\ell+m}\frac{\varepsilon_i-\varepsilon_{i+1}}{\varepsilon_i+\varepsilon_{i+1}} A_{\ell m}^{(i)} &&= (-1)^{\ell+m}\mathcal{R}_i A_{\ell m}^{(i)} \\ \bar{\mathcal{B}}_{\ell m}^{(i)} &= (-1)^{\ell+m}\frac{\varepsilon_i-\varepsilon_{i+1}}{\varepsilon_i+\varepsilon_{i+1}} B_{\ell m}^{(i)} &&= (-1)^{\ell+m}\mathcal{R}_i B_{\ell m}^{(i)}.\end{aligned} \tag{4.30}$$

Here the following coefficients have been introduced

$$\begin{aligned}\mathcal{R}_i &= \frac{\varepsilon_i - \varepsilon_{i+1}}{\varepsilon_i + \varepsilon_{i+1}}\\ \mathcal{T}_i &= \frac{2\varepsilon_i}{\varepsilon_i + \varepsilon_{i+1}},\end{aligned} \tag{4.31}$$

which are recognized as the usual Fresnel coefficients.

The expressions for the potentials above and below the substrate can now be rewritten in terms of the two remaining unknown coefficients $A^{(i)}_{\ell m}$ and $B^{(i)}_{\ell m}$ (with odd i). In region i above the substrate we now have

$$\begin{aligned}\psi_i(\mathbf{r}) = \delta_{i,1}\psi_{inc}(\mathbf{r}) + \psi_0^{(i)} + \sideset{}{'}\sum_{\ell m} A^{(i)}_{\ell m}\Big[&\widetilde{Z}_\ell^m(\xi_\mu, a)Y_\ell^m(\arccos\eta_\mu, \phi_\mu)\\ &+ (-1)^{\ell+m}\mathcal{R}_i\widetilde{Z}_\ell^m(\xi_{\bar{\mu}}, a)Y_\ell^m(\arccos\eta_{\bar{\mu}}, \phi_{\bar{\mu}})\Big]\\ + \sideset{}{'}\sum_{\ell m} B^{(i)}_{\ell m}\Big[&\widetilde{X}_\ell^m(\xi_\mu, a)Y_\ell^m(\arccos\eta_\mu, \phi_\mu)\\ &+ (-1)^{\ell+m}\mathcal{R}_i\widetilde{X}_\ell^m(\xi_{\bar{\mu}}, a)Y_\ell^m(\arccos\eta_{\bar{\mu}}, \phi_{\bar{\mu}})\Big].\end{aligned} \tag{4.32}$$

In region $i+1$ below the substrate we have

$$\begin{aligned}\psi_{i+1}(\mathbf{r}) = &\;\delta_{i,1}\psi_{tr}(\mathbf{r}) + \psi_0^{(i+1)}\\ &+ \mathcal{T}_i\sideset{}{'}\sum_{\ell m}\Big[A^{(i)}_{\ell m}\widetilde{Z}_\ell^m(\xi_\mu, a) + B^{(i)}_{\ell m}\widetilde{X}_\ell^m(\xi_\mu, a)\Big]\,Y_\ell^m(\arccos\eta_\mu, \phi_\mu).\end{aligned} \tag{4.33}$$

4.7. Boundary conditions at the spheroidal interfaces

As mentioned in section 3.2, in spheroidal coordinates, a interface between two spheroids is a surface of constant ξ. In our systems there are spheroidal interfaces between the ambient and the outermost layer of the island, between the substrate and the outermost layer of the part of the island buried the substrate, and between possible internal layers of the island.

We now denote the spheroidal interface s, *i.e.* the spheroid of constant $\xi_{0,s}$, by $\bigcirc_s$. If this spheroid is truncated by the substrate, it will have two parts, one above the substrate boundary and one below. These parts are denoted by $\cap_s$ and $\cup_s$, respectively. We can now write the angular integration over the surface in terms of the operators

$$\int_{\bigcirc_s} \mathrm{d}\Omega = \int_{\cap_s} \mathrm{d}\Omega + \int_{\cup_s} \mathrm{d}\Omega. \tag{4.34}$$

In prolate spheroidal coordinates, these terms can be written

$$\begin{aligned} \int_{\bigcirc_s} \mathrm{d}\Omega &= \int_{-1}^{1} \mathrm{d}\eta \int_0^{2\pi} \mathrm{d}\phi \\ \int_{\cap_s} \mathrm{d}\Omega &= \int_{-1}^{t_r^{(s)}} \mathrm{d}\eta \int_0^{2\pi} \mathrm{d}\phi \\ \int_{\cup_s} \mathrm{d}\Omega &= \int_{t_r^{(s)}}^{1} \mathrm{d}\eta \int_0^{2\pi} \mathrm{d}\phi \end{aligned} \tag{4.35}$$

4.7.1. Weak formulation of the boundary condition

The boundary conditions in Eq. (4.4) should in principle be satisfied at any interface between two media. For the spheroidal interfaces, however, it is more convenient to apply the so-called *weak formulation* of the boundary conditions [7]. These exploit the fact that at a spheroidal surface, the spheroidal harmonics $Y_\ell^m(\arccos\eta, \phi)$ form a complete orthonormal set of functions of η and ϕ. The new boundary conditions are found by multiplying the boundary conditions in Eq. (4.4) by the complex conjugate of the spherical harmonics used in the general solution, $[Y_\ell^m(\arccos\eta, \phi)]^*$, and performing an angular integral over the spheroidal surface. For the interface s, we then get from boundary condition (4.4a)

$$\begin{aligned} &\int_{\cap_s} \mathrm{d}\Omega\, [Y_\ell^m(\arccos\eta, \phi)]^* \left\{\psi_{2s-1}(\mathbf{r}) - \psi_{2s+1}(\mathbf{r})\right\}\big|_{\xi=\xi_{0,s}} \\ &+ \int_{\cup_s} \mathrm{d}\Omega\, [Y_\ell^m(\arccos\eta, \phi)]^* \left\{\psi_{2s}(\mathbf{r}) - \psi_{2s+2}(\mathbf{r})\right\}\big|_{\xi=\xi_{0,s}} \\ &= 0 \\ &\forall \quad s = 1, 2, 3, ..., S;\ \ell = 0, 1, 2, 3, ...;\ m = 0, \pm 1, \pm 2, ..., \pm \ell. \end{aligned} \tag{4.36}$$

Similarly, we get from boundary condition (4.4b)

$$\begin{aligned}
&\int_{\cap_s} \mathrm{d}\Omega\, [Y_\ell^m(\arccos\eta,\phi)]^* \left\{ \frac{\partial}{\partial\xi} [\varepsilon_{2s-1}\psi_{2s-1}(\mathbf{r})] \right.\\
&\qquad \left. - \frac{\partial}{\partial\xi} [\varepsilon_{2s+1}\psi_{2s+1}(\mathbf{r})] \right\}\Bigg|_{\xi=\xi_{0,s}} \\
&\qquad + \int_{\cup_s} \mathrm{d}\Omega\, [Y_\ell^m(\arccos\eta,\phi)]^* \left\{ \frac{\partial}{\partial\xi} [\varepsilon_{2s}\psi_{2s}(\mathbf{r})] \right.\\
&\qquad \left. - \frac{\partial}{\partial\xi} [\varepsilon_{2s+2}\psi_{2s+2}(\mathbf{r})] \right\}\Bigg|_{\xi=\xi_{0,s}} \\
&= 0 \\
&\quad \forall \quad s = 1,2,3,...,S;\ \ell = 0,1,2,3,...;\ m = 0,\pm 1,\pm 2,...,\pm\ell.
\end{aligned} \tag{4.37}$$

The requirement that the integral of the potential difference times a test function over a surface is zero, is of course a weaker requirement than having the potential difference equal to zero at all points on the surface. Hence the name of the weak formulation of the boundary conditions.

4.7.2. First boundary condition

In the following calculation, more convenient dimensionless versions of the functions $\widetilde{X}_\ell^m(\xi,a)$ and $\widetilde{Z}_\ell^m(\xi,a)$ are introduced, which are distinguished from the previously defined versions by the lack of the parameter a in their parameter list:

$$\widetilde{X}_\ell^m(\xi) \equiv \widetilde{X}_\ell^m(\xi,a)a^{-\ell} \tag{4.38a}$$

$$\widetilde{Z}_\ell^m(\xi) \equiv \widetilde{Z}_\ell^m(\xi,a)a^{\ell+1}. \tag{4.38b}$$

Using Eq. (4.38), the following integrals can now be defined

$$\widetilde{V}_{\ell\ell'}^m[\kappa_z,\xi](\eta_1,\eta_2) \equiv \int_{\eta_1}^{\eta_2} \mathrm{d}\eta P_\ell^m(\eta) P_{\ell'}^m(\eta_\kappa(\xi,\eta)) \widetilde{Z}_{\ell'}^m(\xi_\kappa(\xi,\eta)), \tag{4.39}$$

and

$$\widetilde{W}_{\ell\ell'}^m[\kappa_z,\xi](\eta_1,\eta_2) \equiv \int_{\eta_1}^{\eta_2} \mathrm{d}\eta P_\ell^m(\eta) P_{\ell'}^m(\eta_\kappa(\xi,\eta)) \widetilde{X}_{\ell'}^m(\xi_\kappa(\xi,\eta)). \tag{4.40}$$

Here κ is used as a placeholder for one of the multipole expansion points μ or $\bar{\mu}$.

It may be shown, using Eqs. (4.39) and (4.13) that

$$\int_{\eta_1}^{\eta_2} \mathrm{d}\eta \int_0^{2\pi} \mathrm{d}\phi \, [Y_\ell^m(\arccos\eta,\phi)]^* \, \widetilde{Z}_{\ell'}^{m'}(\xi_\kappa,a) Y_{\ell'}^{m'}(\arccos\eta_\kappa,\phi_\kappa)\big|_{\xi=\xi_{0,s}} \\ = \delta_{mm'}\zeta_{\ell\ell'}^m a^{-\ell'-1} \widetilde{V}_{\ell\ell'}^m[\kappa_z,\xi_{0,s}](\eta_1,\eta_2), \tag{4.41}$$

and similarly, using Eqs. (4.40) and (4.13)

$$\int_{\eta_1}^{\eta_2} \mathrm{d}\eta \int_0^{2\pi} \mathrm{d}\phi \, [Y_\ell^m(\arccos\eta,\phi)]^* \, \widetilde{X}_{\ell'}^{m'}(\xi_\kappa,a) Y_{\ell'}^{m'}(\arccos\eta_\kappa,\phi_\kappa)\big|_{\xi=\xi_{0,s}} \\ = \delta_{mm'}\zeta_{\ell\ell'}^m a^{\ell'} \widetilde{W}_{\ell\ell'}^m[\kappa_z,\xi_{0,s}](\eta_1,\eta_2). \tag{4.42}$$

For the constant terms, one may, by noting that $1 = 2\sqrt{\pi}Y_0^0$ and using the orthonormality of the spherical harmonics, write

$$\int_{-1}^{1} \mathrm{d}\eta \int_0^{2\pi} \mathrm{d}\phi \, [Y_\ell^m(\arccos\eta,\phi)]^* \, \psi_0 = 2\sqrt{\pi}\psi_0\delta_{\ell 0}\delta_{m0}. \tag{4.43}$$

The general form of the potentials in Eqs. (4.32) and (4.33) are now inserted into the first boundary condition in Eq. (4.36) while using the relations in Eqs. (4.41), (4.42) and (4.43). The $A_{\ell'm'}^{(2s-1)}$, $A_{\ell'm'}^{(2s+1)}$, $B_{\ell'm'}^{(2s-1)}$ and $B_{\ell'm'}^{(2s+1)}$ terms are then collected, and by introducing the abbreviations $\mathcal{I}$ and $\mathcal{K}$

$$\mathcal{I}_{\ell\ell'}^{m(i)}(t_r,\xi_0) \equiv \xi_0^{\ell'+1}\Big[\widetilde{V}_{\ell\ell'}^m[\mu,\xi_0](-1,t_r) + (-1)^{\ell'+m}\mathcal{R}_i\widetilde{V}_{\ell\ell'}^m[\bar{\mu},\xi_0](-1,t_r) \\ + \mathcal{T}_i\widetilde{V}_{\ell\ell'}^m[\mu,\xi_0](t_r,1)\Big], \tag{4.44}$$

$$\mathcal{K}_{\ell\ell'}^{m(i)}(t_r,\xi_0) \equiv \xi_0^{-\ell'}\Big[\widetilde{W}_{\ell\ell'}^m[\mu,\xi_0](-1,t_r) + (-1)^{\ell'+m}\mathcal{R}_i\widetilde{W}_{\ell\ell'}^m[\bar{\mu},\xi_0](-1,t_r) \\ + \mathcal{T}_i\widetilde{W}_{\ell\ell'}^m[\mu,\xi_0](t_r,1)\Big], \tag{4.45}$$

it can be shown [1] that the first boundary condition, Eq. (4.36), can be written as

$$
\begin{aligned}
&2\sqrt{\pi}\{\psi_0^{(2s-1)} - \psi_0^{(2s+1)}\}\delta_{\ell 0}\delta_{m0} \\
&\quad + \delta_{s1}\int_{-1}^{t_r^{(1)}} \mathrm{d}\eta \int_0^{2\pi} \mathrm{d}\phi\,[Y_\ell^m(\arccos\eta,\phi)]^*\,\psi_{\mathrm{inc}}(\xi,\eta,\phi)\big|_{\xi=\xi_{0,1}} \\
&\quad + \delta_{s1}\int_{t_r^{(1)}}^{1} \mathrm{d}\eta \int_0^{2\pi} \mathrm{d}\phi\,[Y_\ell^m(\arccos\eta,\phi)]^*\,\psi_{\mathrm{tr}}(\xi,\eta,\phi)\big|_{\xi=\xi_{0,1}} \\
&\quad + \sum_{\ell'=|m|}^{\prime} \zeta_{\ell\ell'}^m R_\perp^{-\ell'-1}\Big[A_{\ell' m}^{(2s-1)}\mathcal{I}_{\ell\ell'}^{m(2s-1)}(t_r^{(s)},\xi_{0,s}) \\
&\quad - A_{\ell' m}^{(2s+1)}\mathcal{I}_{\ell\ell'}^{m(2s+1)}(t_r^{(s)},\xi_{0,s})\Big] \\
&\quad + \sum_{\ell'=|m|}^{\prime} \zeta_{\ell\ell'}^m R_\perp^{\ell'}\Big[B_{\ell' m}^{(2s-1)}\mathcal{K}_{\ell\ell'}^{m(2s-1)}(t_r^{(s)},\xi_{0,s}) \\
&\quad - B_{\ell' m}^{(2s+1)}\mathcal{K}_{\ell\ell'}^{m(2s+1)}(t_r^{(s)},\xi_{0,s})\Big] \\
&= 0.
\end{aligned}
\tag{4.46}
$$

Here it was also used that $R_\perp = a\xi_0$.

The weak formulation of the first boundary condition for the spheroidal interfaces has thus been reduced to a set of linear equations in terms of the two unknown multipole coefficients $A_{\ell m}^{(i)}$ and $B_{\ell m}^{(i)}$ (with i odd).

4.7.3. Second boundary condition

The weak form of the second boundary condition in Eq. (4.4b) on the spheroidal interfaces can be written

$$\begin{aligned}
&\int_{\cap_s} \mathrm{d}\Omega\, [Y_\ell^m(\arccos\eta,\phi)]^* \left\{ \frac{\partial}{\partial\xi} [\varepsilon_{2s-1}\psi_{2s-1}(\mathbf{r})] \right. \\
&\qquad \left. - \frac{\partial}{\partial\xi} [\varepsilon_{2s+1}\psi_{2s+1}(\mathbf{r})] \right\} \Big|_{\xi=\xi_{0,s}} \\
&\qquad + \int_{\cup_s} \mathrm{d}\Omega\, [Y_\ell^m(\arccos\eta,\phi)]^* \left\{ \frac{\partial}{\partial\xi} [\varepsilon_{2s}\psi_{2s}(\mathbf{r})] \right. \\
&\qquad \left. - \frac{\partial}{\partial\xi} [\varepsilon_{2s+2}\psi_{2s+2}(\mathbf{r})] \right\} \Big|_{\xi=\xi_{0,s}} \\
&= 0 \\
&\qquad \forall \quad s = 1,2,3,...,S;\ \ell = 0,1,2,3,...;\ m = 0,\pm1,\pm2,...,\pm\ell.
\end{aligned} \tag{4.47}$$

Using the previously defined integrals in Eqs. (4.39) and (4.40) and the relation in Eq. (4.13) we find that

$$\begin{aligned}
&\int_{\eta_1}^{\eta_2} \mathrm{d}\eta \int_0^{2\pi} \mathrm{d}\phi\, [Y_\ell^m(\arccos\eta,\phi)]^* \frac{\partial}{\partial\xi} \Big\{ \widetilde{Z}_{\ell'}^{m'}(\xi_\kappa, a) Y_{\ell'}^{m'}(\arccos\eta_\kappa, \phi_\kappa) \Big\} \Big|_{\xi=\xi_0} \\
&\qquad = \delta_{mm'} \zeta_{\ell\ell'}^m a^{-\ell'-1} \frac{\partial}{\partial\xi} \Big\{ \widetilde{V}_{\ell\ell'}^m[\kappa_z,\xi](\eta_1,\eta_2) \Big\} \Big|_{\xi=\xi_0},
\end{aligned} \tag{4.48}$$

and

$$\begin{aligned}
&\int_{\eta_1}^{\eta_2} \mathrm{d}\eta \int_0^{2\pi} \mathrm{d}\phi\, [Y_\ell^m(\arccos\eta,\phi)]^* \frac{\partial}{\partial\xi} \Big\{ \widetilde{X}_{\ell'}^{m'}(\xi_\kappa, a) Y_{\ell'}^{m'}(\arccos\eta_\kappa, \phi_\kappa) \Big\} \Big|_{\xi=\xi_0} \\
&\qquad = \delta_{mm'} \zeta_{\ell\ell'}^m a^{\ell'} \frac{\partial}{\partial\xi} \Big\{ \widetilde{W}_{\ell\ell'}^m[\kappa_z,\xi](\eta_1,\eta_2) \Big\} \Big|_{\xi=\xi_0}.
\end{aligned} \tag{4.49}$$

Here κ again is a placeholder for one of the multipole expansion points μ or $\bar{\mu}$.

The expressions for the potentials in the different regions found in Eqs. (4.32) and (4.33) can now be inserted into Eq. (4.47) while using Eqs. (4.48) and (4.49). By collecting the $A_{\ell'm'}^{(2s-1)}$, $A_{\ell'm'}^{(2s+1)}$, $B_{\ell'm'}^{(2s-1)}$ and

$B^{(2s+1)}_{\ell' m'}$ terms and introducing the abbreviations

$$\begin{aligned}\mathcal{J}^{m(i)}_{\ell\ell'}(t_r,\xi_0) \equiv \xi_0^{\ell'+1}\Big[&\varepsilon_i \frac{\partial}{\partial\xi}\Big\{\widetilde{V}^m_{\ell\ell'}[\mu,\xi](-1,t_r)\Big\}\Big|_{\xi=\xi_0} \\ &+(-1)^{\ell'+m}\varepsilon_i\mathcal{R}_i\frac{\partial}{\partial\xi}\Big\{\widetilde{V}^m_{\ell\ell'}[\bar{\mu},\xi](-1,t_r)\Big\}\Big|_{\xi=\xi_0} \\ &+\varepsilon_{i+1}\mathcal{T}_i\frac{\partial}{\partial\xi}\Big\{\widetilde{V}^m_{\ell\ell'}[\mu,\xi](t_r,1)\Big\}\Big|_{\xi=\xi_0}\Big],\end{aligned} \tag{4.50}$$

and

$$\begin{aligned}\mathcal{L}^{m(i)}_{\ell\ell'}(t_r,\xi_0) \equiv \xi_0^{-\ell'}\Big[&\varepsilon_i \frac{\partial}{\partial\xi}\Big\{\widetilde{W}^m_{\ell\ell'}[\mu,\xi](-1,t_r)\Big\}\Big|_{\xi=\xi_0} \\ &+(-1)^{\ell'+m}\varepsilon_i\mathcal{R}_i\frac{\partial}{\partial\xi}\Big\{\widetilde{W}^m_{\ell\ell'}[\bar{\mu},\xi](-1,t_r)\Big\}\Big|_{\xi=\xi_0} \\ &+\varepsilon_{i+1}\mathcal{T}_i\frac{\partial}{\partial\xi}\Big\{\widetilde{W}^m_{\ell\ell'}[\mu,\xi](t_r,1)\Big\}\Big|_{\xi=\xi_0}\Big],\end{aligned} \tag{4.51}$$

it can be shown [1] that the second boundary condition, Eq. (4.37), can be written as

$$\begin{aligned}&\delta_{s1}\varepsilon_1\int_{-1}^{t_r^{(1)}}\mathrm{d}\eta\int_0^{2\pi}\mathrm{d}\phi\,[Y^m_\ell(\arccos\eta,\phi)]^*\,\frac{\partial}{\partial\xi}\Big\{\psi_{\mathrm{inc}}(\xi,\eta,\phi)\Big\}\Big|_{\xi=\xi_{0,1}} \\ &+\delta_{s1}\varepsilon_2\int_{t_r^{(1)}}^{1}\mathrm{d}\eta\int_0^{2\pi}\mathrm{d}\phi\,[Y^m_\ell(\arccos\eta,\phi)]^*\,\frac{\partial}{\partial\xi}\Big\{\psi_{\mathrm{tr}}(\xi,\eta,\phi)\Big\}\Big|_{\xi=\xi_{0,1}} \\ &+\sum_{\ell'=|m|}^{\prime}\zeta^m_{\ell\ell'}R_\perp^{-\ell'-1}\Big[A^{(2s-1)}_{\ell' m}\mathcal{J}^{m(2s-1)}_{\ell\ell'}(t_r^{(s)},\xi_{0,s}) \\ &-A^{(2s+1)}_{\ell' m}\mathcal{J}^{m(2s+1)}_{\ell\ell'}(t_r^{(s)},\xi_{0,s})\Big] \\ &+\sum_{\ell'=|m|}^{\prime}\zeta^m_{\ell\ell'}R_\perp^{\ell'}\Big[B^{(2s-1)}_{\ell' m}\mathcal{L}^{m(2s-1)}_{\ell\ell'}(t_r^{(s)},\xi_{0,s}) \\ &-B^{(2s+1)}_{\ell' m}\mathcal{L}^{m(2s+1)}_{\ell\ell'}(t_r^{(s)},\xi_{0,s})\Big] \\ &=0,\end{aligned} \tag{4.52}$$

where it again was used that $R_\perp = a\xi$.

The weak formulation of the second boundary condition on the spheroidal interfaces has now also been reduced to a set of linear equations in terms of the unknown multipole coefficients $A_{\ell m}^{(i)}$ and $B_{\ell m}^{(i)}$ (with i odd). In order to have a fully determined system, we now only need expressions for the potentials corresponding to the incident and transmitted field, $\psi_{\mathrm{inc}}(\xi, \eta, \phi)$ and $\psi_{\mathrm{tr}}(\xi, \eta, \phi)$. This is treated in the next section.

4.8. Incident potential

The incident electric field, which is assumed to be homogeneous (cf. section 4.1), can be written in Cartesian coordinates as [7]

$$\mathbf{E_0} = [E_{0,x}, E_{0,y}, E_{0,z}] = E_0 \left[\sin\theta_0 \cos\phi_0, \sin\theta_0 \sin\phi_0, \cos\theta_0\right]. \tag{4.53}$$

where θ_0 is the angle between $\mathbf{E_0}$ and the z-axis, and ϕ_0 is the angle between the projection of $\mathbf{E_0}$ on to the substrate and the x-axis. Note that the angle θ_0 is not the same as the angle of incidence θ_i seen in Figure 4.1.

For an incident wave with angles of incidence θ_i and ϕ_i, polarized orthogonal (s) or parallel (p) to the plane of incidence, one finds the following relations for the angles θ_0 and ϕ_0:

$$\begin{aligned}
&s\text{-polarization:} \qquad && \theta_0 = \pi/2 \qquad \text{for all } \theta_i \\
& && \phi_0 = \begin{cases} \phi_i + \pi/2 & \text{if } \phi_i < 3\pi/2 \\ \phi_i - 3\pi/2 & \text{if } \phi_i \geq 3\pi/2 \end{cases} \\
&p\text{-polarization:} && \theta_0 = \pi/2 - \theta_i \qquad \text{for all } \theta_i \\
& && \phi_0 = \begin{cases} \pi - \phi_i & \text{if } \phi_i < \pi \\ \phi_i - \pi & \text{if } \phi_i \geq \pi. \end{cases}
\end{aligned} \tag{4.54}$$

Here it has been used that $\theta_i \in [0, \pi/2]$ and $\phi_i \in [0, 2\pi)$, which ensures that the incident light source is located above the substrate. This also ensures that $\theta_0 \in [0, \pi/2]$ and $\phi_0 \in [0, 2\pi)$.

In prolate spheroidal coordinates, the potential corresponding to this incident field can be written [7]

$$\begin{aligned}\psi_{\text{inc}}(\mathbf{r}) =& -\mathbf{E_0}\cdot\mathbf{r}\\ =& \sqrt{\frac{2\pi}{3}}\Big[-\sqrt{2}E_{0,z}\widetilde{X}_1^0(\xi,a)Y_1^0(\arccos\eta,\phi)\\ &+(E_{0,x}-iE_{0,y})\widetilde{X}_1^1(\xi,a)Y_1^1(\arccos\eta,\phi)\\ &-(E_{0,x}+iE_{0,y})\widetilde{X}_1^{-1}(\xi,a)Y_1^{-1}(\arccos\eta,\phi)\Big]\\ =& \sqrt{\frac{2\pi}{3}}E_0\Big[-\sqrt{2}\cos\theta_0\widetilde{X}_1^0(\xi,a)Y_1^0(\arccos\eta,\phi)\\ &+\sin\theta_0 e^{-i\phi_0}\widetilde{X}_1^1(\xi,a)Y_1^1(\arccos\eta,\phi)\\ &-\sin\theta_0 e^{i\phi_0}\widetilde{X}_1^{-1}(\xi,a)Y_1^{-1}(\arccos\eta,\phi)\Big].\end{aligned} \tag{4.55}$$

The incident radiation is partly transmitted into the substrate. The corresponding potential can be written in prolate spheroidal coordinates

$$\begin{aligned}\psi_{\text{tr}}(\mathbf{r}) = \psi' &+ c_1\widetilde{X}_1^0(\xi,a)Y_1^0(\arccos\eta,\phi)+c_2\widetilde{X}_1^1(\xi,a)Y_1^1(\arccos\eta,\phi)\\ &+c_3\widetilde{X}_1^{-1}(\xi,a)Y_1^{-1}(\arccos\eta,\phi),\end{aligned} \tag{4.56}$$

where ψ', c_1, c_2 and c_2 are constants. Using the boundary conditions in Eq. (4.4) at the interface between the ambient and the substrate at $z = d$, it can be shown that [7]

$$\begin{aligned} c_1 &= -\frac{\varepsilon_1}{\varepsilon_2}\left(\frac{4\pi}{3}\right)^{\frac{1}{2}}E_{0,z} = -E_0\frac{\varepsilon_1}{\varepsilon_2}\left(\frac{4\pi}{3}\right)^{\frac{1}{2}}\cos\theta_0\\ c_2 &= \left(\frac{2\pi}{3}\right)^{\frac{1}{2}}(E_{0,x}-iE_{0,y}) = E_0\left(\frac{2\pi}{3}\right)^{\frac{1}{2}}\sin\theta_0 e^{-i\phi_0}\\ c_3 &= -\left(\frac{2\pi}{3}\right)^{\frac{1}{2}}(E_{0,x}+iE_{0,y}) = -E_0\left(\frac{2\pi}{3}\right)^{\frac{1}{2}}\sin\theta_0 e^{i\phi_0}\\ \psi' &= -d\left(1-\frac{\varepsilon_1}{\varepsilon_2}\right)E_{0,z} = E_0\left(\frac{\varepsilon_1}{\varepsilon_2}-1\right)d\cos\theta_0,\end{aligned} \tag{4.57}$$

and the potential corresponding to the transmitted field becomes

$$\begin{aligned}\psi_{\mathrm{tr}}(\mathbf{r}) = {} & E_0\left(\frac{\varepsilon_1}{\varepsilon_2}-1\right)d\cos\theta_0 \\ & + \sqrt{\frac{2\pi}{3}}E_0\Big[-\frac{\varepsilon_1}{\varepsilon_2}\sqrt{2}\cos\theta_0\widetilde{X}_1^0(\xi,a)Y_1^0(\arccos\eta,\phi) \\ & + \sin\theta_0 e^{-i\phi_0}\widetilde{X}_1^1(\xi,a)Y_1^1(\arccos\eta,\phi) \\ & - \sin\theta_0 e^{i\phi_0}\widetilde{X}_1^{-1}(\xi,a)Y_1^{-1}(\arccos\eta,\phi)\Big]\end{aligned} \tag{4.58}$$

In the next calculations, the following integral abbreviation will be introduced

$$Q_{\ell\ell'}^m(\eta_1,\eta_2) \equiv \int_{\eta_1}^{\eta_2} P_\ell^m(\eta)P_{\ell'}^m(\eta)\mathrm{d}\eta, \tag{4.59}$$

which can be shown, using Eqs. (4.12) and (4.13) to have the following orthogonality property

$$Q_{\ell\ell'}^m(-1,1) = \int_{-1}^{1} P_\ell^m(\eta)P_{\ell'}^m(\eta)\mathrm{d}\eta = \frac{\delta_{\ell\ell'}}{\zeta_{\ell\ell}^m} = \frac{2(\ell+m)!}{(2\ell+1)(\ell-m)!}\delta_{\ell\ell'}, \tag{4.60}$$

which gives

$$Q_{\ell\ell'}^m(-1,t_r^{(s)}) + Q_{\ell\ell'}^m(t_r^{(s)},1) = Q_{\ell\ell'}^m(-1,1) = \frac{\delta_{\ell\ell'}}{\zeta_{\ell\ell}^m}. \tag{4.61}$$

The integral $Q_{\ell\ell'}^m(\eta_1,\eta_2)$ is not to be confused with $Q_\ell^m(\xi)$ defined in section 4.2, which is the associated Legendre function of the second kind.

The integral terms containing the incident and transmitted potentials in Eqs. (4.46) may now be calculated using the expressions in Eqs. (4.55), (4.58) and (4.59):

$$\begin{aligned}&\int_{-1}^{t_r^{(1)}}\mathrm{d}\eta\int_0^{2\pi}\mathrm{d}\phi\,[Y_\ell^m(\arccos\eta,\phi)]^*\,\psi_{\mathrm{inc}}(\xi,\eta,\phi)\big|_{\xi=\xi_{0,1}} \\ &\quad = \sqrt{\frac{2\pi}{3}}E_0 a\Big[-\sqrt{2}\cos\theta_0\delta_{m0}\zeta_{\ell1}^0\widetilde{X}_1^0(\xi_{0,1})Q_{\ell1}^0(-1,t_r^{(1)}) \\ &\quad + \sin\theta_0 e^{-i\phi_0}\delta_{m1}\zeta_{\ell1}^1\widetilde{X}_1^1(\xi_{0,1})Q_{\ell1}^1(-1,t_r^{(1)}) \\ &\quad - \sin\theta_0 e^{i\phi_0}\delta_{m,-1}\zeta_{\ell1}^{-1}\widetilde{X}_1^{-1}(\xi_{0,1})Q_{\ell1}^{-1}(-1,t_r^{(1)})\Big],\end{aligned} \tag{4.62}$$

$$
\begin{aligned}
&\int_{t_r^{(1)}}^{1} \mathrm{d}\eta \int_0^{2\pi} \mathrm{d}\phi \, [Y_\ell^m(\arccos\eta, \phi)]^* \, \psi_{\mathrm{tr}}(\xi, \eta, \phi)\big|_{\xi=\xi_{0,1}} \\
&\quad = \sqrt{\frac{4\pi}{3}} E_0 \cos\theta_0 \bigg[\sqrt{3} \bigg(\frac{\varepsilon_1}{\varepsilon_2} - 1 \bigg) d \zeta_{\ell 0}^0 Q_{\ell 0}^0 (t_r^{(1)}, 1) \\
&\qquad - a \frac{\varepsilon_1}{\varepsilon_2} \widetilde{X}_1^0(\xi_{0,1}) \zeta_{\ell 1}^0 Q_{\ell 1}^0 (t_r^{(1)}, 1) \bigg] \delta_{m0} \\
&\qquad + \sqrt{\frac{2\pi}{3}} E_0 a \Big[\sin\theta_0 e^{-i\phi_0} \delta_{m1} \zeta_{\ell 1}^1 \widetilde{X}_1^1(\xi_{0,1}) Q_{\ell 1}^1 (t_r^{(1)}, 1) \\
&\qquad - \sin\theta_0 e^{i\phi_0} \delta_{m,-1} \zeta_{\ell 1}^{-1} \widetilde{X}_1^{-1}(\xi_{0,1}) Q_{\ell 1}^{-1} (t_r^{(1)}, 1) \Big],
\end{aligned}
\tag{4.63}
$$

Combining these results, while using Eq. (4.61) and the fact that $a = R_{\perp,s}\xi_{0,s}^{-1}$ and $d = t_r^{(s)} R_{\perp,s}$ for all s, gives the following equation

$$
\begin{aligned}
&\int_{-1}^{t_r^{(1)}} \mathrm{d}\eta \int_0^{2\pi} \mathrm{d}\phi \, [Y_\ell^m(\arccos\eta, \phi)]^* \, \psi_{\mathrm{inc}}(\xi, \eta, \phi)\big|_{\xi=\xi_{0,1}} \\
&\quad + \int_{t_r^{(1)}}^{1} \mathrm{d}\eta \int_0^{2\pi} \mathrm{d}\phi \, [Y_\ell^m(\arccos\eta, \phi)]^* \, \psi_{\mathrm{tr}}(\xi, \eta, \phi)\big|_{\xi=\xi_{0,1}} \\
&\quad = -R_{\perp,1} \sqrt{\frac{4\pi}{3}} E_0 \cos\theta_0 \bigg\{ \xi_{0,1}^{-1} \frac{\varepsilon_1}{\varepsilon_2} \widetilde{X}_1^0(\xi_{0,1}) \delta_{\ell 1} \\
&\quad + \bigg(\frac{\varepsilon_1}{\varepsilon_2} - 1 \bigg) \Big[\sqrt{3} t_r^{(1)} \zeta_{\ell 0}^0 Q_{\ell 0}^0 (-1, t_r^{(1)}) \\
&\quad - \xi_{0,1}^{-1} \zeta_{\ell 1}^0 \widetilde{X}_1^0(\xi_{0,1}) Q_{\ell 1}^0 (-1, t_r^{(1)}) - \sqrt{3} t_r^{(1)} \delta_{\ell 0} \Big] \bigg\} \delta_{m0} \\
&\quad + R_{\perp,1} \sqrt{\frac{2\pi}{3}} E_0 \xi_{0,1}^{-1} \Big[\sin\theta_0 e^{-i\phi_0} \widetilde{X}_1^1(\xi_{0,1}) \delta_{m1} \delta_{\ell 1} \\
&\quad - \sin\theta_0 e^{i\phi_0} \widetilde{X}_1^{-1}(\xi_{0,1}) \delta_{m,-1} \delta_{\ell 1} \Big].
\end{aligned}
\tag{4.64}
$$

Similarly, we have for the integral terms containing the normal derivatives of the incident and transmitted potential in Eq. (4.52),

$$\begin{aligned}&\int_{-1}^{t_r^{(1)}} \mathrm{d}\eta \int_0^{2\pi} \mathrm{d}\phi\, [Y_\ell^m(\arccos\eta,\phi)]^* \,\frac{\partial}{\partial\xi}\Big\{\psi_{\mathrm{inc}}(\xi,\eta,\phi)\Big\}\Big|_{\xi=\xi_{0,1}} \\ &\quad= \sqrt{\frac{2\pi}{3}} E_0 a\Big\{-\sqrt{2}\cos\theta_0\delta_{m0}\zeta_{\ell 1}^0 \frac{\partial \widetilde{X}_1^0(\xi)}{\partial\xi}\Big|_{\xi=\xi_{0,1}} Q_{\ell 1}^0(-1,t_r^{(1)}) \\ &\qquad+\sin\theta_0 e^{-i\phi_0}\delta_{m1}\zeta_{\ell 1}^1 \frac{\partial \widetilde{X}_1^1(\xi)}{\partial\xi}\Big|_{\xi=\xi_{0,1}} Q_{\ell 1}^1(-1,t_r^{(1)}) \\ &\qquad-\sin\theta_0 e^{i\phi_0}\delta_{m,-1}\zeta_{\ell 1}^{-1} \frac{\partial \widetilde{X}_1^{-1}(\xi)}{\partial\xi}\Big|_{\xi=\xi_{0,1}} Q_{\ell 1}^{-1}(-1,t_r^{(1)})\Big\},\end{aligned} \tag{4.65}$$

and

$$\begin{aligned}&\int_{t_r^{(1)}}^{1} \mathrm{d}\eta \int_0^{2\pi} \mathrm{d}\phi\, [Y_\ell^m(\arccos\eta,\phi)]^* \,\frac{\partial}{\partial\xi}\Big\{\psi_{\mathrm{tr}}(\xi,\eta,\phi)\Big\}\Big|_{\xi=\xi_{0,1}} \\ &\quad= \sqrt{\frac{2\pi}{3}} E_0 a\Big\{-\sqrt{2}\frac{\varepsilon_1}{\varepsilon_2}\cos\theta_0\delta_{m0}\zeta_{\ell 1}^0 \frac{\partial \widetilde{X}_1^0(\xi)}{\partial\xi}\Big|_{\xi=\xi_{0,1}} Q_{\ell 1}^0(t_r^{(1)},1) \\ &\qquad+\sin\theta_0 e^{-i\phi_0}\delta_{m1}\zeta_{\ell 1}^1 \frac{\partial \widetilde{X}_1^1(\xi)}{\partial\xi}\Big|_{\xi=\xi_{0,1}} Q_{\ell 1}^1(t_r^{(1)},1) \\ &\qquad-\sin\theta_0 e^{i\phi_0}\delta_{m,-1}\zeta_{\ell 1}^{-1} \frac{\partial \widetilde{X}_1^{-1}(\xi)}{\partial\xi}\Big|_{\xi=\xi_{0,1}} Q_{\ell 1}^{-1}(t_r^{(1)},1)\Big\}.\end{aligned} \tag{4.66}$$

Combining these, we get

$$\begin{aligned}&\varepsilon_1\int_{-1}^{t_r^{(1)}} \mathrm{d}\eta \int_0^{2\pi} \mathrm{d}\phi\, [Y_\ell^m(\arccos\eta,\phi)]^* \,\frac{\partial}{\partial\xi}\Big\{\psi_{\mathrm{inc}}(\xi,\eta,\phi)\Big\}\Big|_{\xi=\xi_{0,1}} \\ &+\varepsilon_2\int_{t_r^{(1)}}^{1} \mathrm{d}\eta \int_0^{2\pi} \mathrm{d}\phi\, [Y_\ell^m(\arccos\eta,\phi)]^* \,\frac{\partial}{\partial\xi}\Big\{\psi_{\mathrm{tr}}(\xi,\eta,\phi)\Big\}\Big|_{\xi=\xi_{0,1}} \\ &= -R_{\perp,1}\varepsilon_1\sqrt{\frac{4\pi}{3}}E_0\xi_{0,1}^{-1}\cos\theta_0\frac{\partial \widetilde{X}_1^0(\xi)}{\partial\xi}\Big|_{\xi=\xi_{0,1}}\delta_{m0}\delta_{\ell 1} \\ &+R_{\perp,1}\sqrt{\frac{2\pi}{3}}E_0\xi_{0,1}^{-1}\sin\theta_0 e^{-i\phi_0}\frac{\partial \widetilde{X}_1^1(\xi)}{\partial\xi}\Big|_{\xi=\xi_{0,1}} \\ &\times\Big((\varepsilon_1-\varepsilon_2)\zeta_{\ell 1}^1 Q_{\ell 1}^1(-1,t_r^{(1)})+\varepsilon_2\delta_{\ell 1}\Big)\delta_{m1} \\ &-R_{\perp,1}\sqrt{\frac{2\pi}{3}}E_0\xi_{0,1}^{-1}\sin\theta_0 e^{i\phi_0}\frac{\partial \widetilde{X}_1^{-1}(\xi)}{\partial\xi}\Big|_{\xi=\xi_{0,1}} \\ &\times\Big((\varepsilon_1-\varepsilon_2)\zeta_{\ell 1}^{-1} Q_{\ell 1}^{-1}(-1,t_r^{(1)})+\varepsilon_2\delta_{\ell 1}\Big)\delta_{m,-1}.\end{aligned} \tag{4.67}$$

4.9. Linear set of equations for the potential expansion coefficients

The integrals containing the incident and transmitted potentials in the ambient and substrate have now been expressed in terms of known quantities, and their expressions in Eqs. (4.64) and (4.67) may be combined with the results found in section 4.7. We then get the following linear set of equations for the unknown multipole expansion coefficients $A^{(i)}_{\ell m}$ and $B^{(i)}_{\ell m}$:

$$
\begin{aligned}
&{\sum_{\ell'=|m|}}' \zeta^{m}_{\ell\ell'} R_{\perp,s}^{-\ell'-2}\left[A^{(2s-1)}_{\ell' m}\mathcal{I}^{m(2s-1)}_{\ell\ell'}(t_r^{(s)},\xi_{0,s}) - A^{(2s+1)}_{\ell' m}\mathcal{I}^{m(2s+1)}_{\ell\ell'}(t_r^{(s)},\xi_{0,s})\right] \\
&+ {\sum_{\ell'=|m|}}' \zeta^{m}_{\ell\ell'} R_{\perp,s}^{\ell'-1}\left[B^{(2s-1)}_{\ell' m}\mathcal{K}^{m(2s-1)}_{\ell\ell'}(t_r^{(s)},\xi_{0,s}) - B^{(2s+1)}_{\ell' m}\mathcal{K}^{m(2s+1)}_{\ell\ell'}(t_r^{(s)},\xi_{0,s})\right] \\
&= \delta_{s1}\sqrt{\frac{4\pi}{3}}E_0\cos\theta_0\Bigg\{\xi_{0,1}^{-1}\frac{\varepsilon_1}{\varepsilon_2}\widetilde{X}^{0}_{1}(\xi_{0,1})\delta_{\ell 1} \\
&+ \left(\frac{\varepsilon_1}{\varepsilon_2}-1\right)\Big[\sqrt{3}t_r^{(1)}\zeta^{0}_{\ell 0}Q^{0}_{\ell 0}(-1,t_r^{(1)}) \\
&- \xi_{0,1}^{-1}\zeta^{0}_{\ell 1}\widetilde{X}^{0}_{1}(\xi_{0,1})Q^{0}_{\ell 1}(-1,t_r^{(1)}) - \sqrt{3}t_r^{(1)}\delta_{\ell 0}\Big]\Bigg\}\delta_{m0} \\
&- \delta_{s1}\sqrt{\frac{2\pi}{3}}E_0\xi_{0,1}^{-1}\Big[\sin\theta_0 e^{-i\phi_0}\widetilde{X}^{1}_{1}(\xi_{0,1})\delta_{m1}\delta_{\ell 1} \\
&- \sin\theta_0 e^{i\phi_0}\widetilde{X}^{-1}_{1}(\xi_{0,1})\delta_{m,-1}\delta_{\ell 1}\Big] - \frac{2\sqrt{\pi}}{R_{\perp,s}}\{\psi_0^{(2s-1)} - \psi_0^{(2s+1)}\}\delta_{\ell 0}\delta_{m0} \\
&\forall\ s = 1,2,...,S;\ \ell = 0,1,2,...;\ m = 0,\pm 1,\pm 2,...,\pm\ell,
\end{aligned}
\tag{4.68}
$$

and

$$\begin{aligned}
&\sum^{\prime}_{\ell'=|m|} \zeta^{m}_{\ell\ell'} R^{-\ell'-2}_{\perp,s} \Big[A^{(2s-1)}_{\ell' m} \mathcal{J}^{m(2s-1)}_{\ell\ell'}(t^{(s)}_r, \xi_{0,s}) - A^{(2s+1)}_{\ell' m} \mathcal{J}^{m(2s+1)}_{\ell\ell'}(t^{(s)}_r, \xi_{0,s}) \Big] \\
&+ \sum^{\prime}_{\ell'=|m|} \zeta^{m}_{\ell\ell'} R^{\ell'-1}_{\perp,s} \Big[B^{(2s-1)}_{\ell' m} \mathcal{L}^{m(2s-1)}_{\ell\ell'}(t^{(s)}_r, \xi_{0,s}) - B^{(2s+1)}_{\ell' m} \mathcal{L}^{m(2s+1)}_{\ell\ell'}(t^{(s)}_r, \xi_{0,s}) \Big] \\
&= \delta_{s1} E_0 \xi^{-1}_{0,1} \Bigg\{ \varepsilon_1 \sqrt{\frac{4\pi}{3}} \cos\theta_0 \frac{\partial \widetilde{X}^0_1(\xi)}{\partial \xi}\bigg|_{\xi=\xi_{0,1}} \delta_{m0}\delta_{\ell 1} \\
&- \sqrt{\frac{2\pi}{3}} \sin\theta_0 e^{-i\phi_0} \frac{\partial \widetilde{X}^1_1(\xi)}{\partial \xi}\bigg|_{\xi=\xi_{0,1}} \Big((\varepsilon_1 - \varepsilon_2) \zeta^1_{\ell 1} Q^1_{\ell 1}(-1, t^{(1)}_r) + \varepsilon_2 \delta_{\ell 1} \Big) \delta_{m1} \\
&+ \sqrt{\frac{2\pi}{3}} \sin\theta_0 e^{i\phi_0} \frac{\partial \widetilde{X}^{-1}_1(\xi)}{\partial \xi}\bigg|_{\xi=\xi_{0,1}} \Big((\varepsilon_1 - \varepsilon_2) \zeta^{-1}_{\ell 1} Q^{-1}_{\ell 1}(-1, t^{(1)}_r) \\
&+ \varepsilon_2 \delta_{\ell 1} \Big) \delta_{m,-1} \Bigg\} \\
&\forall\; s = 1, 2, ..., S;\ \ell = 0, 1, 2, ...;\ m = 0, \pm 1, \pm 2, ..., \pm \ell.
\end{aligned} \tag{4.69}$$

From the above equations one can now make a couple of important observations. First, there is no coupling between m-values, therefore a system of equations can be set up for each m separately. This is due to the rotational symmetry of our system around the z-axis. Second, the right hand sides are only non-zero for $m = 0, \pm 1$, because the potential corresponding to the incident electric field only has non-zero terms for these values of m. Hence, all $A^{(i)}_{\ell m}$ and $B^{(i)}_{\ell m}$ with $|m| > 1$ are independent of E_0. If $E_0 = 0$, the potential must be homogeneous, since we have no net charge in our system, and all expansion coefficients are therefore zero in this case. Since the expansion coefficients with $|m| > 1$ are independent of E_0, these must thus be equal to zero in order to fulfil this requirement. We can therefore conclude that

$$\begin{aligned} &A^{(i)}_{\ell m} = B^{(i)}_{\ell m} = 0 \\ &\text{for } |m| > 1 \end{aligned} \tag{4.70}$$

It turns out that only the system of equations for $m = 0$ and $m = 1$ are actually needed. This is due to the fact that the matrix elements are symmetric to a change of sign in m, and the coefficients for positive and negative m are therefore equal, except for a phase factor [7]. We can choose to use $m = 1$, and the system corresponding to $m = -1$ is then redundant.

In order to ensure that the potential is finite everywhere, some of the expansion coefficients must be set to zero immediately. In particular, this is the case for $A_{\ell m}$ in regions where $\xi \to 1$ and $B_{\ell m}$ in regions where $\xi \to \infty$. We therefore have

$$\begin{aligned} A_{\ell m}^{(2S+1)} &= 0 \\ B_{\ell m}^{(1)} &= 0 \end{aligned} \tag{4.71}$$

where the numbering convention introduced in section 3.4 is still used, such that medium $2S+1$ is the innermost medium above the substrate, *i.e.* the medium containing the expansion point. Note that there is not a single point where $\xi \to 1$, but rather a line of length $2a$ along the z-axis.

In theory, the multipole expansion introduced contains an infinite number of terms. In practice, however, we must truncate this infinite sum at some point in order to solve the system numerically. We must therefore introduce a *multipole order* M and in the following neglect all multipole coefficients $A_{\ell' m}^{(i)}$ and $B_{\ell' m}^{(i)}$ with $\ell' > M$. We will then have $4M$ unknown coefficients for each s. In order to have a matching number of equations for these unknowns, ℓ must also have the same restriction, *i.e.* $\ell \leq M$.

Because there is no net charge in the island, the multipole coefficients are all zero for $\ell' = 0$. We can therefore solve the system of equations for the unknown coefficients by considering the cases $1 \leq \ell \leq M$, and treat the set of equations with $\ell = 0$ as a separate case. For $\ell > 1$ the set of equations for the expansion coefficients $A_{\ell' m}^{(i)}$ and $B_{\ell' m}^{(i)}$ now takes the form

$$\begin{aligned} &\sum_{\ell'=1}^{M} \zeta_{\ell\ell'}^{m} R_{\perp,s}^{-\ell'-2} \Big[A_{\ell' m}^{(2s-1)} \mathcal{I}_{\ell\ell'}^{m(2s-1)}(t_r^{(s)}, \xi_{0,s}) - A_{\ell' m}^{(2s+1)} \mathcal{I}_{\ell\ell'}^{m(2s+1)}(t_r^{(s)}, \xi_{0,s}) \Big] \\ &+ \sum_{\ell'=1}^{M} \zeta_{\ell\ell'}^{m} R_{\perp,s}^{\ell'-1} \Big[B_{\ell' m}^{(2s-1)} \mathcal{K}_{\ell\ell'}^{m(2s-1)}(t_r^{(s)}, \xi_{0,s}) - B_{\ell' m}^{(2s+1)} \mathcal{K}_{\ell\ell'}^{m(2s+1)}(t_r^{(s)}, \xi_{0,s}) \Big] \\ &= \delta_{s1} \sqrt{\frac{4\pi}{3}} E_0 \cos\theta_0 \Bigg\{ \xi_{0,1}^{-1} \frac{\varepsilon_1}{\varepsilon_2} \widetilde{X}_1^0(\xi_{0,1}) \delta_{\ell 1} \\ &+ \left(\frac{\varepsilon_1}{\varepsilon_2} - 1 \right) \Big[\sqrt{3} t_r^{(1)} \zeta_{\ell 0}^{0} Q_{\ell 0}^{0}(-1, t_r^{(1)}) \\ &- \xi_{0,1}^{-1} \zeta_{\ell 1}^{0} \widetilde{X}_1^0(\xi_{0,1}) Q_{\ell 1}^{0}(-1, t_r^{(1)}) \Big] \Bigg\} \delta_{m0} \\ &- \delta_{s1} \sqrt{\frac{2\pi}{3}} E_0 \xi_{0,1}^{-1} \sin\theta_0 e^{-i\phi_0} \widetilde{X}_1^1(\xi_{0,1}) \delta_{\ell 1} \delta_{m1} \\ &\forall\ s = 1, 2, ..., S;\ \ell = 0, 1, 2, ..., M;\ m = 0, 1, \end{aligned} \tag{4.72}$$

and

$$\begin{aligned}
&\sum_{\ell'=1}^{M} \zeta_{\ell\ell'}^{m} R_{\perp,s}^{-\ell'-2}\Big[A_{\ell'm}^{(2s-1)}\mathcal{J}_{\ell\ell'}^{m(2s-1)}(t_r^{(s)},\xi_{0,s}) - A_{\ell'm}^{(2s+1)}\mathcal{J}_{\ell\ell'}^{m(2s+1)}(t_r^{(s)},\xi_{0,s})\Big] \\
&+\sum_{\ell'=1}^{M} \zeta_{\ell\ell'}^{m} R_{\perp,s}^{\ell'-1}\Big[B_{\ell'm}^{(2s-1)}\mathcal{L}_{\ell\ell'}^{m(2s-1)}(t_r^{(s)},\xi_{0,s}) - B_{\ell'm}^{(2s+1)}\mathcal{L}_{\ell\ell'}^{m(2s+1)}(t_r^{(s)},\xi_{0,s})\Big] \\
&= \delta_{s1}E_0\xi_{0,1}^{-1}\Bigg\{\varepsilon_1\sqrt{\frac{4\pi}{3}}\cos\theta_0\left.\frac{\partial\widetilde{X}_1^0(\xi)}{\partial\xi}\right|_{\xi=\xi_{0,1}}\delta_{m0}\delta_{\ell1} \\
&-\sqrt{\frac{2\pi}{3}}\sin\theta_0 e^{-i\phi_0}\left.\frac{\partial\widetilde{X}_1^1(\xi)}{\partial\xi}\right|_{\xi=\xi_{0,1}}\Big((\varepsilon_1-\varepsilon_2)\zeta_{\ell1}^{1}Q_{\ell1}^{1}(-1,t_r^{(1)})+\varepsilon_2\delta_{\ell1}\Big)\delta_{m1}\Bigg\} \\
&\forall\ s=1,2,...,S;\ \ell=0,1,2,...,M;\ m=0,1.
\end{aligned} \tag{4.73}$$

Once the expansion coefficients $A_{\ell'0}^{(i)}$ and $B_{\ell'0}^{(i)}$ have been found by solving the set of equations in Eqs. (4.72) and (4.73), the case $\ell=0$ can be used to determine the constants ψ_0^{2s-1} and ψ_0^{2s+1} in Eq. (4.68).

$$\begin{aligned}
&\Big[\psi_0^{(2s+1)}-\psi_0^{(2s-1)}\Big] \\
&=\frac{1}{2\sqrt{\pi}}\sum_{\ell'=1}^{M}\zeta_{0\ell'}^{0}R_{\perp,s}^{-\ell'-1}\Big[A_{\ell'0}^{(2s-1)}\mathcal{I}_{0\ell'}^{0(2s-1)}(t_r^{(s)},\xi_{0,s}) \\
&-A_{\ell'0}^{(2s+1)}\mathcal{I}_{0\ell'}^{0(2s+1)}(t_r^{(s)},\xi_{0,s})\Big] \\
&+\frac{1}{2\sqrt{\pi}}\sum_{\ell'=1}^{M}\zeta_{0\ell'}^{0}R_{\perp,s}^{\ell'}\Big[B_{\ell'0}^{(2s-1)}\mathcal{K}_{0\ell'}^{0(2s-1)}(t_r^{(s)},\xi_{0,s}) \\
&-B_{\ell'0}^{(2s+1)}\mathcal{K}_{0\ell'}^{0(2s+1)}(t_r^{(s)},\xi_{0,s})\Big] \\
&+\delta_{s1}R_{\perp,s}E_0\cos\theta_0\left(\frac{\varepsilon_1}{\varepsilon_2}-1\right)\Bigg\{\frac{1}{\sqrt{3}}\zeta_{01}^{0}Q_{01}^{0}(-1,t_r^{(1)}) \\
&+t_r^{(1)}\Big[1-\zeta_{00}^{0}Q_{00}^{0}(-1,t_r^{(1)})\Big]\Bigg\} \\
&\forall\quad s=1,2,3,...,S,
\end{aligned} \tag{4.74}$$

where it was used that $\xi^{-1}\widetilde{X}_1^0(\xi)=1$. We are only interested in potential *differences*, and may therefore set a reference point for the potential by letting the constant term in the ambient, $\psi_0^{(1)}$, be zero. The constant terms in all other regions may then be calculated from Eq. (4.74).

When the multipole expansion coefficients have been found by solving the linear set of equations in Eqs. (4.72) and (4.73), the island polarizability and surface susceptibilities can be found. This is treated in the next sections. By inserting the multipole expansion coefficients into the general solutions in Eqs. (4.26) and (4.27), and calculating the constant term from Eq. (4.74), the potential in any region of the system can now also be found.

4.10. Island polarizability

The linear response of an island to an electric field is given by [7]

$$\mathbf{P}(\mathbf{r},\omega) = \int \boldsymbol{\alpha}(\mathbf{r}',\omega|\mathbf{r}) \cdot \mathbf{E}(\mathbf{r}',\omega)\mathrm{d}\mathbf{r}', \tag{4.75}$$

where $\mathbf{P}$ is the polarization, $\mathbf{E}$ is the electric field and $\boldsymbol{\alpha}(\mathbf{r}',\omega|\mathbf{r})$ is the polarizability matrix. Since we are interested in the field due to the polarization as seen far from the island, it is convenient to expand the polarizability $\boldsymbol{\alpha}$ as a multipole expansion too. For calculating the first and second order surface susceptibilites, we only need the dipole and quadrupole terms in this expansion. In our case, these dipole and quadrupole polarizabilities of the spheroids can be given in terms of the potential expansion coefficients $A_{10}^{(1)}$, $A_{11}^{(1)}$, $A_{20}^{(1)}$ and $A_{21}^{(1)}$ [7]

$$\begin{aligned}
\alpha_z &= \frac{2\pi\varepsilon_1}{\sqrt{\pi/3}E_0\cos\theta_0} A_{10}^{(1)} \\
\alpha_\parallel &= -\frac{\pi\varepsilon_1}{\sqrt{2\pi/3}E_0\sin\theta_0\exp(-i\phi_0)} A_{11}^{(1)} \\
\alpha_z^{10} &= \frac{\pi\varepsilon_1}{\sqrt{\pi/5}E_0\cos\theta_0} A_{20}^{(1)} \\
\alpha_\parallel^{10} &= -\frac{\pi\varepsilon_1}{\sqrt{6\pi/5}E_0\sin\theta_0\exp(-i\phi_0)} A_{21}^{(1)}.
\end{aligned} \tag{4.76}$$

Note that the polarizabilities are actually independent of E_0, θ_0 and ϕ_0, since $A_{\ell 0}$ are proportional to $E_0\cos\theta_0$ and $A_{\ell 1}$ is proportional to $E_0\sin\theta_0\exp(-i\phi_0)$. Hence, the polarizabilities are independent of the incident field $\mathbf{E_0}$.

One could be led to believe that since we only need the first four multipole expansion coefficients for the calculation of the polarizabilities, it is sufficient to truncate the linear set of equations in Eqs. (4.72) – (4.73) to $M = 2$. This is, however, not the case, since the multipole order determines the accuracy to which the coefficients are calculated. The sum should only be truncated at the M which gives the expansion coefficients with the desired accuracy.

The calculations in this chapter have been based on the assumption that the island film is of low coverage, and that the distance between individual islands therefore is relatively high compared to the size of the islands. Interactions between islands could therefore be neglected. In the case of higher coverage this assumption is no longer valid, and one must take into account interactions between islands and their images. As a first approximation, one can introduce interactions to dipolar order, since these have the longest range. It can be shown that this first order approximation will lead to a correction factor to the polarizabilities found above [7].

4.11. Surface susceptibilities

In section 2.2, the optical reflection and transmission coefficients of a thin film such as the one treated here were found in terms of a set of surface susceptibilities. These susceptibilities are related to the polarizabilities found in section 4.10. The first order surface susceptibilities γ and β are proportional to the dipole polarizability, while the second order susceptibilities δ and τ are linear combinations of the dipole and quadrupole polarizabilities. The second order susceptibilities take into account spatial dispersion, *i.e.* the fact that the expansion point of the polarizability is located a distance $|d - \mu_z|$ above the *reference surface*, located at the substrate surface. In our case the surface susceptibilities are given by [7]

$$\begin{aligned}
\beta &= \rho\alpha_z/\varepsilon_1^2 \\
\gamma &= \rho\alpha_{\parallel} \\
\delta &= -\rho\left[\alpha_z^{10} + \alpha_{\parallel}^{10} - (|d-\mu_z|)\,\alpha_z - (|d-\mu_z|)\,\alpha_{\parallel}\right]/\varepsilon_1 \\
\tau &= -\rho\left[\alpha_{\parallel}^{10} - (|d-\mu_z|)\,\alpha_{\parallel}\right],
\end{aligned} \tag{4.77}$$

where ρ is the island density, *i.e.* the number of islands per unit area.

5. Special cases

In order to verify that the expressions for the potential expansion derived in chapter 4 are actually correct, it is useful to reduce the results to other cases previously calculated by others. If the expressions agree in these limits, this is a good indicator that they may also be correct in the general case.

For the problem of a truncated and coated prolate spheroid on a substrate, there are two special cases that are natural to compare with

i) An uncoated, truncated prolate spheroid on a substrate.

ii) A coated, truncated sphere on a substrate.

In this chapter, these two special cases are treated, and the set of equations derived in chapter 4 are shown to be equal to the sets of equations in these cases, in the corresponding limits. Case *i)* is treated in section 5.1, while case *ii)* is treated in section 5.2.

5.1. Multipoles in center and no coating

The case of uncoated, truncated prolate spheroids where the multipole expansion points have been placed in the center of the spheroid has been solved in [7].

When there is no coating, $S = 1$, and the number of spheroidal interfaces reduces to one. In this case the superscripts dependent of s may be dropped. From Eq. (4.71) we see that in the case of $S = 1$ we have

$$\begin{aligned} A^{(3)}_{\ell' m} &= 0 \\ B^{(1)}_{\ell' m} &= 0. \end{aligned} \tag{5.1}$$

Placing the multipoles in the center of the spheroid, *i.e.* the origin, is equivalent to setting

$$\begin{aligned}\mu_z &= 0\\ \bar{\mu}_z &= 2d.\end{aligned} \tag{5.2}$$

Using this it can be shown that

$$\widetilde{V}^m_{\ell\ell'}[\mu_z = 0, \xi](\eta_1, \eta_2) = \widetilde{Z}^m_{\ell'}(\xi) Q^m_{\ell\ell'}(\eta_1, \eta_2) \tag{5.3}$$

and

$$\widetilde{W}^m_{\ell\ell'}[\mu_z = 0, \xi](\eta_1, \eta_2) = \widetilde{X}^m_{\ell'}(\xi) Q^m_{\ell\ell'}(\eta_1, \eta_2), \tag{5.4}$$

with $Q^m_{\ell\ell'}$ as defined in Eq. (4.59). Using Eqs. (5.3) and (5.4) together with Eqs. (4.31) and (4.61), the abbreviations in Eqs. (4.44), (4.45), (4.50), (4.51) can now be reduced to

$$\begin{aligned}\mathcal{I}^{m(1)}_{\ell\ell'}(t_r, \xi_0) = \frac{\xi_0^{\ell'+1}}{\zeta^m_{\ell\ell'}} \Bigg\{ & \frac{2\varepsilon_1}{\varepsilon_1 + \varepsilon_2} \widetilde{Z}^m_{\ell'}(\xi_0) \delta_{\ell\ell'} \\ & + \frac{\varepsilon_1 - \varepsilon_2}{\varepsilon_1 + \varepsilon_2} \zeta^m_{\ell\ell'} \left[(-1)^{\ell'+m'} \widetilde{V}^m_{\ell\ell'}[\bar{\mu}, \xi_0](-1, t_r) - \widetilde{Z}^m_{\ell'}(\xi_0) Q^m_{\ell\ell'}(-1, t_r) \right] \Bigg\},\end{aligned} \tag{5.5}$$

$$\begin{aligned}\mathcal{K}^{m(3)}_{\ell\ell'}(t_r, \xi_0) = \frac{\xi_0^{-\ell'}}{\zeta^m_{\ell\ell'}} \Bigg\{ & \frac{2\varepsilon_3}{\varepsilon_3 + \varepsilon_4} \widetilde{X}^m_{\ell'}(\xi_0) \delta_{\ell\ell'} \\ & + \frac{\varepsilon_3 - \varepsilon_4}{\varepsilon_3 + \varepsilon_4} \zeta^m_{\ell\ell'} \left[(-1)^{\ell'+m'} \widetilde{W}^m_{\ell\ell'}[\bar{\mu}, \xi_0](-1, t_r) - \widetilde{X}^m_{\ell'}(\xi_0) Q^m_{\ell\ell'}(-1, t_r) \right] \Bigg\},\end{aligned} \tag{5.6}$$

$$\begin{aligned}\mathcal{J}^{m(1)}_{\ell\ell'}(t_r, \xi_0) = \frac{\xi_0^{\ell'+1}}{\zeta^m_{\ell\ell'}} \varepsilon_1 \Bigg\{ & \delta_{\ell\ell'} \frac{2\varepsilon_2}{\varepsilon_1 + \varepsilon_2} \frac{\partial}{\partial \xi} \left(\widetilde{Z}^m_{\ell'}(\xi) \right) \Big|_{\xi=\xi_0} \\ & + \frac{\varepsilon_1 - \varepsilon_2}{\varepsilon_1 + \varepsilon_2} \zeta^m_{\ell\ell'} \Bigg[Q^m_{\ell\ell'}(-1, t_r) \frac{\partial}{\partial \xi} \left(\widetilde{Z}^m_{\ell'}(\xi) \right) \Big|_{\xi=\xi_0} \\ & + (-1)^{\ell'+m'} \frac{\partial}{\partial \xi} \left(\widetilde{V}^m_{\ell\ell'}[\bar{\mu}, \xi](-1, t_r) \right) \Big|_{\xi=\xi_0} \Bigg] \Bigg\},\end{aligned} \tag{5.7}$$

$$\begin{aligned}\mathcal{L}^{m(3)}_{\ell\ell'}(t_r, \xi_0) = \frac{\xi_0^{-\ell'}}{\zeta^m_{\ell\ell'}} \varepsilon_3 \Bigg\{ & \delta_{\ell\ell'} \frac{2\varepsilon_4}{\varepsilon_3 + \varepsilon_4} \frac{\partial}{\partial \xi} \left(\widetilde{X}^m_{\ell'}(\xi) \right) \Big|_{\xi=\xi_0} \\ & + \frac{\varepsilon_3 - \varepsilon_4}{\varepsilon_3 + \varepsilon_4} \zeta^m_{\ell\ell'} \Bigg[Q^m_{\ell\ell'}(-1, t_r) \frac{\partial}{\partial \xi} \left(\widetilde{X}^m_{\ell'}(\xi) \right) \Big|_{\xi=\xi_0} \\ & + (-1)^{\ell'+m'} \frac{\partial}{\partial \xi} \left(\widetilde{W}^m_{\ell\ell'}[\bar{\mu}, \xi](-1, t_r) \right) \Big|_{\xi=\xi_0} \Bigg] \Bigg\}.\end{aligned} \tag{5.8}$$

The linear set of equations in Eqs. (4.72) and (4.73) now reduces to

$$\begin{aligned}
&\sum_{\ell'=1}^{M} \zeta_{\ell\ell'}^{m} R_{\perp}^{-\ell'-2} A_{\ell' m}^{(1)} \mathcal{I}_{\ell\ell'}^{m(1)}(t_r,\xi_0) - \sum_{\ell'=1}^{M} \zeta_{\ell\ell'}^{m} R_{\perp}^{\ell'-1} B_{\ell' m}^{(3)} \mathcal{K}_{\ell\ell'}^{m(3)}(t_r,\xi_0) \\
&= \sqrt{\frac{4\pi}{3}} E_0 \cos\theta_0 \Bigg\{ \xi_0^{-1} \frac{\varepsilon_1}{\varepsilon_2} \widetilde{X}_1^0(\xi_0)\delta_{\ell 1} + \left(\frac{\varepsilon_1}{\varepsilon_2} - 1\right) \Big[\sqrt{3} t_r \zeta_{\ell 0}^{0} Q_{\ell 0}^{0}(-1,t_r) \\
&- \xi_{0,1}^{-1} \zeta_{\ell 1}^{0} \widetilde{X}_1^0(\xi_{0,1}) Q_{\ell 1}^{0}(-1,t_r^{(1)}) \Big] \Bigg\} \delta_{m0} \\
&- \sqrt{\frac{2\pi}{3}} E_0 \xi_0^{-1} \sin\theta_0 e^{-i\phi_0} \widetilde{X}_1^1(\xi_0) \delta_{m1}\delta_{\ell 1} \\
&\forall\ \ell = 1,2,3,...,M; \quad m = 0,1,
\end{aligned} \tag{5.9}$$

and

$$\begin{aligned}
&\sum_{\ell'=1}^{M} \zeta_{\ell\ell'}^{m} R_{\perp}^{-\ell'-2} A_{\ell' m}^{(1)} \mathcal{J}_{\ell\ell'}^{m(1)}(t_r,\xi_0) - \sum_{\ell'=1}^{M} \zeta_{\ell\ell'}^{m} R_{\perp}^{\ell'-1} B_{\ell' m}^{(3)} \mathcal{L}_{\ell\ell'}^{m(3)}(t_r,\xi_0) \\
&= E_0 \xi_0^{-1} \Bigg\{ \varepsilon_1 \sqrt{\frac{4\pi}{3}} \cos\theta_0 \left.\frac{\partial \widetilde{X}_1^0(\xi)}{\partial \xi}\right|_{\xi=\xi_0} \delta_{m0}\delta_{\ell 1} \\
&- \sqrt{\frac{2\pi}{3}} \sin\theta_0 e^{-i\phi_0} \left.\frac{\partial \widetilde{X}_1^1(\xi)}{\partial \xi}\right|_{\xi=\xi_0} \Big((\varepsilon_1 - \varepsilon_2) \zeta_{\ell 1}^{1} Q_{\ell 1}^{1}(-1,t_r) + \varepsilon_2 \delta_{\ell 1} \Big) \delta_{m1} \Bigg\} \\
&\forall\ \ell = 1,2,3,...,M; \quad m = 0,1.
\end{aligned} \tag{5.10}$$

With $S = 1$, the unknown constant terms $\psi_0^{(1)}$ and $\psi_0^{(3)}$ in the two regions above the substrate also need to be determined. Since we are only interested in potential differences, the first one may simply be set to zero, and the second one can now be calculated from Eq. (4.74):

$$\begin{aligned}
\psi_0^{(3)} &= R_\perp E_0 \cos\theta_0 \left(\frac{\varepsilon_1}{\varepsilon_2} - 1\right) \left\{ \frac{1}{\sqrt{3}} \zeta^0_{01} Q^0_{01}(-1, t_r) \right.\\
&\quad \left. + t_r \Big[1 - \zeta^0_{00} Q^0_{00}(-1, t_r) \Big] \right\}\\
&\quad - \frac{1}{2\sqrt{\pi}} \sum_{\ell'=1}^{M} A^{(1)}_{\ell' 0} R_\perp^{-\ell'-1} \zeta^0_{0\ell'} \xi_0^{\ell'+1} \left(\frac{\varepsilon_1 - \varepsilon_2}{\varepsilon_1 + \varepsilon_2}\right)\\
&\qquad \times \Big[\widetilde{Z}^0_{\ell'}(\xi_0) Q^0_{0\ell'}(-1, t_r) - (-1)^{\ell'} \widetilde{V}^0_{0\ell'}[\bar{\mu}, \xi_0](-1, t_r) \Big]\\
&\quad + \frac{1}{2\sqrt{\pi}} \sum_{\ell'=1}^{M} B^{(3)}_{\ell' 0} R_\perp^{\ell'} \zeta^0_{0\ell'} \xi_0^{-\ell'} \left(\frac{\varepsilon_3 - \varepsilon_4}{\varepsilon_3 + \varepsilon_4}\right)\\
&\qquad \times \Big[\widetilde{X}^0_{\ell'}(\xi_0) Q^0_{0\ell'}(-1, t_r) - (-1)^{\ell'} \widetilde{W}^0_{0\ell'}[\bar{\mu}, \xi_0](-1, t_r) \Big],
\end{aligned} \tag{5.11}$$

where the results from Eqs. (5.5) and (5.6) also have been used.

The results in Eqs. (5.9) – (5.11) agree with the expressions for uncoated, truncated prolate spheroidal particles found in [7], as they should.

5.2. The spherical limit

The case of truncated, coated spherical particles on a substrate has been solved in [15].

For a spheroid, the spherical limit is approached as

$$\begin{aligned}
\xi_0 &\to \infty\\
a &\to 0\\
a\xi_0 &= R
\end{aligned} \tag{5.12}$$

where R is the radius of the sphere. In this case, the prolate spheroidal coordinates can be written in terms of the ordinary spherical coordinates (r, θ, ϕ). We then get

$$\begin{aligned}
\xi &\simeq r/a\\
\eta &\simeq \cos\theta\\
\phi &= \phi
\end{aligned} \tag{5.13}$$

where a still is the focal radius of the spheroidal coordinate system.

It can be shown [7], as mentioned in section 4.2, that in the spherical limit the functions $\widetilde{X}^m_\ell(\xi, a)$ and $\widetilde{Z}^m_\ell(\xi, a)$ approach the radial part of a spherical solution, *i.e.* that

$$\begin{aligned}\widetilde{X}_\ell^m(\xi,a) &\simeq (\xi a)^\ell \simeq r^\ell \\ \widetilde{Z}_\ell^m(\xi,a) &\simeq (\xi a)^{-\ell-1} \simeq r^{-\ell-1}.\end{aligned} \tag{5.14}$$

The dimensionless versions of these functions defined in Eq. (4.38) thus have the following behaviour in the spherical limit

$$\begin{aligned}\widetilde{X}_\ell^m(\xi) &\simeq a^{-\ell} r^\ell \\ \widetilde{Z}_\ell^m(\xi) &\simeq a^{\ell+1} r^{-\ell-1}.\end{aligned} \tag{5.15}$$

Using these relations, it can be shown that the functions defined in Eqs. (4.59), (4.39) and (4.40) take the following form in the spherical limit

$$\begin{aligned}Q_{\ell\ell'}^m(\eta_1,\eta_2) &\simeq \int_{x_1}^{x_2} P_\ell^m(x) P_{\ell'}^m(x)\mathrm{d}x \\ \widetilde{V}_{\ell\ell'}^m\left[\kappa_z,\xi_{0,s}\right](\eta_1,\eta_2) &\simeq \xi_{0,s}^{-\ell'-1} I_{\ell\ell'}^m\left[\kappa_z,-\ell'-1,R_s\right](x_1,x_2) \\ \widetilde{W}_{\ell\ell'}^m\left[\kappa_z,\xi_{0,s}\right](\eta_1,\eta_2) &\simeq \xi_{0,s}^{\ell'} I_{\ell\ell'}^m\left[\kappa_z,\ell',R_s\right](x_1,x_2) \\ \frac{\partial}{\partial\xi}\left\{\widetilde{V}_{\ell\ell'}^m\left[\kappa_z,\xi\right](\eta_1,\eta_2)\right\}\bigg|_{r=R_s} &\simeq \xi_{0,s}^{-\ell'-2} J_{\ell\ell'}^m\left[\kappa_z,-\ell'-1,R_s\right](x_1,x_2) \\ \frac{\partial}{\partial\xi}\left\{\widetilde{W}_{\ell\ell'}^m\left[\kappa_z,\xi\right](\eta_1,\eta_2)\right\}\bigg|_{r=R_s} &\simeq \xi_{0,s}^{\ell'-1} J_{\ell\ell'}^m\left[\kappa_z,\ell',R_s\right](x_1,x_2),\end{aligned} \tag{5.16}$$

where the integrals $I_{\ell\ell'}^m$ and $J_{\ell\ell'}^m$ are defined as

$$I_{\ell\ell'}^m\left[\kappa_z,\alpha,R_s\right](x_1,x_2) = \int_{x_1}^{x_2} P_\ell^m(x)\left(\frac{r_\kappa}{R_s}\right)^\alpha P_{\ell'}^m(x_\kappa)\mathrm{d}x, \tag{5.17}$$

and

$$J_{\ell\ell'}^m\left[\kappa_z,\alpha,R_s\right](x_1,x_2) = R_s\int_{x_1}^{x_2} P_\ell^m(x)\frac{\partial}{\partial r}\left[\left(\frac{r_\kappa}{R_s}\right)^\alpha P_{\ell'}^m(x_\kappa)\right]\bigg|_{r=R_s}\mathrm{d}x. \tag{5.18}$$

Here $x = \cos\theta \simeq \eta$ and $x_\kappa = \cos\theta_\kappa \simeq \eta_\kappa(\xi,\eta)$. As before, the subscript κ is a placeholder for one of the expansion points μ or $\bar{\mu}$, and indicates that a coordinate belongs to the coordinate system with origin in this point. Similarly $r_\kappa = r_\kappa(r,\theta)$ is the distance from expansion point κ to a point (r,θ,ϕ).

Using the relations in Eq. (5.16), the abbreviations introduced in section 4.7 can now be written as

$$\begin{aligned}\mathcal{I}_{\ell\ell'}^{m(i)}(t_r,\xi_0) \simeq \Big[& I_{\ell\ell'}^m\left[\mu,-\ell'-1,R_s\right](-1,t_r) \\ & + (-1)^{\ell'+m'}\mathcal{R}_i I_{\ell\ell'}^m\left[\bar{\mu},-\ell'-1,R_s\right](-1,t_r) \\ & + \mathcal{T}_i I_{\ell\ell'}^m\left[\mu,-\ell'-1,R_s\right](t_r,1)\Big],\end{aligned} \tag{5.19}$$

$$\begin{aligned}\mathcal{K}^{m(i)}_{\ell\ell'}(t_r,\xi_0) \simeq \Big[& I^m_{\ell\ell'}\left[\mu,\ell',R_s\right](-1,t_r) \\ & + (-1)^{\ell'+m'}\mathcal{R}_i I^m_{\ell\ell'}\left[\bar{\mu},\ell',R_s\right](-1,t_r) \\ & + \mathcal{T}_i I^m_{\ell\ell'}\left[\mu,\ell',R_s\right](t_r,1)\Big],\end{aligned} \tag{5.20}$$

$$\begin{aligned}\mathcal{J}^{m(i)}_{\ell\ell'}(t_r,\xi_0) \simeq \xi_0^{-1}\Big[& \varepsilon_i J^m_{\ell\ell'}\left[\mu,-\ell'-1,R_s\right](-1,t_r) \\ & + (-1)^{\ell'+m'}\varepsilon_i\mathcal{R}_i J^m_{\ell\ell'}\left[\bar{\mu},-\ell'-1,R_s\right](-1,t_r) \\ & + \varepsilon_{i+1}\mathcal{T}_i J^m_{\ell\ell'}\left[\mu,-\ell'-1,R_s\right](t_r,1)\Big],\end{aligned} \tag{5.21}$$

$$\begin{aligned}\mathcal{L}^{m(i)}_{\ell\ell'}(t_r,\xi_0) \simeq \xi_0^{-1}\Big[& \varepsilon_i J^m_{\ell\ell'}\left[\mu,\ell',R_s\right](-1,t_r) \\ & + (-1)^{\ell'+m'}\varepsilon_i\mathcal{R}_i J^m_{\ell\ell'}\left[\bar{\mu},\ell',R_s\right](-1,t_r) \\ & + \varepsilon_{i+1}\mathcal{T}_i J^m_{\ell\ell'}\left[\mu,\ell',R_s\right](t_r,1)\Big].\end{aligned} \tag{5.22}$$

By inserting the results in Eqs. (5.19) – (5.22) into the left hand sides of the linear set of equations given by Eqs. (4.72) and (4.73), these are found to be equal to the left hand sides of the linear set of equations previously calculated for the case of truncated, coated spherical particles in [15].

The right hand sides of Eqs. (4.72) and (4.73), which have their origin in the incident and transmitted fields, are shown in [7] to tend to the equivalent expressions in spherical coordinates in the spherical limit. Similarly, it is shown in [7] that, in the spherical limit, the expression for the constant potential terms in Eq. (4.74) tend to the equivalent expressions in the spherical case. It can therefore be concluded that the expressions derived here for truncated, coated prolate spheroidal particles are equivalent, in the spherical limit, to those previously derived for truncated, coated spherical particles, as they should.

Although the equations found here for the prolate spheroidal case can be seen as a generalization of the spherical case, since the latter is a limit of the former, both cases are still needed, since it in practice is impossible to reach the limit $\xi_0 \to \infty,\ a \to 0,\ a\xi_0 \to R$ numerically.

6. Numerical modelling

In the two previous chapters, the linear set of equations for the multipole expansion coefficients for the prolate spheroidal system was derived and analytically shown to be equivalent to previously calculated cases in certain limits. The next step is now to solve the system of equations numerically. The implementation and testing of this calculation is covered in this chapter. Section 6.1 covers some details around the implementation, while section 6.2 contains the results of the numerical tests used to verify its correctness.

6.1. Implementation

The equations derived in chapter 4 were implemented in the existing GranFilm 2.0 framework. This software, which is written in the *Fortran 90* programming language, already supported films of coated spheres and oblate spheroids, but not prolate spheroids.

The implementation consisted of adding prolate spheroid support to several parts of the GranFilm code. In Figure 6.1 an overview of the structure of the software can be seen, including the parts of the code that were modified and added. The program starts by calculating all the necessary integrals, as given in Eqs. (4.41)–(4.42) and (4.48)–(4.49), up to a multipole order M. The integrands of these integrals are dependent on the island geometry, so a new module containing these integrands was implemented for the prolate spheroidal case. The integrands, in turn, required a new set of Legendre polynomials and coordinate transformations to be implemented. This is discussed in more detail in App. B.

When the integrals have been calculated, the system of equations for the multipole expansion coefficients in Eqs. (4.72)–(4.73) is set up and solved for a range of photon energies. Although there is no explicit energy dependence in the linear set of equations, the system is dependent on the photon energy through the dielectric functions $\varepsilon_i(\omega)$ of the different media. It should be noted that the system of equations is implemented in a slightly

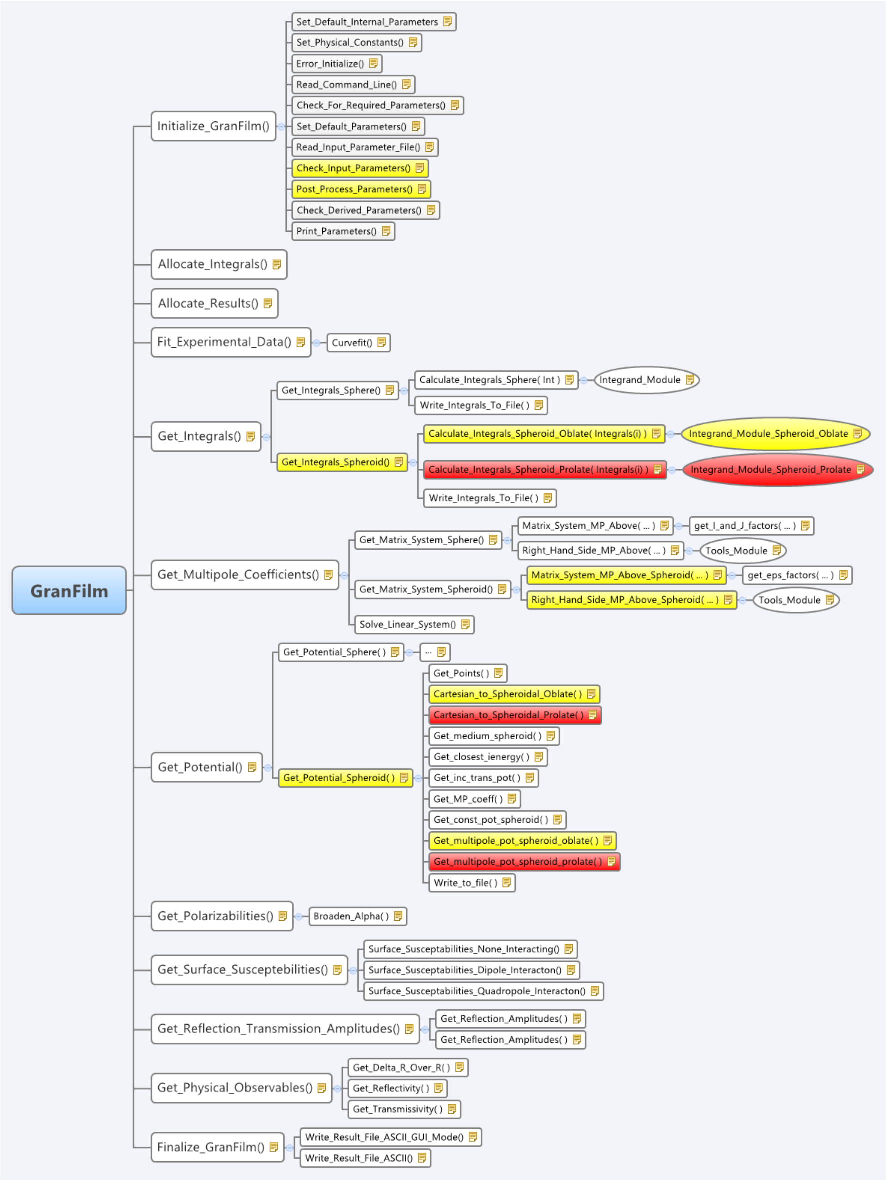

Figure 6.1: Overview of the main routines and modules of GranFilm. The program is run depth-first starting on the top branch. The boxes marked red are the new routines added in the implementation of prolate spheroid support, while the yellow boxes are existing routines that needed modification in order to support prolate spheroids.

different form than in Eqs. (4.72)–(4.73) in order for the coefficients to be dimensionless. This is detailed in Appendix A.

After solving the system of equations, one is left with a set of normalized expansion coefficients $\widehat{A}_{\ell m}^{(i)}$ and $\widehat{B}_{\ell m}^{(i)}$ for each photon energy. The first few coefficients are then used to calculate the island polarizability, which in turn is used to find the first order surface susceptibilities γ and β as discussed in section 4.10. These are finally used in calculating the amplitudes of transmission and reflection in Eqs. (2.20)–(2.23).

Once the expansion coefficients are known, the potential in any region in and around an island may also be calculated explicitly for a given photon energy, using Eqs. (4.32)–(4.33). This calculation is performed in a separate module, which was also modified to support prolate spheroidal islands. The details of this implementation can be found in Appendix C. Using this module, the potential in the near-field may be studied at any set of points specified by the user. This makes it possible to *e.g.* inspect the potential in a cross-section of an island, or controlling the boundary conditions by evaluating the potential at points on both sides of an interface.

6.2. Numerical tests

In order to check whether the equations implemented are correct, a number of numerical tests are performed and summarized below. First, the differential reflectance (SDRS) curves, which is the main output of GranFilm, are inspected for island films of different geometries in the spherical limit. Second, the potential around islands of different geometries, also in the spherical limit, is evaluated and compared visually. These two tests provides evidence of the success of the implementation, but are no proof of correctness. The ultimate test of the correctness of the implementation is the third one, which is to quantitatively inspect the fulfilment of the boundary conditions, Eq. (4.4), on the spheroidal interfaces.

The parameters of the main test case studied in this section are specified in Table 6.1. This describes a film of truncated prolate spheroidal silver particles, supported by a substrate of $\mathrm{Al_2O_3}$. The islands are coated by silver oxide ($\mathrm{Ag_2O}$). The number of multipoles used in the calculations is $M = 16$. The islands are arranged in a hexagonal lattice with lattice constant $L = 20$ nm and the incident field is p-polarized[1] with incident angles $\theta_0 = 45°$ and $\phi_0 = 0°$. If not otherwise specified, the same lattice

---

[1] Remember that this polarization gives excitations both in the parallel and normal directions, as mentioned in section 2.2.3

configuration and incident radiation are used for all test cases throughout this chapter.

Parameter set 1		
Substrate medium		Al_2O_3
Core medium		Ag
Coating medium		Ag_2O
Radii	$R_\perp$	8.0 nm
	$R_\parallel$	7.0 nm
Core radius ratio	χ_2	0.9
Truncation ratio	t_r	0.25
Multipole order	M	16

Table 6.1: Main test parameters used in the GranFilm runs of this section.

6.2.1. SDR spectra in the spherical limit

In chapter 5, the linear set of equations for the potential expansion coefficients of a prolate spheroidal island was shown to be equal to the equivalent set of equations for a spherical island, in the limit where the prolate spheroid becomes spherical. One would therefore expect that the observable properties of a film of prolate spheroidal islands are equal to those of a film of spherical islands in this limit. This must also be true in the numerical simulation, and it is therefore useful to first check that this holds for the new implementation.

With the addition of prolate spheroid support in GranFilm, the software now supports islands of three different geometry types; prolate spheroids, spheres and oblate spheroids. Each of these geometries has its own more or less independent parts of the code, so that when calculating the potential expansion coefficients, different parts of the code are invoked for different geometries. A reasonable test of the new code is therefore to run the program for each of the three geometries in the limit where they become equal, *i.e.* in the spherical limit. For spheroids where $R_\perp$ and $R_\parallel$ are only slightly different, one would expect that the calculated SDRS spectrum is similar to that of a sphere with the same radius.

Uncoated islands

In order to check that the output of the new implementation of GranFilm is consistent in the spherical limit, two sets of test runs are first performed for the case of uncoated islands. The parameters used in these runs are the ones specified in Parameter set 1 in Table 6.1, but with the coating removed. This essentially means that the radius ratio of the core, χ_2, is set to 1.0. In addition the this, the island radii are varied, in order for all three geometry branches of the GranFilm program to be invoked. The radii in the two sets of runs are as follows:

1. The radius parallel to the substrate, $R_{\|}$, is kept constant at 7.7 nm, while the normal radius $R_{\perp}$ is varied in the range $7.1-8.3$ nm. This changes the shape of the islands from oblate spheroidal to prolate spheroidal, via spherical.

2. The normal radius $R_{\perp}$ is kept constant at 7.7 nm, while $R_{\|}$ is varied in the range $7.1 - 8.3$ nm. This changes the shape of the islands from prolate spheroidal to oblate spheroidal, via spherical.

The resulting SDRS curves of these two sets of runs are presented in Figures 6.2 and 6.3, respectively.

As can be seen from Figures 6.2 –6.3, the curves for the spheroidal geometries lie symmetrically around the curve corresponding to the spherical islands. As both the prolate and oblate spheroidal particles become more spherical, their SDRS curves move closer to the central spherical curve. The same behaviour is also observed around the resonance peaks. This indicates that the differential reflectance spectrum of a film of spheroidal islands converges towards the spectrum of a film of spherical islands in the spherical limit, as it should.

Note from Figure 6.3 that the height of the main resonance peak, located around 2.7 eV is very sensitive to variations in $R_{\|}$. This suggests that the excitations parallel to the substrate are mainly responsible for this resonance, since the resonance peak grows as as $R_{\|}$ increases[2]. This could also be explained by noting that when $R_{\|}$ increases, the metal coverage of the substrate increases, resulting in a higher reflectance. In Figure 6.2, $R_{\|}$ is kept constant, which means that the fraction of the substrate covered by metal is constant, since only the height of the islands is changed. Note from Figure 6.4b that the film of oblate spheroids still gives the highest resonance, although the prolate spheroids have a bigger volume. This could be explained by the fact that when the height of the island increases, its center of mass moves away from the substrate. This leads to a weaker interaction between the island and the substrate, with a weaker resonance as a result.

---

[2] This is also discussed in chapter 7.

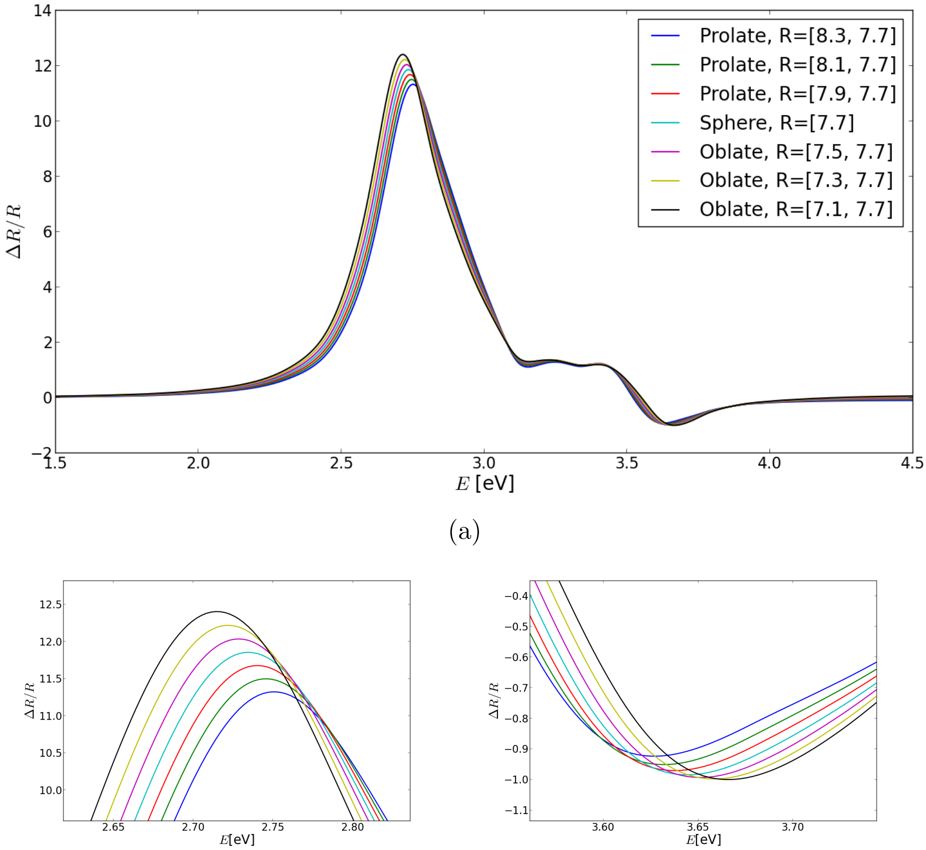

(a)

(b)

(c)

Figure 6.2: (a) Comparison of the SDRS curves for various uncoated particle geometries in the spherical limit, with $R_{||}$ kept constant. The spheroidal curves approach the spherical curve as the particles approach a spherical geometry. (b) Close-up view of the main resonance peak located around 2.7 eV. (c) Close-up view of the resonance peak located around 3.6 eV

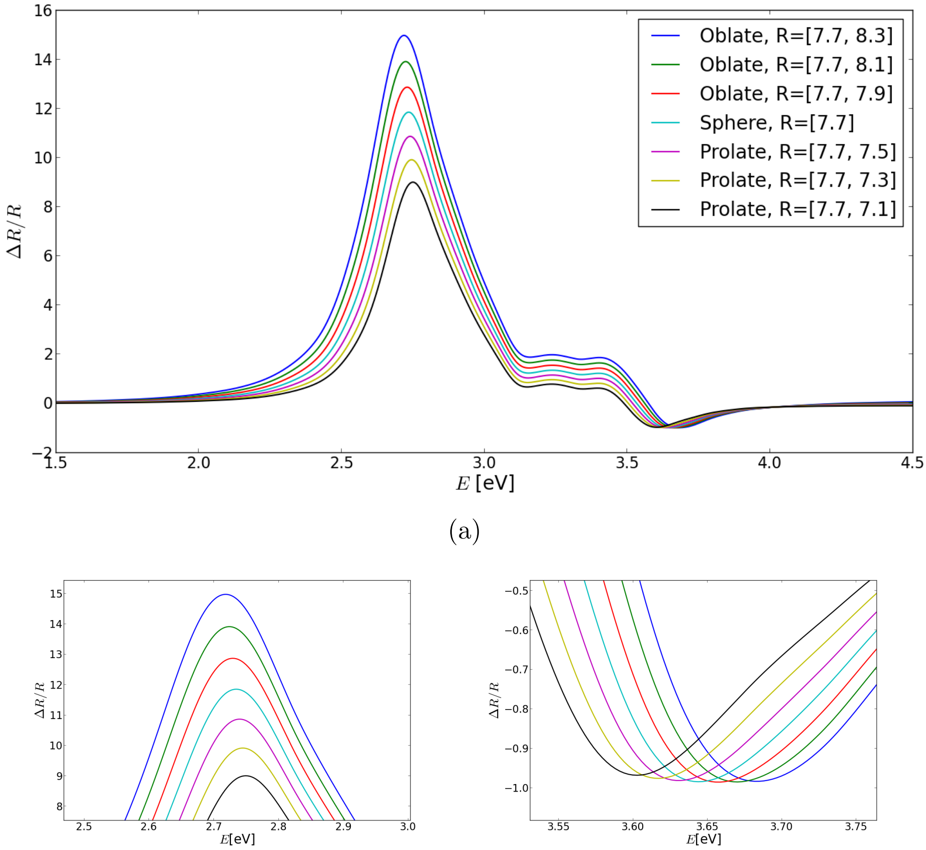

(a)

(b)

(c)

Figure 6.3: (a) Comparison of the SDRS curves for various <u>uncoated</u> particle geometries in the spherical limit, with $R_\perp$ kept constant. The spheroidal curves approach the spherical curve as the particles approach a spherical geometry. (b) Close-up view of the resonance peak located around 2.7 eV. (c) Close-up view of the resonance peak located around 3.6 eV.

Coated islands

The same two sets of runs as in the previous paragraph are then performed on an island film where a thin layer of coating has been applied to the silver islands, as specified in Parameter set 1 in Table 6.1. The coating consists of silver oxide in order to simulate oxidation of the islands, and has a thickness such that the radius ratio of the silver core is $\chi_2 = 0.9$. The resulting SDRS curves of the two sets of runs are presented in Figures 6.4 and 6.5.

Figures 6.4–6.5 show that the SDRS curves in the spheroidal cases again lie symmetrically around the curve corresponding to the spherical geometry. The spheroidal SDR spectra move closer to the spherical one, as the spheroids become more sphere-like. This indicates that the differential reflectance spectra of the spheroidal island films in the spherical limit approach the spectrum of the spherical island film, in the coated case as well.

By comparing the figures in the coated case (6.4–6.5) with the corresponding figures in the uncoated case (6.2–6.3), it is observed that the introduction of a coating on the islands has the effect of shifting the main resonance peak towards a lower energy. This effect seems to be greater for prolate spheroids than for oblate spheroids, as *e.g.* seen when comparing Figures 6.2b and 6.4b.

6.2.2. Visual inspection of the potential

In the limit where the spheroidal islands become spherical, the potential in a region around the islands should also approach the same values. By studying the potential in a cross-section of an island in this limit visually, possible errors in the implementation could be detected.

For this test, three runs of GranFilm are performed, one for each geometry type. The parameters defined in Parameter set 1 in Table 6.1 are used in all three runs, but with different island radii. The radii are $R_\perp = 8.0$ nm, $R_\parallel = 7.0$ nm in the prolate spheroidal run, $R_\perp = 7.0$ nm, $R_\parallel = 8.0$ nm in the oblate spheroidal run and $R = 7.5$ nm in the spherical run. The potential around one island in the xz-plane is evaluated at an energy close to the main resonance peak ($E = 2.4$ eV) and a contour plot of the real part of the potential is made for all three runs. The resulting potentials can be seen in Figures 6.6a–6.6c.

As can be seen from these figures, the potential seems to behave consistently for all three geometry types. The same parallel dipole excitation is observed for all three cases, but with a lower amplitude for the prolate

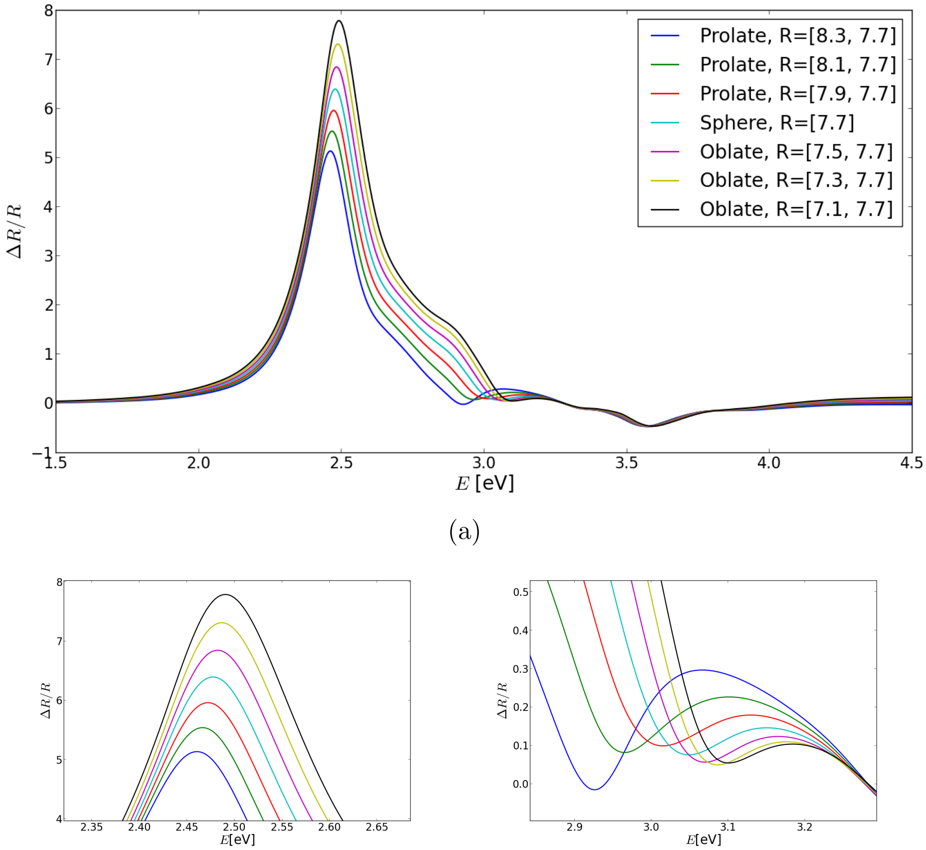

(a)

(b)

(c)

Figure 6.4: (a) Comparison of the SDRS curves for various coated particle geometries in the spherical limit, with $R_{\|}$ kept constant. The spheroidal curves approach the spherical curve as the particles approach a spherical geometry. (b) Close-up view of the main resonance peak located around 2.5 eV. (c) Close-up view of the behaviour around 3.0 eV.

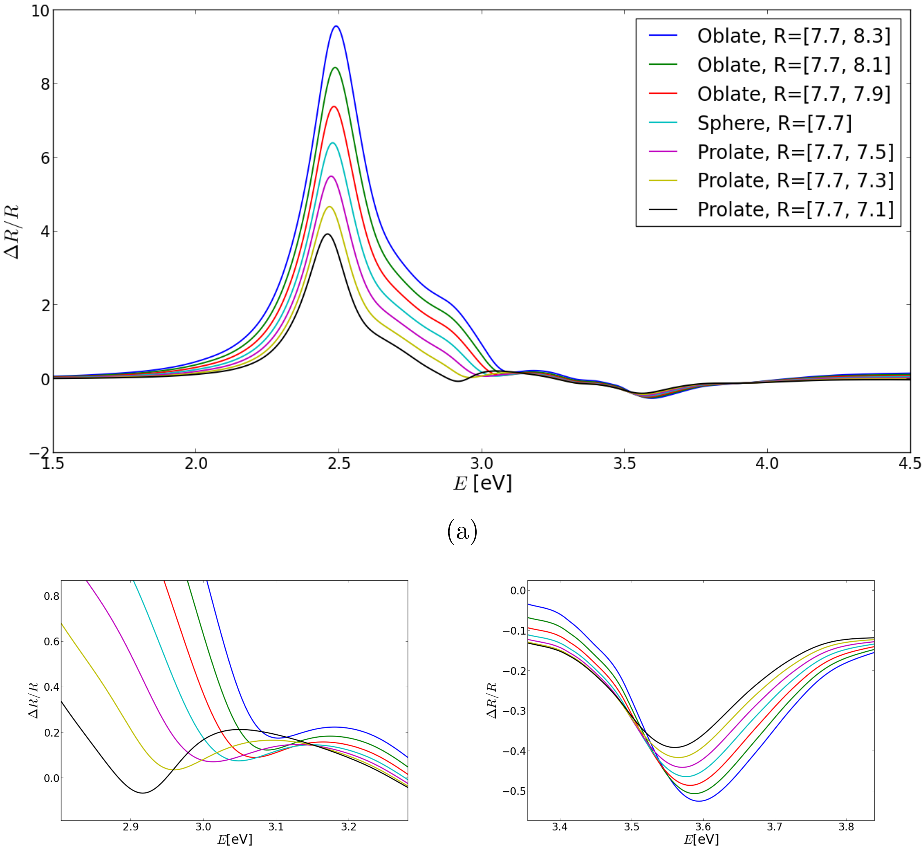

(a)

(b) (c)

Figure 6.5: (a) Comparison of the SDRS curves for various coated particle geometries in the spherical limit, with $R_\perp$ kept constant. The spheroidal curves approach the spherical curve as the particles approach a spherical geometry. (b) Close-up view of the behaviour around 3 eV. (c) Close-up view of the resonance peak located around 3.6 eV

spheroidal case in Fig. 6.6a. This is consistent with the results seen in the previous section, where the prolate spheroids had the weakest resonance peaks in the SDRS curves.

6.2.3. Fulfilment of boundary conditions

The uniqueness theorem guarantees that if a potential satisfies the Laplace equation and the boundary conditions of the system, the solution is the one and only correct one. By construction, the equations (4.72)–(4.73) implemented in GranFilm satisfies the Laplace equation (4.3) and also the boundary conditions (4.4) at the $z = d$ interfaces. The boundary conditions at the spheroidal interfaces are, on the other hand, only indirectly enforced through their weak form. The error in the boundary conditions at the spheroidal interfaces is therefore a measure of the correctness of the implementation, and needs to be checked numerically.

The boundary conditions, Eqs. (4.4a)–(4.4b), states that the potential, ψ, and the normal derivative of the potential times the permittivity, $\varepsilon\partial_n\psi$, must be continuous over all interfaces between two media. In order to evaluate the errors in these boundary conditions, a set of dimensionless error measures, similar to those used in [16], are introduced. These are, for the first (4.4a) and second (4.4b) boundary conditions, respectively

$$e_1(\mathbf{r_s}) = \frac{\psi_+(\mathbf{r_s}) - \psi_-(\mathbf{r_s})}{\max_{\mathbf{r_1}}|\psi_{\text{inc}}(\mathbf{r_1})|} \tag{6.1}$$

$$e_2(\mathbf{r_s}) = \frac{\varepsilon_+\partial_n\psi_+(\mathbf{r_s}) - \varepsilon_-\partial_n\psi_-(\mathbf{r_s})}{\max_{\mathbf{r_1}}|\varepsilon_1\partial_n\psi_{\text{inc}}(\mathbf{r_1})|} \tag{6.2}$$

where $\mathbf{r_s}$ is a point on the spheroidal interface s, *i.e.* where $\xi = \xi_{0,s}$, and the subscripts $+, -$ indicates that a quantity is evaluated just outside or inside the spheroidal interface, respectively. The first error measure, e_1, is normalized by the maximum value of the incident potential $\psi_{\text{inc}}(\mathbf{r_1})$, evaluated at the outermost interface. The second error measure, e_2, is normalized by the maximum value of the normal derivative of the incident potential times the permittivity, $\varepsilon_1\partial_n\psi_{\text{inc}}(\mathbf{r_1})$, evaluated just outside the outermost interface. Here $\mathbf{r_1}$ is a point on the outermost interface. These normalizations make both error measures dimensionless and independent of the incident field strength E_0.

The error in the first boundary condition, e_1, is found by calculating the potential at points just inside and just outside of the interface. The error in the second boundary condition, e_2, is calculated in the same way, but now using two points just inside and two points just outside of the

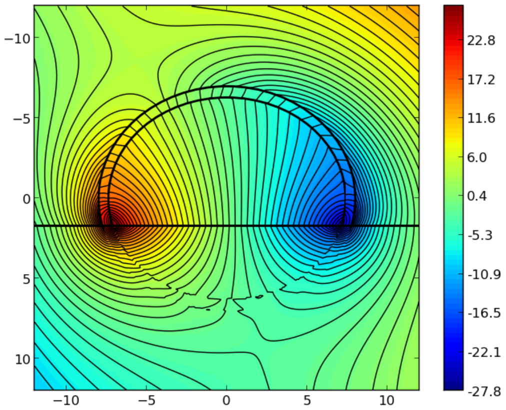

(a) Oblate, $R_\perp = 7.0$ nm, $R_\parallel = 8.0$ nm

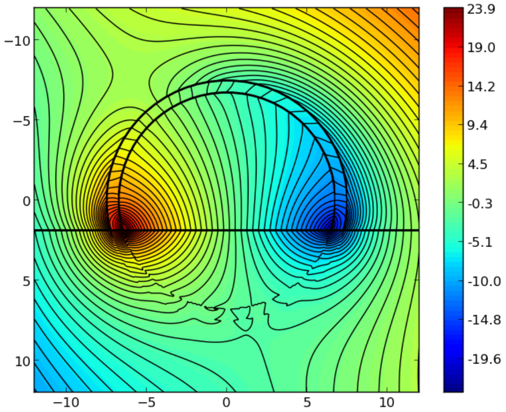

(b) Spherical, $R = 7.5$ nm

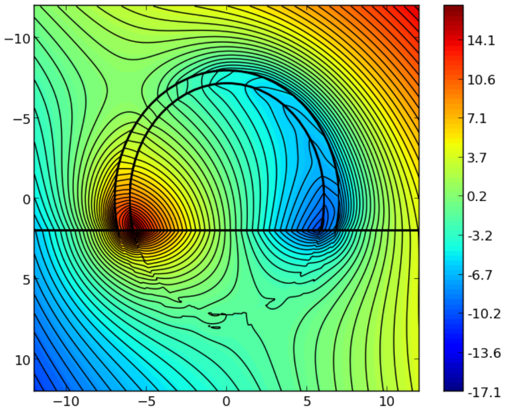

(c) Prolate, $R_\perp = 8.0$ nm, $R_\parallel = 7.0$ nm

Figure 6.6: Potential maps in the xz-plane for the three geometries at $E = 2.4\,\text{eV}$.

interface, allowing for the calculation of the normal derivative of the potential using a finite-difference approach. The prolate spheroidal metric tensor, defined in section 3.2, is used to find these points on a line normal to the interface. It should be noted that the normal derivative of the potential was also calculated analytically using the expansion coefficients. This is discussed in more detail in section 6.2.4. For this specific test case, however, this was not deemed necessary as the finite-difference approach was well-behaved.

In order to study the errors in the boundary conditions along the spheroidal interfaces, the quantities ψ, $\varepsilon\partial_n\psi$, e_1 and e_2 are calculated in the xz-plane at points evenly spaced in $\arccos(\eta)$. The simulation parameters are the ones defined in Parameter set 1 in Table 6.1. The potential is evaluated at an energy close to the main resonance peak of the SDRS curve ($E = 2.4$ eV), since the highest error can be expected here.

The results of these tests can be seen in Figs. 6.7–6.10. The errors in the boundary conditions found here are well within what could be expected when taking into account the fact that the boundary conditions are only indirectly enforced on the system through their weak form, as explained in section 4.7. Note that the error is biggest close to the substrate interface. This is also as expected, since the potential here has to fulfil the boundary conditions at the spheroidal and substrate interfaces simultaneously.

6.2.4. Analytic normal derivatives

As mentioned in the previous section, the numerical tests of the boundary conditions were well-behaved for the test case in question. However, when studying island films with higher truncation ratios, *i.e.* where the islands are only slightly truncated by the substrate[3], some anomalous results appeared in the boundary condition tests. In Figures 6.11–6.12, the second boundary condition is again checked on the system defined in Parameter set 1 in Table 6.1, but now with a truncation ratio of $t_r = 0.75$.

From these figures it appears that the second boundary condition is not at all satisfied in this case. From the behaviour of these errors it seems likely that numerical errors become significant in the limit of high truncation ratios. It is also observed that the error increases with higher truncation ratio t_r and multipole order M. Furthermore, it is clear from the figures that the error is dependent on the polar angle (θ, η), since it grows out of proportion close to the top of the island. Note from Figure 6.11 that the calculation of the second boundary condition only breaks

---

[3] see section 3.3 for the definition of truncation ratio

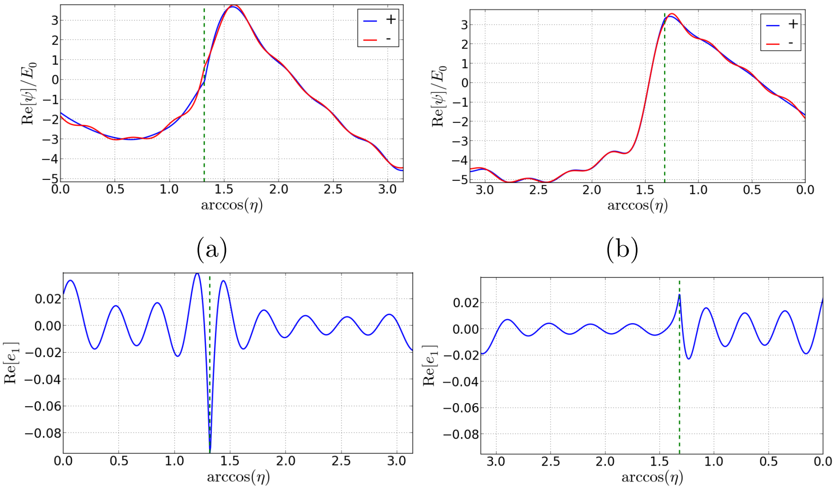

(a) (b)

(c) (d)

Figure 6.7: Real part of the potential ψ just outside $(+)$ and inside $(-)$ the outermost spheroidal interface $s = 1$, evaluated at the (a) $\phi = 0$ half and (b) $\phi = \pi$ half of the xz-plane at the energy $E = 2.4$ eV. (c) and (d) shows the real part of the error e_1 evaluated at the same points. The vertical dashed line indicates where the island is truncated by the substrate.

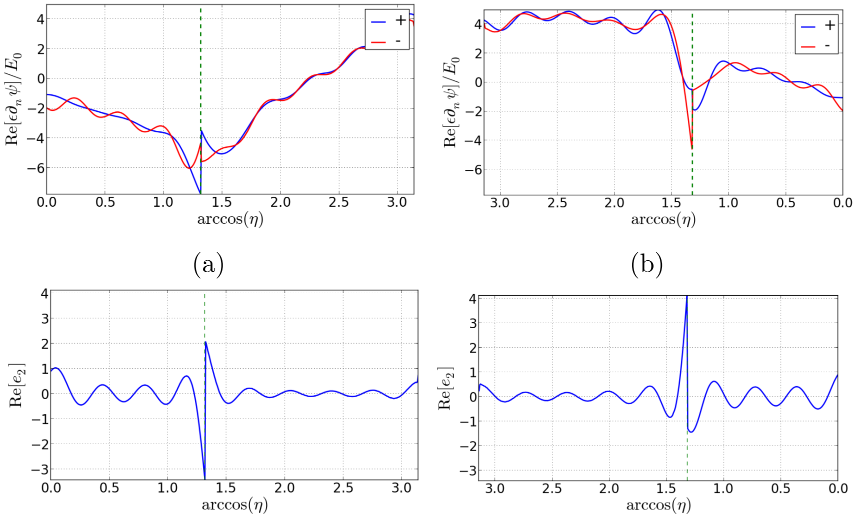

(a) (b)

(c) (d)

Figure 6.8: Real part of the normal derivative of the potential times the permittivity $\varepsilon\partial_n\psi$ just outside $(+)$ and inside $(-)$ the outermost spheroidal interface $s = 1$, evaluated at the (a) $\phi = 0$ half and (b) $\phi = \pi$ half of the xz-plane at the energy $E = 2.4$ eV. (c) and (d) shows the real part of the error e_2 evaluated at the same points. The vertical dashed line indicates where the island is truncated by the substrate.

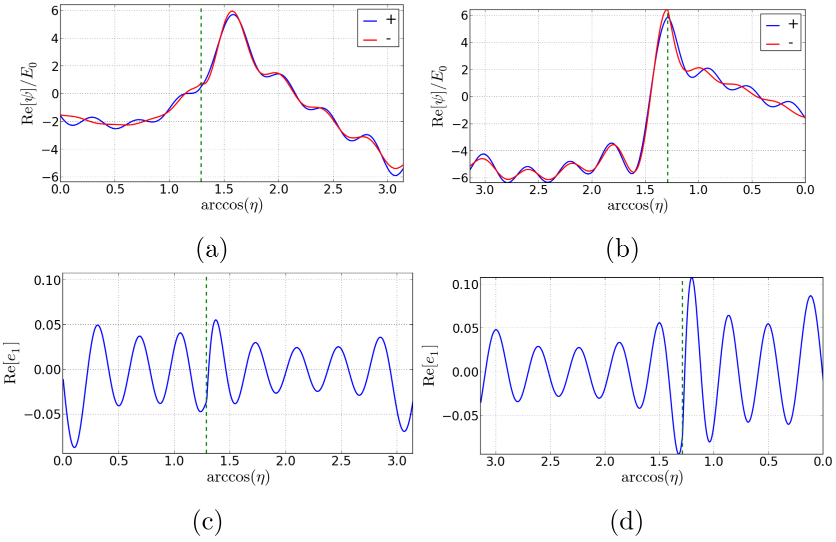

(a) (b)

(c) (d)

Figure 6.9: Real part of the potential ψ just outside (+) and inside (−) the inner spheroidal interface $s = 2$, evaluated at the (a) $\phi = 0$ half and (b) $\phi = \pi$ half of the xz-plane at the energy $E = 2.4$ eV. (c) and (d) shows the real part of the error e_1 evaluated at the same points. The vertical dashed line indicates where the island is truncated by the substrate.

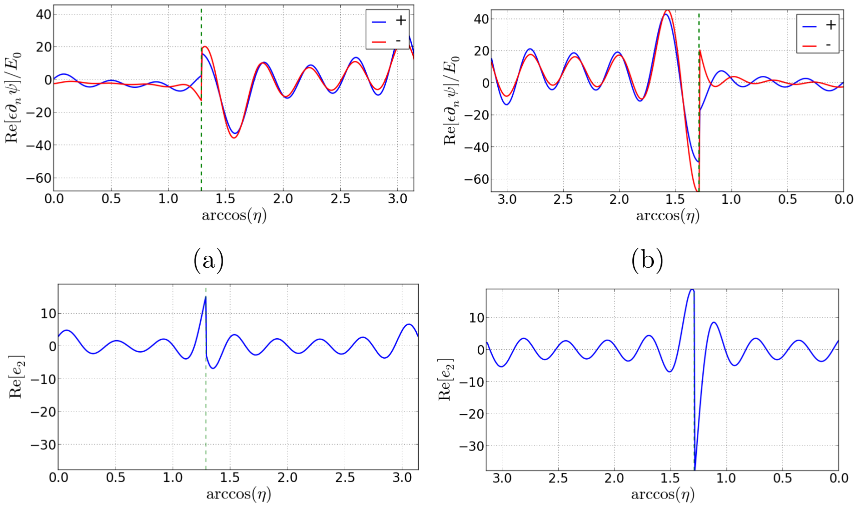

(a) (b)

(c) (d)

Figure 6.10: Real part of the normal derivative of the potential times the permittivity $\varepsilon\partial_n\psi$ just outside (+) and inside (−) the inner spheroidal interface $s = 2$, evaluated at the (a) $\phi = 0$ half and (b) $\phi = \pi$ half of the xz-plane at the energy $E = 2.4$ eV. (c) and (d) shows the real part of the error e_2 evaluated at the same points. The vertical dashed line indicates where the island is truncated by the substrate.

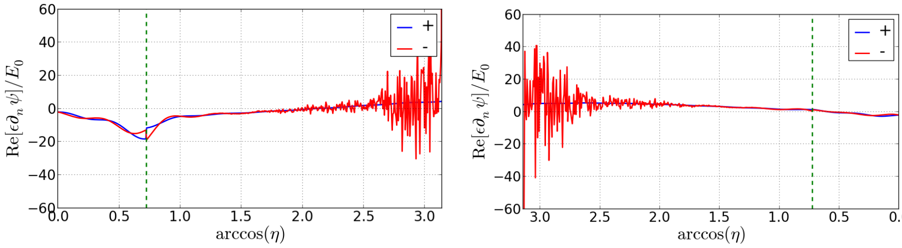

(a) (b)

Figure 6.11: Real part of the finite-difference normal derivative times the permittivity just outside (+) and inside (−) the outermost spheroidal interface $s = 1$ at the energy $E = 2.4$ eV for a high truncation ratio of $t_r = 0.75$. The figures show $\varepsilon\partial_n\psi$ evaluated at the (a) $\phi = 0$ half and (b) $\phi = \pi$ half of the xz plane. Note that $\varepsilon\partial_n\psi$ seems to behave normally outside the interface.

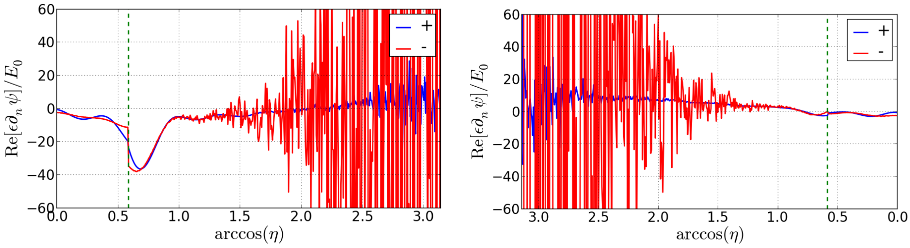

(a) (b)

Figure 6.12: Real part of the finite-difference normal derivative times the permittivity just outside (+) and inside (−) the inner spheroidal interface $s = 2$ at the energy $E = 2.4$ eV for a high truncation ratio of $t_r = 0.75$. The figures show $\varepsilon\partial_n\psi$ evaluated at the (a) $\phi = 0$ half and (b) $\phi = \pi$ half of the xz plane.

down in the interior of the island, and seems to be correct for the region outside the island.

It seems likely that the origin of this error lies in the *python* script used for calculating the normal derivatives of the potential using a finite-difference approach. In order to make sure that these errors in fact were due to this approximation, and rule out any problems with the GRANFILM code itself, an analytical calculation of the normal derivatives was carried out.

The calculation of the analytic normal derivatives of the potential was implemented in a new module in GRANFILM. The normal derivatives are found by differentiating Eqs. (4.32)–(4.33) with respect to ξ and evaluating this on both sides of the spheroidal interfaces using the multipole coefficients. The details of this calculation can be found in Appendix C.2. As can be seen in Figs. 6.13–6.13, this evaluation yields a much better result, and the second boundary condition turns out to be reasonably well satisfied in the case of a high truncation ratio as well.

6.2.5. Dependence on the multipole order *M*

In theory, an infinite number of multipoles are required in order to solve the system of equations in Eqs. (4.72)–(4.73). In practice, however, the number of multipoles must be limited when calculating the potential numerically in order to be able to run the simulations in a reasonable amount of time. By varying the number of multipoles included in the simulations, the convergence properties of the new parts of the code can be studied.

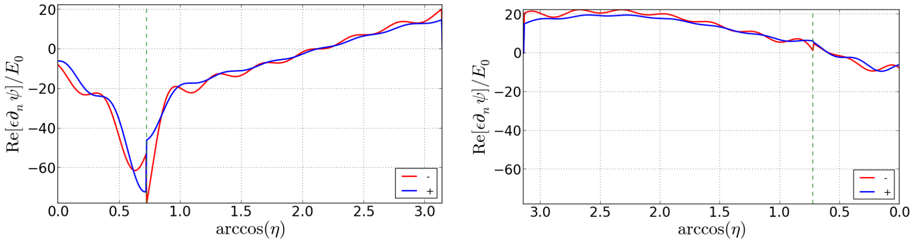

(a) (b)

Figure 6.13: Real part of the analytic normal derivative times the permittivity just outside (+) and inside (−) the outermost spheroidal interface $s = 1$ at the energy $E = 2.4$ eV for a high truncation ratio of $t_r = 0.75$. The figures show $\varepsilon\partial_n\psi$ evaluated at the (a) $\phi = 0$ half and (b) $\phi = \pi$ half of the xz plane.

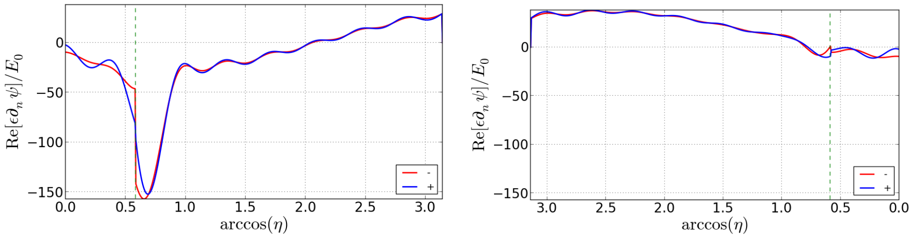

(a) (b)

Figure 6.14: Real part of the analytic normal derivative times the permittivity just outside (+) and inside (−) the inner spheroidal interface $s = 2$ at the energy $E = 2.4$ eV for a high truncation ratio of $t_r = 0.75$. The figures show $\varepsilon\partial_n\psi$ evaluated at the (a) $\phi = 0$ half and (b) $\phi = \pi$ half of the xz plane.

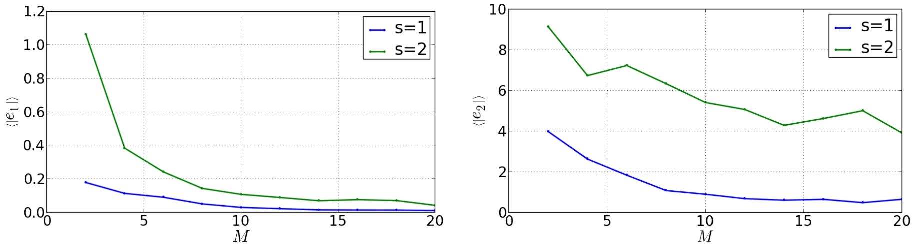

(a) (b)

Figure 6.15: Average error in the first (a) and second (b) boundary condition at $E = 2.7$ eV, as a function of multipole order. Note that the error at the outer interface ($s = 1$) is greater than the error at the inner interface ($s = 2$).

Convergence of boundary conditions

As discussed in section 6.2.3, the error in the boundary conditions on the spheroidal interfaces can be seen as a measure of the correctness of the implementation. One should therefore expect that a higher multipole order gives a better fulfilment of these boundary conditions.

In Figures 6.15–6.16 the average error in both boundary conditions at the two spheroidal interfaces of the test system in the previous section is plotted for various multipole orders. This is done at the two energies $E = 2.7$ eV and $E = 4.5$ eV, where first energy is close to the main resonance peak, while the second is far from any resonances. As indicated by these figures, the average error decreases with increasing multipole order, as it should. Note that the average errors at the energy close to the resonance peak in Fig. 6.15 are around one order of magnitude greater than the average errors at the energy far from the resonance in Fig. 6.16. This is not unreasonable, since the potential exhibits a more dramatic behaviour close to the resonances. A greater error can therefore be expected here.

From this one could be led to believe that a higher multipole order is always better. Although this is true up to a certain point, it turns out that if one includes multipoles of too high orders the average error starts increasing again. This is probably due to numerical round-off errors in the calculations. These errors were observed to start dominating around $M = 25$ in some cases.

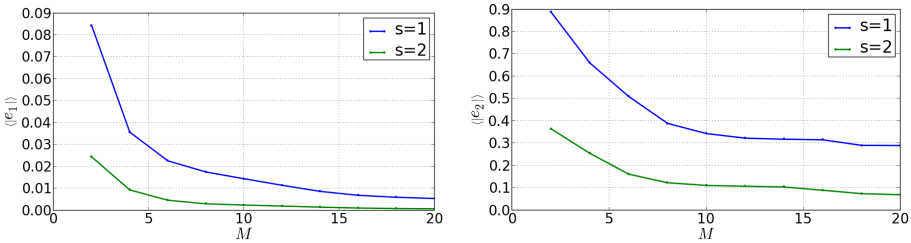

(a) (b)

Figure 6.16: Average error in the first (a) and second (b) boundary condition at $E = 4.5$ eV, as a function of multipole order. Note that the error at the outer interface ($s = 1$) is greater than the error at the inner interface ($s = 2$).

Convergence of SDRS curves

With an increasing number of multipoles included in the calculation, one also expects that the observable differential reflectance spectrum of the island film converges towards a 'true' spectrum. The results of this test is in Figure 6.17.

Here the resulting SDRS curves of several runs of the test case defined in Parameter set 1 in Table 6.1, but with different multipole orders M, are compared. It is quite clear that the SDRS curves converges towards a single curve with an increasing number of multipoles. By subtracting the curve corresponding to $M = 24$ from the others, this tendency is even clearer. This is presented in Figure 6.18.

It should be noted from Figure 6.17c that the 'shoulder' on the SDRS curve around 2.7 eV is not visible for $M < 12$. This indicates that multipoles of this order are needed in order to capture some of the effects of the SDRS curves.

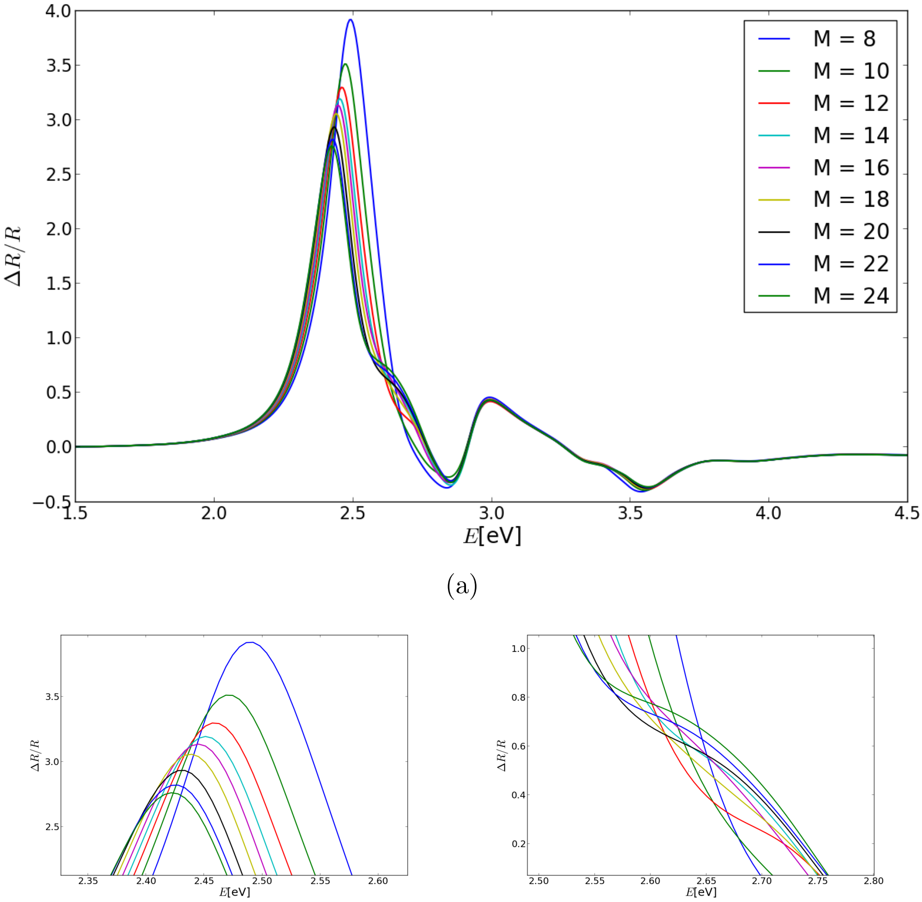

(a)

(b) (c)

Figure 6.17: (a) Comparison of the SDRS curves for different multipole orders. The curves seem to converge towards a single curve for higher M. (b) Detailed view of the behaviour around the main resonance peak. (c) Detailed view of the behaviour close to the ‘shoulder’ around 2.7 eV. Note that the higher order multipoles are needed to describe this feature.

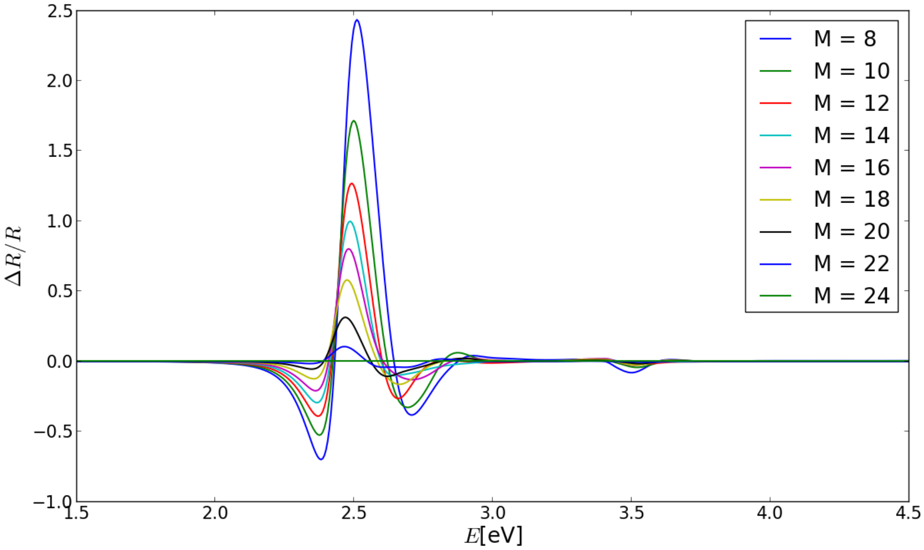

Figure 6.18: SDRS curves for different multipole orders, where the $M = 24$ curve have been subtracted from all other curves. The curves converges towards this 'true' curve with increasing multipole order M.

7. Characterization of eigenmodes

As discussed in section 2.3, the peaks and valleys in the SDR spectrum of an island film are due to plasmon resonances. Using the functionality included in GRANFILM of evaluating the potential in the near-field around an island, these plasmon modes can be studied in more detail. This is the subject of this chapter. Section 7.1 discusses two methods of finding the resonance energies of a particular geometry, while section 7.2 is a study of the resonances modes in the case of a hemispherical island covered by an oxide coating. In section 7.3 the hybridized plasmon modes of a metallic shell are studied.

7.1. Localization of resonances

When solving the system of equations in Eqs. (4.68)–(4.69) in GRANFILM, the linear system of equations is first written in the matrix form

$$A\mathbf{x} = \mathbf{b} \tag{7.1}$$

where A is the matrix containing the integral abbreviations in Eqs. (4.44), (4.45), (4.50) and (4.51) (also called *matrix elements*), $\mathbf{x}$ is a vector containing the unknown expansion coefficients $A_{\ell m}^{(i)}$ and $B_{\ell m}^{(i)}$, and $\mathbf{b}$ is a vector containing the potential contributions from the incident radiation. The linear system is solved for $\mathbf{x}$ using a standard linear algebra library [17], and the potential expansion coefficients are then used for calculating the island polarizabilities or evaluating the potential itself.

As all information about the island system is contained in the matrix A, one can use this to study the resonance modes of the system. By turning off the external field, *i.e.* setting $\mathbf{b} = \mathbf{0}$, one is left with the the corresponding *homogeneous* set of equations for the system

$$A\mathbf{x} = \mathbf{0}. \tag{7.2}$$

The non-trivial solutions $\mathbf{x}$ of this equation are the resonance modes or *eigenmodes* of the system, and the energies at which a non-trivial solution exists are its resonance energies. From linear algebra we know that in order for this equation to have any non-trivial solutions, the matrix A must be singular, which means that the determinant of A must be equal to zero [18]. The eigenmodes of the system can therefore be identified by calculating the determinant $\det(A)$ for a range of energies, and locating the energies for which $\det(A)$ is zero. The system is still energy dependent, even with no incident radiation, due to the complex dielectric functions $\varepsilon_i(\omega)$ of the media.

When the incident field is set to zero, the system described by Eq. (7.2) is essentially a damped oscillating system with no driving forces. The damping forces comes from the imaginary part of the complex dielectric functions $\varepsilon_i(\omega)$, which give rise to an exponentially decaying factor in the electric field. In order to be able to study the resonances in more detail, GranFilm includes an option of reducing these damping forces artificially by setting the imaginary part of the dielectric function to a small number. As seen from Eq. (2.25), this increases the quality factor Q, and thus the lifetime, of the surface plasmons. This has the effect of enhancing the resonant behaviour of the system, without affecting the location of the resonances.

The fact that the dielectric functions are complex also means that any zeros of $\det(A)$ do not necessarily lie on the real energy axis, but rather somewhere in the complex frequency plane. By reducing the imaginary part of the dielectric function, these zeros move closer to the real axis, and they should therefore become easier to identify when studying $|\det(A)|$ for a range of (real) energies.

In the results below the imaginary part of the dielectric function is set to 1% of its physical value, which effectively removes most of the damping in the system.

The test case studied in this section consists of hemispherical silver islands of radius 8.0 nm on a MgO substrate, surrounded by air. This is the same test case as was used in [3], and similar resonances to those found there should therefore be expected in these tests. The parameters of this test system are summarized in Table 7.1.

In Figure 7.1, the normalized[1] SDRS curves for this system are compared for the cases of physical dielectric functions and reduced damping.

---

[1] Divided by its maximum value. Here the amplitudes of the resonance peaks are not relevant, only their location on the energy axis.

Parameter set 2a		
Substrate medium		MgO
Island medium		Ag
Radius	R	8.0 nm
Truncation ratio	t_r	0.0
Multipole order	M	16

Table 7.1: Main test parameters used in the GranFilm runs of this section.

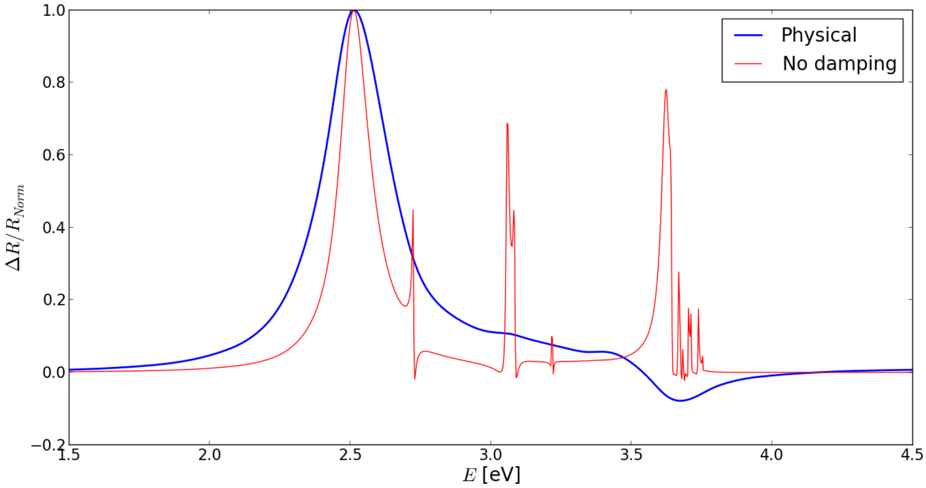

Figure 7.1: Comparison of the (normalized) SDRS curves in the case of a physical dielectric function and in the case where the damping has been artificially reduced by 99 %.

From this it can be seen that the removal of damping leads to sharper resonance peaks. In Figure 7.2 the absolute value of $\det(A)$ for $m = 0, 1$ in the undamped system is plotted for a range of energies and compared with the normalized SDRS curve. Although the determinant reaches extremely high values and is nowhere near zero for any energy, it is clear that each resonance peak corresponds to a dip of several orders of magnitude in the determinant of one of the matrices ($m = 0$ or $m = 1$). This agrees with what one would expect from the discussion above, and indicates that the actual zeros lie in the complex plane, close to these dips.

By turning the damping completely off, *i.e.* setting $\text{Im}[\varepsilon] = 0$ for the island, and increasing the resolution on the energy axis it is observed that the dips in $|\det(A)|$ grow deeper. It seems likely that $|\det(A)|$ reaches

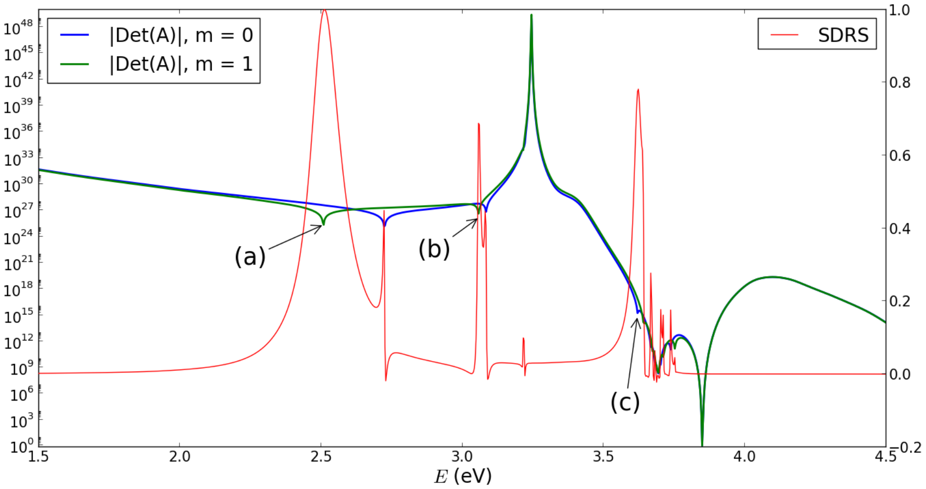

Figure 7.2: The absolute values of the determinant of the matrix A, for different energies and $m = 0, 1$. The corresponding SDRS curve is plotted for the same energies. Note that each resonance peak in the SDRS curve corresponds to a dip in the matrix determinant.

zero in the center of the dips, but it was not possible to observe this, even at very high resolutions.

In Figure 7.2 the dips corresponding to the three main resonances (a), (b) and (c) of the SDRS curve have been marked. When plotting the potential at the corresponding energies, the resonance modes which lead to the peaks can be identified. This is done in Figure 7.3, and the three resonances are recognized as

(a) a dipolar mode, parallel to the substrate,

(b) a quadrupolar mode,

(c) a dipolar mode, perpendicular to the substrate.

These results agree with the resonance modes found for the same system in [3].

Note also from Figure 7.2 that the resonances (a) and (b) correspond to a dip in $|\det(A)|$ for the $m = 1$ system of equations, while (c) corresponds to a dip in $|\det(A)|$ for $m = 0$. One would therefore expect the (c) mode to be rotational symmetrical around the z-axis, since the spherical harmonics $Y_{\ell m}$ with $m = 0$ all have this symmetry. This seems to agree with Fig. 7.3c.

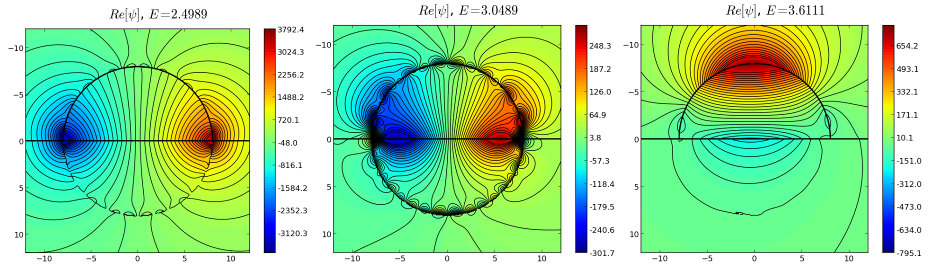

(a) (b) (c)

Figure 7.3: Potential maps of the system at the three main resonance energies, showing the three main resonance modes. (a) Parallel dipolar mode at $E = 2.50$ eV (b) Quadrupolar mode at $E = 3.05$ eV (c) Normal dipolar mode at $E = 3.61$ eV.

Eigenvalues of A

Another way of looking for solutions to Eq. (7.2), is to first find the eigenvalues λ_i and eigenvectors $\mathbf{v}_i$ of the matrix A. This is done by solving the eigenvalue system

$$A\mathbf{v} = \lambda\mathbf{v}. \tag{7.3}$$

When an eigenvalue λ_i approaches zero, one is left with the homogeneous equation above, Eq. (7.2). In the limit of an eigenvalue λ_i equal to zero, the matrix A must be singular (*i.e.* have a determinant equal to zero), because the eigenvector $\mathbf{v}_i$ is non-zero by definition [18]. To look for energies where an eigenvalue of A approaches zero is thus equivalent to looking for energies where $\det(A)$ approaches zero, and the energies at which this occurs will therefore again correspond to the eigenmodes of the system. In Figure 7.4 the inverse of the minimum absolute value of the eigenvalues of the matrix A is plotted for each energy and for $m = 0, 1$, and compared with the SDRS curve. In Figure 7.5 the same is shown for the case where the damping part of the dielectric function again has been artificially reduced to 1 % of its actual value. From these figures it is quite clear that the resonances of the SDRS curve occur at the energies where the smallest absolute eigenvalue of A approach zero.

Notice from Figure 7.4 that the valley in the SDRS curve at (c) seems to occur at a slightly higher energy than the corresponding maxima in $1/\min|\lambda_i|$. The reason for this energy shift is seen when the damping is removed in Figure 7.5. The complex behaviour in $1/\min|\lambda_i|$ around 3.7 eV leads to an equally complex response in the SDR spectrum at this energy. This seems to have the effect of shifting the observable dip in the

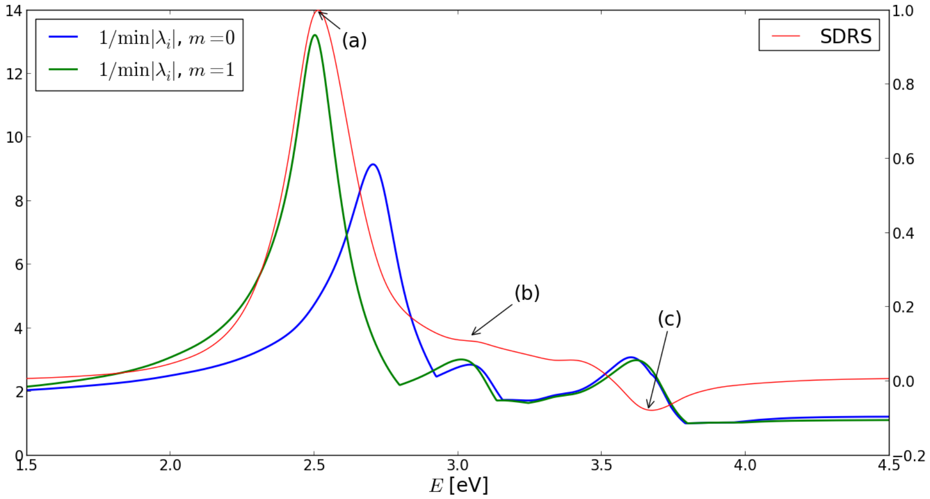

Figure 7.4: The inverse minimum absolute eigenvalues of A along with the SDRS curve for the test system with physical ε-values. The peaks of the SDRS curve seem to correspond to the various maxima in $1/\min|\lambda_i|$.

reflectance in Figure 7.4 towards a higher energy.

Although the eigenvalue-approach to locating the eigenmodes gives the same results as when looking for local minima in $|\det(A)|$, the sharper peaks in Figure 7.5 makes it easier to *i)* find the exact resonance energies and *ii)* distinguish between the $m = 0$ and the $m = 1$ peaks. This approach is therefore preferred in the next sections.

7.2. Oxide-coated islands

It is also useful to study how a dielectric coating layer on the metallic islands affects the eigenmodes, and the tests of the previous sections are therefore repeated for coated particles. The test system used in this section is therefore the same as in the previous section, but now with a dielectric coating layer on the hemispherical silver islands. In order to simulate the effect of the oxidisation process which occurs when silver is exposed to oxygen, the coating layer is set to consist of silver oxide. The thickness of the coating layer is such that the radius ratio of the silver core is 0.95. These system parameters are summarized in Table 7.2.

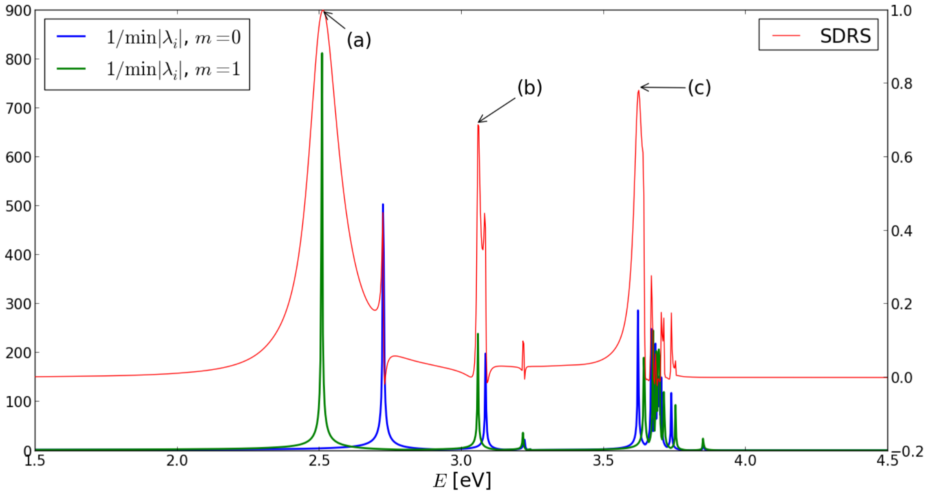

Figure 7.5: The inverse minimum absolute eigenvalues of A along with the normalized SDRS curve for the test system with Im[$\varepsilon_{\mathrm{Ag}}$] reduced to 1 % of its actual value. Here each peak in the SDRS curve is clearly related to a $m = 0$ or $m = 1$ eigenvalue approaching zero.

7.2.1. Coated island resonances

In Figure 7.6 the differential reflectivity curve of the coated system is plotted along with the inverse minimum absolute eigenvalues of the matrix A. When comparing this to the uncoated system in Figure 7.5, it is observed that the main resonances are shifted towards lower energies, and also that some new resonances arise. Note how the complex behaviour of the SDRS curve around 3.7 eV in the uncoated case has been replaced by a single sharp peak in the coated case. Instead, six new and approximately equidistant peaks have arisen in the region $2.7 - 3.2$ eV.

The potential at the five peaks (a)–(e) is depicted in Figure 7.7a–7.7e. The potentials at these energies suggest that the resonances can be attributed to the following modes:

(a) A dipolar mode, parallel to the substrate. This is similar to the mode in Figure 7.3a.

(b) Possibly a quadrupolar mode, similar to the one in Figure 7.3b.

(c) A quadrupolar mode. Note that this mode was not observed in the uncoated case.

Parameter set 2b		
Substrate medium		MgO
Core medium		Ag
Coating medium		Ag_2O
Radius	R	8.0 nm
Core radius ratio	χ_2	0.95
Truncation ratio	t_r	0.0
Multipole order	M	16

Table 7.2: Main test parameters used in the GranFilm runs of this section.

(d) A normal dipolar mode, or possibly a quadrupolar mode (due to the small minima close to the substrate).

(e) A normal dipolar mode, similar to the one in Figure 7.3c.

The eigenmodes found for the uncoated islands in the previous section are thus also found in the coated case, but at different energies. Note that some of the resonances are difficult to attribute to a single plasmon mode. For the (c) and (e) resonances, this can be explained by the fact that there is a peak in $1/\min(|\lambda_i|)$ for both $m = 0$ and $m = 1$ at these energies. This means that the potentials in Figures 7.7c and 7.7e could be combinations of two eigenmodes.

7.2.2. Dependence on coating thickness

For a more quantitative study of the effect of adding a dielectric coating to the island, the differential reflectivity curves for varying coating thickness are calculated and the positions of the various resonance peaks compared. In Figure 7.8 this is shown in the cases of no coating and a coating of $0.1R$. Here it can be seen that all the resonance peaks are shifted towards lower energies, by various amounts. In Figure 7.9 this is shown more systematically for a coating thickness ranging from 0 to $0.2R$. This shows that the resonances all shift towards lower energies with increasing coating thickness. It is, however, worth noting that this effect is greatest for a thin layer of coating. This means that even a really thin layer of dielectric coating can have a large impact on the resonance energies.

It should be noted that in the tests above the thickness of the coating layer was increased by reducing the radius ratio of the metal core. This means that the properties of the system in theory could change not only due to the thickness of the coating layer, but also because the metallic

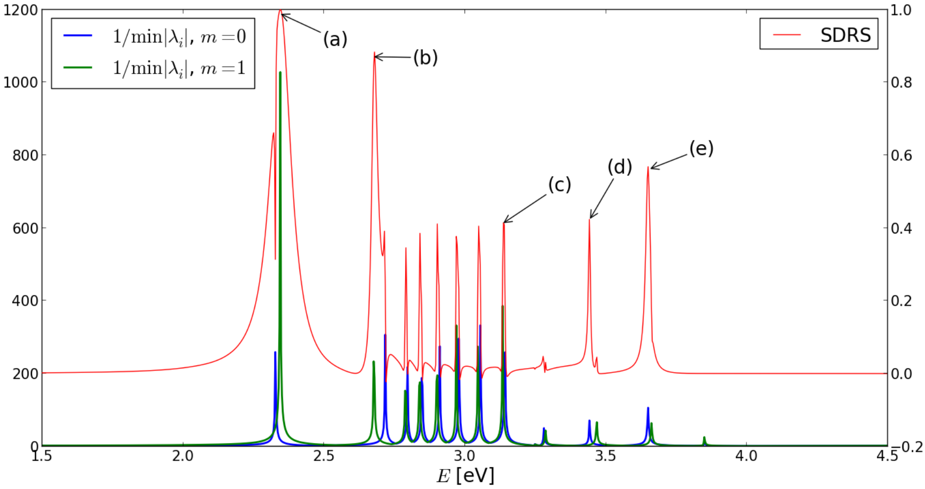

Figure 7.6: The inverse minimum absolute eigenvalues of A along with the normalized SDRS curve for the coated test system with $\mathrm{Im}[\varepsilon_{\mathrm{Ag}}]$ reduced to 1 % of its actual value.

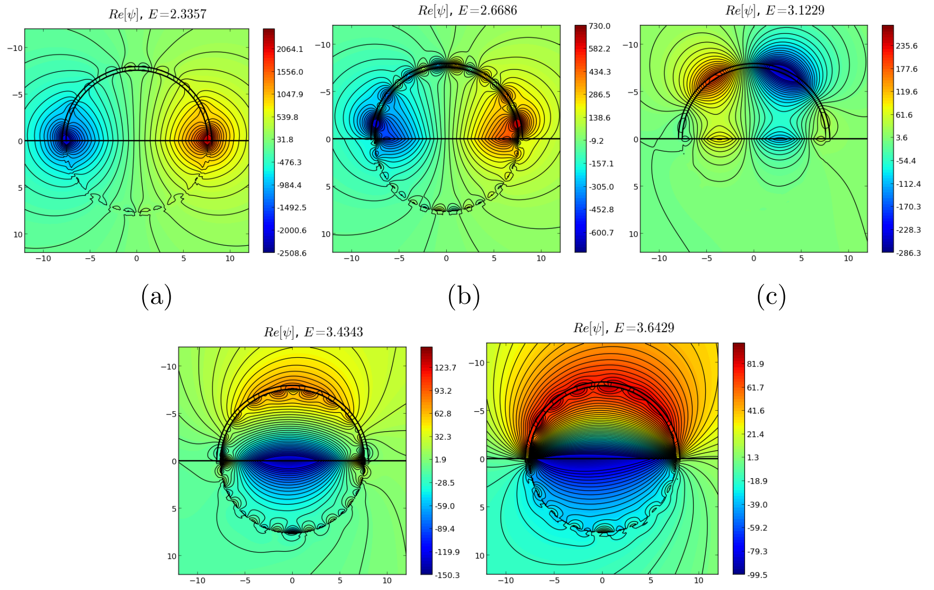

(a)

(b)

(c)

(d)

(e)

Figure 7.7: Maps of the real part of the potential at the energies indicated in Figure 7.6. (a) Parallel dipolar mode at $E = 2.34$ eV (b) Possible quadrupolar mode at $E = 2.67$ eV (c) Quadrupolar mode at $E = 3.12$ eV (d) Normal dipolar, or possible quadrupolar mode at $E = 3.43$ eV (e) Normal dipolar mode at $E = 3.64$ eV.

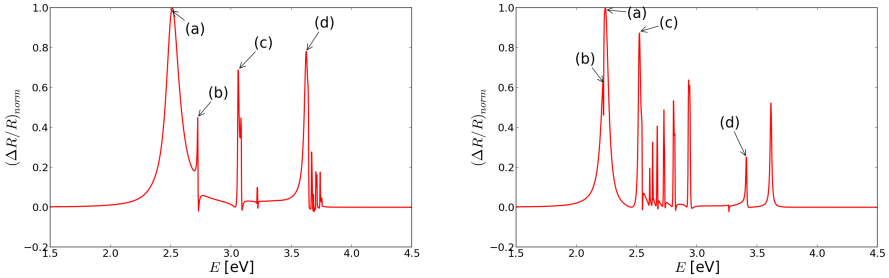

Figure 7.8: Normalized SDRS curves in the cases of uncoated islands (left) and islands with an oxide coating of thickness $0.1R$ (right). Note how the resonances (a)–(d) shifts towards lower energies when the coating is applied.

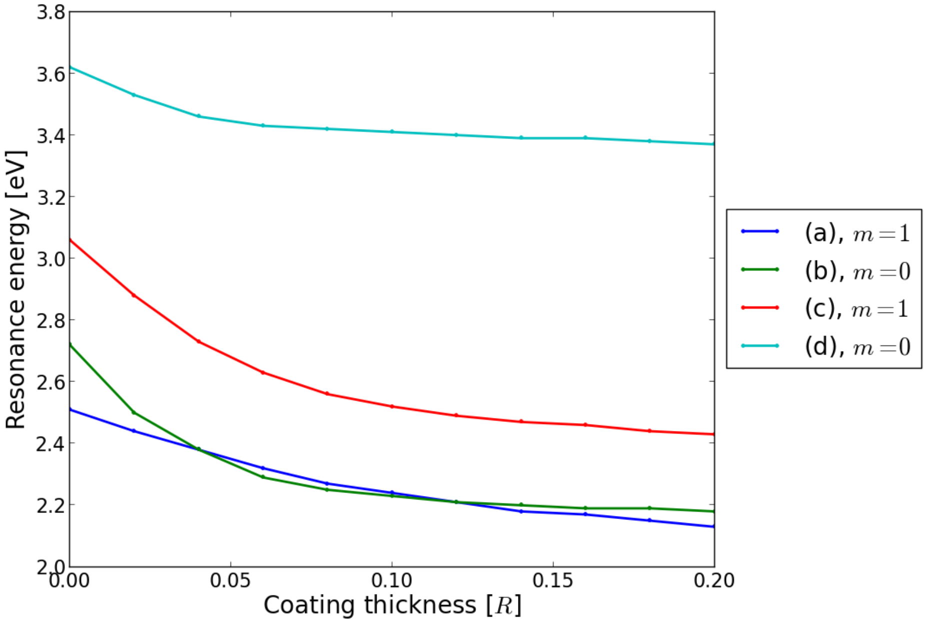

Figure 7.9: Position of the resonances (a)–(d) in Figure 7.8 on the energy axis with varying coating thickness.

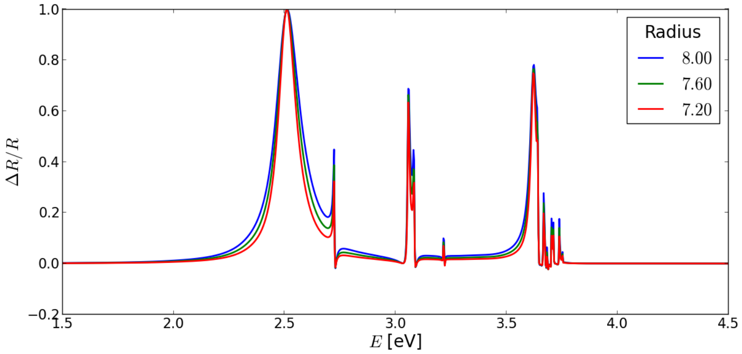

Figure 7.10: SDRS curves of uncoated, spherical islands of three different radii. The position of the resonance peaks on the energy axis is not dependent on the particle radius.

islands are getting relatively smaller. In order to rule out the effect of this, the SDRS curves for three uncoated hemispherical island systems of varying radius are compared in Figure 7.10. This shows that although the radius has some effect on the amplitude of the resonances, their position on the energy axis is not changed by varying the radius. The movement of the resonances along the energy axis observed in Fig. 7.9 can therefore be attributed to the coating thickness alone.

7.2.3. Dependence on island interactions

When performing calculations in GranFilm, the metallic islands are placed in a regular lattice configuration with a typical distance between islands called the *lattice parameter* L. In the calculations up to this point, this distance has been assumed to be so large that each island can be considered an independent system. When this is not the case, GranFilm also has the option of including island–island interactions. This is done by taking into account not only contributions from the multipoles and image multipoles of the island itself, but also the multipoles and image multipoles of the neighbouring islands. As a first approximation, this is modelled by including a correction in the island polarizabilities of dipolar order, as described in [7].

In Figure 7.11 the SDRS curves have been plotted for the coated and uncoated systems with no corrections due to island–island interactions and with corrections to dipolar order included. By comparing the SDRS curves in these cases, it seems that the effect of turning island–island interactions on is smaller in the coated case than in the uncoated case. This makes

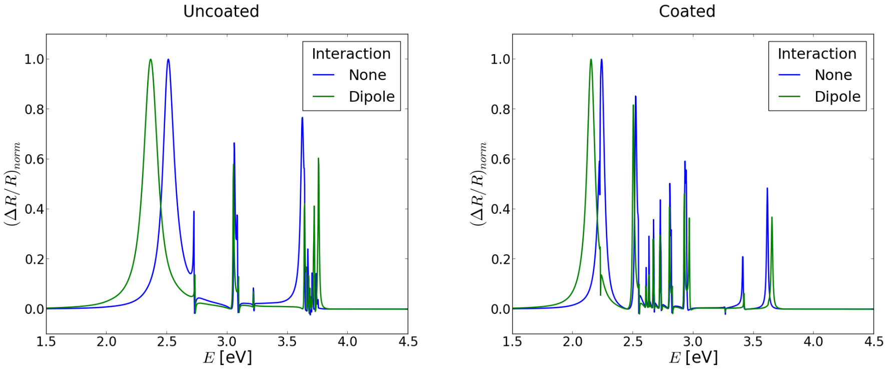

Figure 7.11: Effect of island–island interactions on the SDRS curves in the cases of uncoated islands (left) and islands with an oxide coating of thickness $0.1R$ (right). The islands are placed in a square lattice configuration with a lattice parameter of $L = 20$.

intuitively sense, as the dielectric coating 'shields' the islands from the contributions of its neighbours.

7.3. Resonances of metallic shells

As discussed in section 2.3.1, the plasmon resonances of a metallic shell can be found as a hybridization of the plasmon modes of a metallic sphere and a spherical cavity in a metal. For the metallic shell, these modes are split into a low energy symmetric mode and a high energy antisymmetric mode. The physics behind this hybridization of plasmons is not expected to change considerably for truncated particles, and one could therefore expect to observe the same behaviour when placing truncated metallic shells on a substrate.

The test case used when looking for this effect consists of hemispherical silver shells around cores of glass[2], placed on a MgO substrate. The radius ratio of the inner glass core is 0.7, and the damping of the system is still artificially reduced by setting Im$[\varepsilon_{\mathrm{Ag}}]$ to 1 % of its actual value, in order to better locate the resonances. The system parameters are summarized in Table 7.3

When plotting the inverse minimum absolute eigenvalues together with the SDRS curve of the system, the main resonances are identified, as seen in Figure 7.12. Here, the two $m = 1$ peaks corresponding to the symmetric

---

[2] More specifically, borosilicate crown glass (BK7).

Parameter set 3		
Substrate medium		MgO
Core medium		Glass (BK7)
Shell medium		Ag
Radius	R	8.0 nm
Core radius ratio	χ_2	0.7
Truncation ratio	t_r	0.0
Multipole order	M	16

Table 7.3: Main test parameters used in the GranFilm runs of this section.

and antisymmetric plasmon modes are marked. The potential maps at these energies are shown in Fig. 7.13–7.14, and the potential at (a) and (b) are recognized as the symmetric and antisymmetric configurations in the schematic in Fig. 2.2, respectively. The energy of the symmetric mode is lower than the energy of the antisymmtric mode, in agreement with the hybridization model.

In section 7.1, the same system is studied, but with solid silver hemispheres instead of hemispherical shells. The corresponding dipolar plasmon energy of this system lies between the hybridized energies, as seen in Figs. 7.2–7.3a, so that

$$E_{symmetric} < E_{solid} < E_{antisymmetric}. \tag{7.4}$$

This also agrees with the schematic in Fig. 2.2.

Note that the maxima of the potentials in the symmetric mode in Figure 7.13a are more than one order of magnitude higher than in the antisymmetric mode in Figure 7.13b. This makes sense, since the potential maxima and minima of this mode are quite close and are thus partially cancelling each other out. The fact that the symmetric mode corresponds to the main resonance peak in the SDR spectrum, while the antisymmetric mode gives a lower and narrower peak, can also be attributed to this.

In Figure 7.15 the SDR spectrum in the case of physical Im[ε]-values is compared with the spectrum in the case of reduced damping, which is studied in this section. From this it is observed that the antisymmetric mode is responsible for a small local maximum in the observable SDRS curve of the system as well.

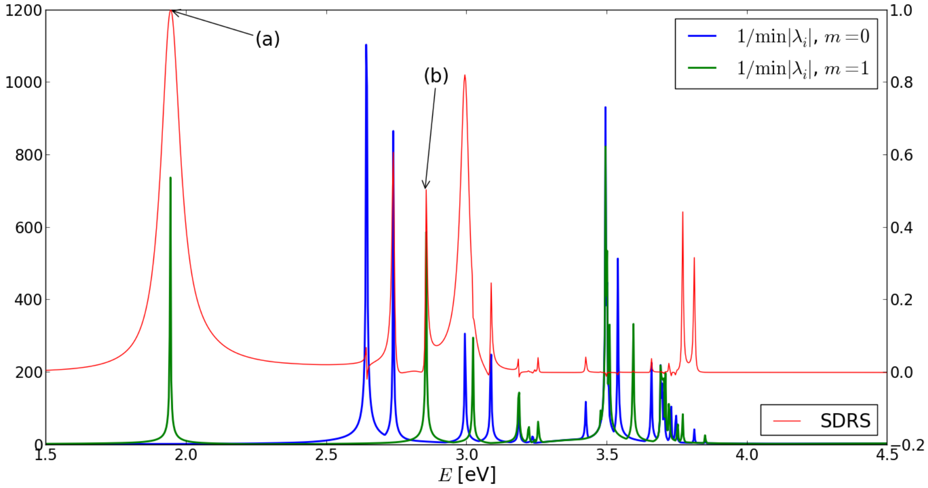

Figure 7.12: Inverse minimum absolute values of the eigenvalues of the matrix A along with the SDR spectrum for the metallic shell system defined in Parameter set 3.

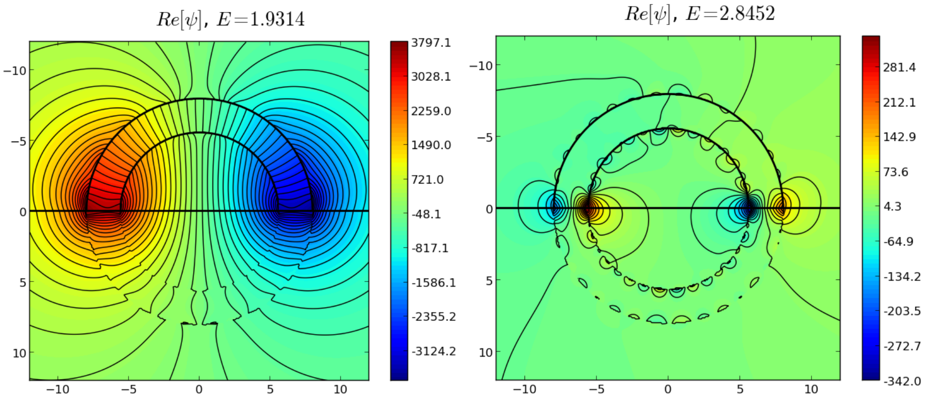

(a) (b)

Figure 7.13: Potential maps of the metallic shell system showing the two hybridized resonance modes. (a) Symmetric mode at $E = 1.93$ eV. (b) Antisymmetric mode at $E = 2.85$ eV

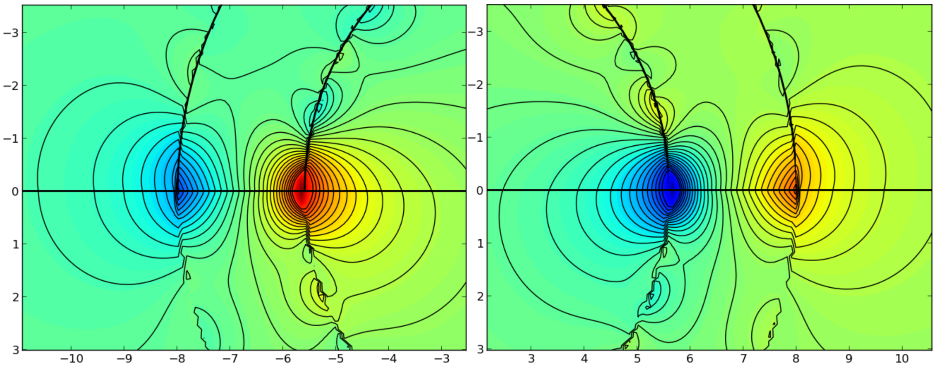

Figure 7.14: Close-up view of the left and right part of the antisymmetric mode in Figure 7.13b.

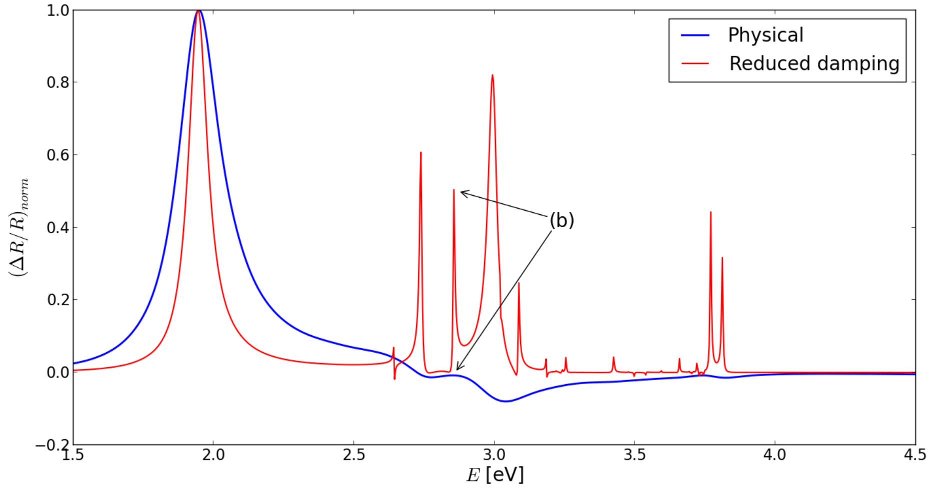

Figure 7.15: Normalized SDRS curves of the system in the case where the actual (physical) ε-values have been used and in the case where damping is reduced by setting $\mathrm{Im}[\varepsilon_{\mathrm{Ag}}]$ to 1 % of its actual value. The antisymmetric hybridized mode at (b) leads to a small maximum in the physical case as well.

8. Summary and conclusions

The first goal of this work was to implement into GranFilm the functionality needed in order to calculate the optical properties of an island film of truncated and coated prolate spheroidal nanoparticles, as derived in chapter 4. The implementation was carried out and the code checked thoroughly for errors. The fact that the functionality was to be added to the existing GranFilm 2.0 framework and not be built from scratch, made the implementation a more manageable task. Although consisting of a vast body of code, the GranFilm framework has clearly been built with such future additions in functionality in mind, which made my job of adding prolate spheroid support easier. I have tried to follow this principle of allowing for future additions and modifications in my code as well.

The second goal of this work was directly linked to the first, and consisted of testing the implementation of the new functionality rigorously in the appropriate limits. In fact, this turned out to be the most time-consuming part of this thesis. In section 6.2, the various test are detailed. The new code is first shown to give results in the spherical limit that are consistent with the results from the old code. This is done by studying the main output of the program, which is the differential reflectance spectrum (SDRS) of the surface system, in this limit. By changing the radii of the island particles slightly in a number of subsequent runs, the particle shape changes from oblate spheroidal to spherical and then from spherical to prolate spheroidal, invoking all three branches of the code. By comparing the SDR spectra in these runs, they are found to converge towards the spherical case from both sides, as can be seen in Figures 6.2–6.3. The same is observed when the islands have a dielectric coating, as can be seen in Figures 6.4–6.5. Although it is not a proof of correctness that the SDRS curves behave consistently for the three geometries in the spherical limit, it is certainly a good indication that the implementation was successful.

Another possible output of GranFilm is the potential in the near field evaluated at a set of points specified by the user. When plotting the real part of the potential in the cross-section of an island for the three different geometry types in the spherical limit, the same qualitative behaviour should be expected. This is done in section 6.2.2, and by comparing Figures 6.6a–6.6c, it is seen that the potential evaluated by the new prolate implementation exhibits the same behaviour as in the two other geometries.

It was, however, observed that if one tries to use the spheroidal code on geometries too close to the spherical limit, the SDRS curves behave oddly or the calculation breaks down entirely. This is due to numerical issues arising from the fact that $\xi_0 \to \infty$ and $a \to 0$ for spheroids in the spherical limit. This means that the user must be careful when studying spheroidal systems close to the spherical limit. In the case of a geometry very close to a sphere, it is probably best to approximate the islands as spheres and perform the calculations using the spherical branch of the GranFilm program.

The tests above are of course just indications that the implementation has been carried out without error. The ultimate test of the correctness of the implementation is to check that the boundary conditions, Eq. (4.4), at the spheroidal interfaces are fulfilled. From the uniqueness theorem we know that if the potential is a solution of Laplace's equation and satisfies the boundary conditions of the system, this must be the one and only solution. Since the multipole expansions for the potential in Eqs. (4.26)–(4.27) satisfy Laplace's equation and the boundary conditions at the flat interfaces by construction, it is the degree to which the boundary conditions at the spheroidal interfaces are fulfilled that decides the success of the implementation. In section 6.2.3 this fulfilment is tested quantitatively, and the results are presented in Figures 6.7–6.10. These results show that both boundary conditions are relatively well satisfied at all the spheroidal interfaces. It is noted that the first boundary condition is better satisfied than the second, but this is not unreasonable, since the derivatives of the potential are expected to change more rapidly than the potential itself. At all the spheroidal interfaces, the biggest error is observed at the interface between the ambient and the substrate. There are at least two reasons why this makes sense. First, this is the point where the spheroidal interface crosses the substrate interface, and when potential in this region is forced into fulfilling the boundary conditions at both interfaces simultaneously, this could lead to conflicts. Second, as seen in Figures 6.6a–6.6c, this is the region where the potential has the largest value for the particular resonance corresponding to the main peak in the SDRS curve. Since this is the region with the most dramatic behaviour in the potential, it is reasonable that the error is greatest here.

The continuity of the normal derivatives of the potential times the permittivity, $\varepsilon\partial_n\psi$, across a spheroidal interface was checked using a finite-difference approximation of the derivatives. When checking the fulfilment of this boundary condition for an island with high truncation ratio, this calculation broke down, as seen in section 6.2.4. The reason for this was not found, but in order to make sure that this boundary condition was satisfied for this system as well, an analytical calculation of the normal derivatives was implemented. This calculation proved successful.

In theory, an infinite number of multipoles are needed in order for the potential expansion to be valid. In practice this is impossible, and the multipole expansion must be truncated at an order M. One would, however, expect the results to improve with an increasing number of multipoles, and this is also observed in the implementation, as seen in section 6.2.5. While more multipoles are always better in the analytical derivation, the picture is different when it comes to numerics. This is due to the finite precision of the numbers used in the calculation. This is a purely numerical effect, but may actually lead to higher errors when including multipoles of very high orders. The result is that the number of multipoles to be included in the calculation must be chosen from a finite interval. Too few multipoles will lead to imprecise results, while too many will give these round-off errors. The maximum number of multipoles that can be included before such errors start dominating seem to depend on the geometry of the system, but was observed to be as low as the mid-twenties in some cases. Most of the GRANFILM runs performed in this work used $M = 16$, which gave satisfactory results without taking too much time.

The third goal of this thesis was to study the resonance modes of supported island particles. A reasonable place to start is always to try to reproduce results found by others, so first the resonance modes of a simple film of uncoated, hemispherical silver islands was studied. This was the same system studied by Lazzari and Simonsen in [3], and the resonance modes should therefore match the ones identified there. As can be seen in Figure 7.3, the three main resonance modes for this system could be identified as a parallel dipolar mode, a quadrupolar mode and a normal dipolar mode using GRANFILM. This was in agreement with the results in [3].

The resonance modes were located on the energy axis in two different ways. Both methods used the fact that the matrix A containing the integral terms of the system of equations for the multipole expansion coefficients is singular at a resonance energy. These energies were first located by studying the absolute value of the determinant of the matrix, since the determinant should approach zero when the matrix becomes singular. It turned out that the determinant did not approach zero at any energy tested. It did, however, have dips of several orders of magnitude at certain energies. These energies corresponded to the energies at which a peak or a valley (indicating resonant behaviour) was observed in the SDRS curve of the island film. By increasing the resolution on the energy axis, it was observed that the dips grew deeper, but it was not possible to find the exact zero. This is probably due to the finite precision in the calculations. The second method of locating the resonance energies was to study the eigenvalues of the matrix A. In a similar way, the smallest absolute value of the eigenvalues should approach zero when the matrix becomes singular, and the energies at which this happens will therefore correspond to the resonance energies of the system. Like the determinant, the eigenvalues did not reach exactly zero, but by plotting the inverse minimum absolute value of the eigenvalues, a series of sharp peaks could be seen. These corresponded exactly to the various peaks in the SDRS signal, and made it easy to identify the possible resonance energies of the system. Because of the sharper peaks, the eigenvalue method was therefore found to be the better of the two methods of locating the resonances.

The resonance modes of a film of coated hemispherical islands were also studied, and the results are presented in section 7.2.1. These results show that the dielectric coating has the effect of shifting the resonances towards lower energies. The added coating also results in a more complex response with more dominating resonances, as seen when comparing Figures 7.5 and 7.6. The main eigenmodes corresponding to these resonances can be found by studying the potentials in Fig. 7.7. Here the three modes found in the uncoated system are found again, in addition to two new ones. These were difficult to characterize, but are likely dipolar or quadrupolar too.

The resonance modes of this coated system were then studied with varying thickness of the coating. By gradually increasing the coating thickness, it was observed that the resonance modes were shifted towards lower energies and that this effect was greatest when the coating was thinnest. This is shown in Figure 7.9. This means that even a very thin layer of coating will have a big impact on the location of the resonances. When studying the correction in the SDRS spectrum due to island-island interactions for metallic islands with and without a dielectric coating, it was also observed that the correction is smaller in the coated case. This agrees with what one intuitively would expect, since the dielectric coating layer can be considered a shielding layer, thereby isolating the neighbouring islands from each other.

The final test case studied in this work was a truncated metallic shell system. This consisted of an island film of hemispherical silver shells with glass cores. The plasmon modes of such a nanoshell have been shown to be a hybridization of the modes supported by a solid metal particle and by a cavity in a metal [9]. It was expected that a film of hemispherical shells would show a similar behaviour, and the resonances of this system were therefore located and maps of the potential at these energies compared. As Figure 7.13 shows, the hybridization also occurs in this system. The single parallel dipolar mode found in the solid silver islands is split into two new modes, a low energy symmetric one and a high energy antisymmetric one. By comparing the energies of these two modes with the energy of the single solid silver mode, found in section 7.1, it is observed that the energy of this original mode lies between the energies of the two hybridized ones, as it should according to the hybridization model.

In conclusion, the three main goals of this thesis can be said to have been reached. The prolate spheroid functionality added to GranFilm seems to behave as it should, and the various tests performed confirm this numerically. The plasmon resonance modes of various metallic islands have been studied in more detail, with some interesting results. In particular, the fact that plasmonic hybridization of a metallic shell can be observed in GranFilm is an interesting find.

With the implementation of prolate spheroid support, GranFilm now supports island films of a wide range of geometries. In theory, islands shapes ranging from flat discs to thin needles are now supported, but these limits have not been tested. Some further study of the performance of the software in these limits could therefore be useful. Support for the case of islands only slightly truncated by the substrate, with internal layers entirely lying above the substrate, could also be a useful future addition to GranFilm.

Bibliography

[1] S. Stavseng, “Optical properties of prolate spheroidal nanoparticles supported by a substrate,” specialization project, NTNU, 2012.

[2] I. Simonsen, R. Lazzari, J. Jupille, and S. Roux, “Numerical modelling of the optical response of supported metallic particles,” *Phys. Rev. B*, vol. 61, pp. 7722–7733, 2000.

[3] R. Lazzari and I. Simonsen, “Granfilm: a software for calculating thin-layer dielectric properties and fresnel coefficients,” *Thin Solid Films*, vol. 419, pp. 124 – 136, 2002.

[4] J. Steele, N. Grady, P. Nordlander, and N. Halas, “Plasmon hybridization in complex nanostructures,” in *Surface Plasmon Nanophotonics* (M. Brongersma and P. Kik, eds.), vol. 131 of *Springer Series in Optical Sciences*, pp. 183–196, Springer Netherlands, 2007.

[5] M. I. Stockman, “Nanoplasmonics: The physics behind the applications,” *Physics Today*, vol. 64, no. 2, 2011.

[6] A. G. Brolo, “Plasmonics for future biosensors,” *Nature Photonics*, vol. 6, no. 11, 2012.

[7] D. Bedeaux and J. Vlieger, *Optical properties of surfaces.* Imperial College Press, London, 2nd ed., 2004.

[8] I. Simonsen and R. Lazzari, “GranFilm: Optical Properties of Granular Thin Films.” `http://web.phys.ntnu.no/~ingves/Software/GranFilm/Current/`, 2003.

[9] E. Prodan, C. Radloff, N. J. Halas, and P. Nordlander, “A hybridization model for the plasmon response of complex nanostructures,” *Science*, vol. 302, no. 5644, pp. 419–422, 2003.

[10] D. Griffiths, *Introduction to Electrodynamics.* Pearson, San Francisco, 3rd ed., 2008.

[11] S. Maier, *Plasmonics: Fundamentals and Applications.* Springer Science, 2007.

[12] L. Novotny and B. Hecht, *Principles of Nano-Optics.* Cambridge University Press, 2006.

[13] K. Rottmann, *Matematisk formelsamling.* Spektrum, 2003.

[14] "Wikimedia Commons." `http://commons.wikimedia.org/wiki/File:ProlateSpheroidCoord.png`.

[15] I. Simonsen, "Note on the potential expansion (GranFilm Note)." Unpublished, 2012.

[16] E. Aursand, "Optical properties of truncated and coated spheroidal nanoparticles on a substrate," Master's thesis, NTNU, 2012.

[17] E. Anderson, Z. Bai, C. Bischof, S. Blackford, J. Demmel, J. Dongarra, J. Du Croz, A. Greenbaum, S. Hammarling, A. McKenney, and D. Sorensen, *LAPACK Users' Guide.* Philadelphia, PA: Society for Industrial and Applied Mathematics, 3rd ed., 1999.

[18] E. Kreyszig, *Advanced Engineering Mathematics.* John Wiley And Sons USA, 9th ed., 2007.

A. Dimensionless equations

When implementing Eqs. (4.72)–(4.73) in GranFilm, a slightly modified set of equations are actually used, in order for the multipole coefficients to be dimensionless. This convention was used in the original GranFilm implementation, as described in [3, 16], and the equations for the prolate spheroidal system was therefore implemented in a similar way.

The multipole expansions coefficients $A_{\ell m}^{(i)}$ and $B_{\ell m}^{(i)}$ as defined in Eq. (4.17) have the dimensions $\mathrm{Vm}^{\ell+1}$ and $\mathrm{Vm}^{-\ell}$, respectively. In the implementation, these have been replaced by their dimensionless equivalents, defined as

$$\begin{aligned}\widehat{A}_{\ell m}^{(i)} &= R_{\perp,1}^{-\ell-2} A_{\ell m}^{(i)} / E_0 \\ \widehat{B}_{\ell m}^{(i)} &= R_{\perp,1}^{\ell-1} B_{\ell m}^{(i)} / E_0\end{aligned} \tag{A.1}$$

where $R_{\perp,1}$ is the semimajor axis of the outermost spheroidal interface and E_0 is the field strength of the incident radiation. When replacing the coefficients in Eqs. (4.72)–(4.73) with these dimensionless quantities, the new set of equations to be solved becomes

$$
\begin{aligned}
&\sum_{\ell'=1}^{M} \zeta_{\ell\ell'}^{m} \chi_s^{-\ell'-2}\Big[\widehat{A}_{\ell' m}^{(2s-1)}\mathcal{I}_{\ell\ell'}^{m(2s-1)}(t_r^{(s)},\xi_{0,s}) - \widehat{A}_{\ell' m}^{(2s+1)}\mathcal{I}_{\ell\ell'}^{m(2s+1)}(t_r^{(s)},\xi_{0,s})\Big] \\
&+ \sum_{\ell'=1}^{M} \zeta_{\ell\ell'}^{m} \chi_s^{\ell'-1}\Big[\widehat{B}_{\ell' m}^{(2s-1)}\mathcal{K}_{\ell\ell'}^{m(2s-1)}(t_r^{(s)},\xi_{0,s}) - \widehat{B}_{\ell' m}^{(2s+1)}\mathcal{K}_{\ell\ell'}^{m(2s+1)}(t_r^{(s)},\xi_{0,s})\Big] \\
&= \delta_{s1}\sqrt{\frac{4\pi}{3}}\cos\theta_0\Big\{\xi_{0,1}^{-1}\frac{\varepsilon_1}{\varepsilon_2}\widetilde{X}_1^0(\xi_{0,1})\delta_{\ell 1} + \Big(\frac{\varepsilon_1}{\varepsilon_2}-1\Big)\Big[\sqrt{3}t_r^{(1)}\zeta_{\ell 0}^{0}Q_{\ell 0}^{0}(-1,t_r^{(1)}) \\
&- \xi_{0,1}^{-1}\zeta_{\ell 1}^{0}\widetilde{X}_1^0(\xi_{0,1})Q_{\ell 1}^{0}(-1,t_r^{(1)})\Big]\Big\}\delta_{m0} \\
&- \delta_{s1}\sqrt{\frac{2\pi}{3}}\xi_{0,1}^{-1}\sin\theta_0 e^{-i\phi_0}\widetilde{X}_1^1(\xi_{0,1})\delta_{\ell 1}\delta_{m1} \\
&\forall\ s=1,2,...,S;\ \ell=0,1,2,...,M;\ m=0,1,
\end{aligned}
\tag{A.2}
$$

and

$$
\begin{aligned}
&\sum_{\ell'=1}^{M} \zeta_{\ell\ell'}^{m} \chi_s^{-\ell'-2}\Big[\widehat{A}_{\ell' m}^{(2s-1)}\mathcal{J}_{\ell\ell'}^{m(2s-1)}(t_r^{(s)},\xi_{0,s}) - \widehat{A}_{\ell' m}^{(2s+1)}\mathcal{J}_{\ell\ell'}^{m(2s+1)}(t_r^{(s)},\xi_{0,s})\Big] \\
&+ \sum_{\ell'=1}^{M} \zeta_{\ell\ell'}^{m} \chi_s^{\ell'-1}\Big[\widehat{B}_{\ell' m}^{(2s-1)}\mathcal{L}_{\ell\ell'}^{m(2s-1)}(t_r^{(s)},\xi_{0,s}) - \widehat{B}_{\ell' m}^{(2s+1)}\mathcal{L}_{\ell\ell'}^{m(2s+1)}(t_r^{(s)},\xi_{0,s})\Big] \\
&= \delta_{s1}\xi_{0,1}^{-1}\Big\{\varepsilon_1\sqrt{\frac{4\pi}{3}}\cos\theta_0\frac{\partial\widetilde{X}_1^0(\xi)}{\partial\xi}\Big|_{\xi=\xi_{0,1}}\delta_{m0}\delta_{\ell 1} \\
&- \sqrt{\frac{2\pi}{3}}\sin\theta_0 e^{-i\phi_0}\frac{\partial\widetilde{X}_1^1(\xi)}{\partial\xi}\Big|_{\xi=\xi_{0,1}}\Big((\varepsilon_1-\varepsilon_2)\zeta_{\ell 1}^{1}Q_{\ell 1}^{1}(-1,t_r^{(1)}) + \varepsilon_2\delta_{\ell 1}\Big)\delta_{m1}\Big\} \\
&\forall\ s=1,2,...,S;\ \ell=0,1,2,...,M;\ m=0,1,
\end{aligned}
\tag{A.3}
$$

where it has been used that $R_{\perp,s} = \chi_s R_{\perp,1}$, where χ_s is the radius ratio of the interface s. Equations (A.2)–(A.3) are the ones that are actually solved in GRANFILM.

B. Integrals

In order to solve the system of equations for the multipole expansion coefficients, the integrals defined in Eqs. (4.39)–(4.40)

$$\widetilde{V}^{m}_{\ell\ell'}[\kappa_z,\xi](\eta_1,\eta_2) \equiv \int_{\eta_1}^{\eta_2} \mathrm{d}\eta P^{m}_{\ell}(\eta) P^{m}_{\ell'}(\eta_\kappa(\xi,\eta)) \widetilde{Z}^{m}_{\ell'}(\xi_\kappa(\xi,\eta)), \tag{B.1}$$

and

$$\widetilde{W}^{m}_{\ell\ell'}[\kappa_z,\xi](\eta_1,\eta_2) \equiv \int_{\eta_1}^{\eta_2} \mathrm{d}\eta P^{m}_{\ell}(\eta) P^{m}_{\ell'}(\eta_\kappa(\xi,\eta)) \widetilde{X}^{m}_{\ell'}(\xi_\kappa(\xi,\eta)), \tag{B.2}$$

and their derivatives with respect to ξ

$$\begin{aligned}\frac{\partial}{\partial\xi}\left[\widetilde{V}^{m}_{\ell\ell'}[\kappa_z,\xi](\eta_1,\eta_2)\right]_{\xi=\xi_0} = \int_{\eta_1}^{\eta_2} \mathrm{d}\eta P^{m}_{\ell}(\eta) \bigg\{ &\frac{\partial\eta_\kappa}{\partial\xi}\frac{\partial P^{m}_{\ell'}(\eta_\kappa)}{\partial\eta_\kappa}\widetilde{Z}^{m}_{\ell'}(\xi_\kappa) \\ &+ \frac{\partial\xi_\kappa}{\partial\xi}\frac{\partial\widetilde{Z}^{m}_{\ell'}(\xi_\kappa)}{\partial\xi_\kappa}P^{m}_{\ell'}(\eta_\kappa)\bigg\},\end{aligned} \tag{B.3}$$

$$\begin{aligned}\frac{\partial}{\partial\xi}\left[\widetilde{W}^{m}_{\ell\ell'}[\kappa_z,\xi](\eta_1,\eta_2)\right]_{\xi=\xi_0} = \int_{\eta_1}^{\eta_2} \mathrm{d}\eta P^{m}_{\ell}(\eta) \bigg\{ &\frac{\partial\eta_\kappa}{\partial\xi}\frac{\partial P^{m}_{\ell'}(\eta_\kappa)}{\partial\eta_\kappa}\widetilde{X}^{m}_{\ell'}(\xi_\kappa) \\ &+ \frac{\partial\xi_\kappa}{\partial\xi}\frac{\partial\widetilde{X}^{m}_{\ell'}(\xi_\kappa)}{\partial\xi_\kappa}P^{m}_{\ell'}(\eta_\kappa)\bigg\},\end{aligned} \tag{B.4}$$

need to be calculated numerically. The integrands of these integrals contains special functions which had to be implemented in GranFilm. In section B.1 the implementation of the Associated Legendre polynomials P^{m}_{ℓ} and Q^{m}_{ℓ}, the Prolate radial functions $\widetilde{Z}^{m}_{\ell'}$ and $\widetilde{X}^{m}_{\ell'}$ and their derivatives $\frac{\partial}{\partial\eta}P^{m}_{\ell}(\eta)$, $\frac{\partial}{\partial\xi}\widetilde{Z}^{m}_{\ell'}(\xi)$ and $\frac{\partial}{\partial\xi}\widetilde{X}^{m}_{\ell'}(\xi)$ is treated in detail. In section B.2 the implementation of the coordinate transformations $\xi_\kappa(\xi,\eta)$, $\eta_\kappa(\xi,\eta)$ and their derivatives $\frac{\partial}{\partial\xi}\xi_\kappa(\xi,\eta)$, $\frac{\partial}{\partial\xi}\eta_\kappa(\xi,\eta)$ is covered.

B.1. Legendre polynomials

The associated Legendre Polynomials are needed both in the implementation of the Spherical harmonics, Eq. (4.11), and in the implementations of the prolate $\widetilde{X}_\ell^m(\xi, a)$ and $\widetilde{Z}_\ell^m(\xi, a)$ functions, Eqs. (4.18a)–(4.18b). In the former case only the first order function is needed, defined on the interval $-1 \leq \eta \leq 1$. This was already in place in GranFilm, since these polynomials are also needed in the spherical and oblate spheroidal cases. In the latter case both the first and the second order functions are needed, now defined on the interval $1 \leq \xi < \infty$, where ξ is a real number. These are special for the prolate spheroidal case and were implemented in GranFilm using the definitions in Eqs. (4.7) and (4.9) and the following recursion formulas [13]

$$\begin{aligned} P_\ell^m(\xi) &= \frac{1}{\ell - m}[(2\ell-1)\xi P_{\ell-1}^m - (\ell+m-1)P_{\ell-2}^m] \\ Q_\ell^m(\xi) &= \frac{1}{\ell - m}[(2\ell-1)\xi Q_{\ell-1}^m - (\ell+m-1)Q_{\ell-2}^m]. \end{aligned} \tag{B.5}$$

From these formulae, all the associated Legendre polynomials of the first and second order, defined on the interval $1 \leq \xi < \infty$, can be determined from the first few terms, which can be found directly from the definitions in Eqs. (4.7) and (4.9)

$$\begin{aligned} P_0^0(\xi) &= 1 \\ P_1^0(\xi) &= \xi \\ P_1^1(\xi) &= -i\sqrt{\xi^2-1} \\ P_2^1(\xi) &= -3i\xi\sqrt{\xi^2-1} \\ Q_0^0(\xi) &= \frac{1}{2}\ln\left(\frac{\xi+1}{\xi-1}\right) \\ Q_1^0(\xi) &= \frac{1}{2}\xi\ln\left(\frac{\xi+1}{\xi-1}\right) - 1 \\ Q_1^1(\xi) &= -\frac{1}{\sqrt{\xi^2-1}}\left[\frac{1}{2}(\xi^2-1)\ln\left(\frac{\xi+1}{\xi-1}\right) - \xi\right] \\ Q_2^1(\xi) &= -\frac{1}{\sqrt{\xi^2-1}}\left[\frac{1}{2}(3\xi^3-3\xi)\ln\left(\frac{\xi+1}{\xi-1}\right) - 3\xi^2 + 2\right]. \end{aligned} \tag{B.6}$$

When calculating the integrals B.3–B.4, the derivatives of the associated Legendre polynomials with respect to ξ are needed. These can be found from a second set of recursion formulas [13]

$$\begin{aligned}\frac{\mathrm{d}}{\mathrm{d}\xi}P_\ell^m(\xi) &= \frac{1}{\xi^2-1}\left[(\ell-m+1)P_{\ell+1}^m(\xi)-(\ell+1)\xi P_\ell^m(\xi)\right]\\ \frac{\mathrm{d}}{\mathrm{d}\xi}Q_\ell^m(\xi) &= \frac{1}{\xi^2-1}\left[(\ell-m+1)Q_{\ell+1}^m(\xi)-(\ell+1)\xi Q_\ell^m(\xi)\right].\end{aligned} \tag{B.7}$$

It should be noted that the associated Legendre polynomials were implemented in GranFilm with quadruple precision in order to avoid round-off errors.

The prolate radial functions $\widetilde{X}_\ell^m(\xi,a)$ and $\widetilde{Z}_\ell^m(\xi,a)$, Eqs. (4.18a)–(4.18b), and their derivatives $\frac{\partial}{\partial\xi}\widetilde{X}_\ell^m(\xi,a)$ and $\frac{\partial}{\partial\xi}\widetilde{Z}_\ell^m(\xi,a)$ were implemented using the above Legendre polynomials. In order to avoid integer overflow when calculating the factorial factors in these expressions, these factors were re-written in the following way

$$\frac{(\ell-m)!}{(2\ell-1)!!} = \begin{cases}\displaystyle\prod_{i=1}^{\ell}\frac{i}{2i-1} & \text{if } m=0\\ \displaystyle\frac{1}{\ell}\prod_{i=1}^{\ell}\frac{i}{2i-1} & \text{if } m=1\end{cases} \tag{B.8}$$

and

$$\frac{(2\ell+1)!!}{(\ell+m)!} = \begin{cases}\displaystyle\prod_{i=1}^{\ell}\frac{2i+1}{i} & \text{if } m=0\\ \displaystyle\frac{1}{\ell+1}\prod_{i=1}^{\ell}\frac{2i+1}{i} & \text{if } m=1\end{cases} \tag{B.9}$$

where it was used that $(2k\pm1)!! = \prod_{i=1}^{k}(2i\pm1)$ and $k! = \prod_{i=1}^{k} i$.

B.2. Coordinate transformations

In addition to the transformations between prolate spheroidal coordinate systems shifted by Δz, as defined in Eqs. (3.16)–(3.17), the derivatives of these transformations are also needed when implementing the derivatives of the integrals $\widetilde{V}_{\ell\ell'}^m$ and $\widetilde{W}_{\ell\ell'}^m$ in Eqs. (B.3)–(B.4). By differentiating Eqs. (3.16) and (3.17) with respect to ξ, the following expressions are obtained

$$\frac{\partial}{\partial\xi}\xi'[\Delta z,a](\xi,\eta) = \frac{1}{\sqrt{2}}\left(C_7+\frac{\xi C_8}{2C_7}\right) \tag{B.10}$$

and

$$\frac{\partial}{\partial \xi}\eta'[\Delta z, a](\xi, \eta) = \sqrt{2}\left[\frac{\Delta z}{a\xi^2}\frac{1}{C_7} - \frac{1}{2}\left(\eta - \frac{\Delta z}{a\xi}\right)\frac{C_8}{C_7^3}\right], \tag{B.11}$$

where

$$\begin{aligned}
C_1 =& 1 + \frac{(\Delta z)^2}{a^2\xi^2} - \frac{2\Delta z}{a\xi}\eta + \frac{\eta^2}{\xi^2} \\
C_2 =& \frac{2}{\xi}\left(\frac{\Delta z}{a\xi} - \eta\right) \\
C_3 =& \frac{\partial}{\partial \xi}C_1 = -\frac{2}{\xi^3}\left(\frac{\Delta z}{a}\right)^2 + \frac{2\eta}{\xi^2}\frac{\Delta z}{a} - \frac{2\eta^2}{\xi^3} \\
C_4 =& \frac{\partial}{\partial \xi}C_2 = -\frac{4\Delta z}{a\xi^3} + \frac{2\eta}{\xi^2} \\
C_5 =& \sqrt{C_1^2 - C_2^2} \\
C_6 =& C_1 C_3 - C_2 C_4 \\
C_7 =& \sqrt{C_1 + C_5} \\
C_8 =& C_3 + \frac{C_6}{C_5}.
\end{aligned} \tag{B.12}$$

C. Potential calculations

The module in GranFilm which calculates the potential from the expansion coefficients needed to be extended to also include the case of prolate spheroids. In this section some of the mathematics of this implementation is detailed.

C.1. Evaluating the potential

When the multipole expansion coefficients have been found, the potential may be evaluated explicitly from Eqs. (4.32)–(4.33). Using the dimensionless multipole coefficients $\widehat{A}_{\ell m}^{(i)}$ and $\widehat{B}_{\ell m}^{(i)}$ introduced in Appendix A, these equations now take the form

$$
\begin{aligned}
\psi_i(\mathbf{r}) =& \delta_{i,1}\psi_{inc}(\mathbf{r}) + \psi_0^{(i)} + E_0 \sideset{}{'}\sum_{\ell m} R_{\perp,1}^{\ell+2} \widehat{A}_{\ell m}^{(i)} \Big[\widetilde{Z}_\ell^m(\xi_\mu, a) Y_\ell^m(\arccos\eta_\mu, \phi_\mu) \\
&+ (-1)^{\ell+m} \mathcal{R}_i \widetilde{Z}_\ell^m(\xi_{\bar{\mu}}, a) Y_\ell^m(\arccos\eta_{\bar{\mu}}, \phi_{\bar{\mu}}) \Big] \\
&+ E_0 \sideset{}{'}\sum_{\ell m} R_{\perp,1}^{-\ell+1} \widehat{B}_{\ell m}^{(i)} \Big[\widetilde{X}_\ell^m(\xi_\mu, a) Y_\ell^m(\arccos\eta_\mu, \phi_\mu) \\
&+ (-1)^{\ell+m} \mathcal{R}_i \widetilde{X}_\ell^m(\xi_{\bar{\mu}}, a) Y_\ell^m(\arccos\eta_{\bar{\mu}}, \phi_{\bar{\mu}}) \Big],
\end{aligned}
\tag{C.1}
$$

for a region i above the substrate and

$$
\begin{aligned}
\psi_{i+1}(\mathbf{r}) =& \delta_{i,1}\psi_{tr}(\mathbf{r}) + \psi_0^{(i+1)} \\
&+ \mathcal{T}_i E_0 \sideset{}{'}\sum_{\ell m} \Big[R_{\perp,1}^{\ell+2} \widehat{A}_{\ell m}^{(i)} \widetilde{Z}_\ell^m(\xi_\mu, a) \\
&+ R_{\perp,1}^{-\ell+1} \widehat{B}_{\ell m}^{(i)} \widetilde{X}_\ell^m(\xi_\mu, a) \Big] Y_\ell^m(\arccos\eta_\mu, \phi_\mu).
\end{aligned}
\tag{C.2}
$$

for a region $i+1$ below the substrate.

When solving the system of equations for the multipole expansion coefficients, it was only necessary to consider the equations for the cases $m = 0, 1$, as discussed in section 4.9. This was due to the symmetry in the matrix elements with respect to m, which made the case $m = -1$ redundant.

When calculating the potential, however, all values of m must be considered. Thus, the functions $\widetilde{X}_\ell^m(\xi, a)$ and $\widetilde{Z}_\ell^m(\xi, a)$, the spherical harmonics $Y_\ell^m(\arccos\eta, \phi)$, as well as the multipole coefficients, for $m = -1$ are needed. It can be shown, using Eq. (4.10), that the two first functions are independent of a change of sign in m, *i.e.* that

$$\begin{aligned} \widetilde{X}_\ell^m(\xi, a) &= \widetilde{X}_\ell^{-m}(\xi, a) \\ \widetilde{Z}_\ell^m(\xi, a) &= \widetilde{Z}_\ell^{-m}(\xi, a). \end{aligned} \tag{C.3}$$

The spherical harmonics for $m = -1$ are found from Eqs. (4.10)–(4.11), and can be written

$$\begin{aligned} Y_\ell^0(\arccos\eta, \phi) &= \sqrt{\frac{2\ell+1}{4\pi}} P_\ell^0(\eta) \\ Y_\ell^{-1}(\arccos\eta, \phi) &= \sqrt{\frac{2\ell+1}{4\pi\ell(\ell+1)}} P_\ell^1(\eta) e^{-i\phi} \\ Y_\ell^1(\arccos\eta, \phi) &= -\sqrt{\frac{2\ell+1}{4\pi\ell(\ell+1)}} P_\ell^1(\eta) e^{i\phi} \end{aligned} \tag{C.4}$$

for the three cases $m = 0, -1, 1$. Using Eqs. (C.3)–(C.4) and (A.2)–(A.3), it can now be shown that the dimensionless multipole coefficients have the following symmetry in m

$$\begin{aligned} \widehat{A}_{\ell,-1}^{(i)} &= -e^{i2\phi_0} \widehat{A}_{\ell,1}^{(i)} \\ \widehat{B}_{\ell,-1}^{(i)} &= -e^{i2\phi_0} \widehat{B}_{\ell,1}^{(i)}. \end{aligned} \tag{C.5}$$

The constant terms of the potential are calculated from Eq. (4.74), which, using the dimensionless coefficients, takes the form

$$
\begin{aligned}
&\left[\psi_0^{(2s+1)} - \psi_0^{(2s-1)}\right] \\
&= \frac{E_0 \chi_s R_{\perp,1}}{2\sqrt{\pi}} \sum_{\ell'=1}^{M} \zeta_{0\ell'}^{0} \chi_s^{-\ell'-2} \left[\widehat{A}_{\ell' 0}^{(2s-1)} \mathcal{I}_{0\ell'}^{0(2s-1)}(t_r^{(s)}, \xi_{0,s}) \right. \\
&\left. - \widehat{A}_{\ell' 0}^{(2s+1)} \mathcal{I}_{0\ell'}^{0(2s+1)}(t_r^{(s)}, \xi_{0,s}) \right] \\
&+ \frac{E_0 \chi_s R_{\perp,1}}{2\sqrt{\pi}} \sum_{\ell'=1}^{M} \zeta_{0\ell'}^{0} \chi_s^{\ell'-1} \left[\widehat{B}_{\ell' 0}^{(2s-1)} \mathcal{K}_{0\ell'}^{0(2s-1)}(t_r^{(s)}, \xi_{0,s}) \right. \\
&\left. - \widehat{B}_{\ell' 0}^{(2s+1)} \mathcal{K}_{0\ell'}^{0(2s+1)}(t_r^{(s)}, \xi_{0,s}) \right] \\
&+ \delta_{s1} R_{\perp,s} E_0 \cos\theta_0 \left(\frac{\varepsilon_1}{\varepsilon_2} - 1 \right) \left\{ \frac{1}{\sqrt{3}} \zeta_{01}^{0} Q_{01}^{0}(-1, t_r^{(1)}) \right. \\
&\left. + t_r^{(1)} \left[1 - \zeta_{00}^{0} Q_{00}^{0}(-1, t_r^{(1)}) \right] \right\} \\
&\forall \quad s = 1, 2, 3, ..., S.
\end{aligned}
\tag{C.6}
$$

C.2. Analytic expression for the potential derivatives

The normal derivatives of the potential at an interface are calculated by differentiating Eqs. (4.32)–(4.33) with respect to ξ. This yields the following expressions

$$
\begin{aligned}
\frac{\partial}{\partial\xi}\psi_i(\mathbf{r}) = \delta_{i,1}\frac{\partial}{\partial\xi}\psi_{inc}(\mathbf{r})
&+ E_0 \sideset{}{'}\sum_{\ell m} R_{\perp,1}^{\ell+2}\widehat{A}_{\ell m}^{(i)}\Big\{\Big[\frac{\partial}{\partial\xi_\mu}\widetilde{Z}_\ell^m(\xi_\mu,a)\frac{\partial\xi_\mu}{\partial\xi}Y_\ell^m(\arccos\eta_\mu,\phi_\mu)\\
&+ \widetilde{Z}_\ell^m(\xi_\mu,a)\frac{\partial}{\partial\eta_\mu}Y_\ell^m(\arccos\eta_\mu,\phi_\mu)\frac{\partial\eta_\mu}{\partial\xi}\Big]\\
&+ (-1)^{\ell+m}\mathcal{R}_i\Big[\frac{\partial}{\partial\xi_{\bar\mu}}\widetilde{Z}_\ell^m(\xi_{\bar\mu},a)\frac{\partial\xi_{\bar\mu}}{\partial\xi}Y_\ell^m(\arccos\eta_{\bar\mu},\phi_{\bar\mu})\\
&+ \widetilde{Z}_\ell^m(\xi_{\bar\mu},a)\frac{\partial}{\partial\eta_{\bar\mu}}Y_\ell^m(\arccos\eta_{\bar\mu},\phi_{\bar\mu})\frac{\partial\eta_{\bar\mu}}{\partial\xi}\Big]\Big\}\\
&+ E_0 \sideset{}{'}\sum_{\ell m} R_{\perp,1}^{-\ell+1}\widehat{B}_{\ell m}^{(i)}\Big\{\Big[\frac{\partial}{\partial\xi_\mu}\widetilde{X}_\ell^m(\xi_\mu,a)\frac{\partial\xi_\mu}{\partial\xi}Y_\ell^m(\arccos\eta_\mu,\phi_\mu)\\
&+ \widetilde{X}_\ell^m(\xi_\mu,a)\frac{\partial}{\partial\eta_\mu}Y_\ell^m(\arccos\eta_\mu,\phi_\mu)\frac{\partial\eta_\mu}{\partial\xi}\Big]\\
&+ (-1)^{\ell+m}\mathcal{R}_i\Big[\frac{\partial}{\partial\xi_{\bar\mu}}\widetilde{X}_\ell^m(\xi_{\bar\mu},a)\frac{\partial\xi_{\bar\mu}}{\partial\xi}Y_\ell^m(\arccos\eta_{\bar\mu},\phi_{\bar\mu})\\
&+ \widetilde{X}_\ell^m(\xi_{\bar\mu},a)\frac{\partial}{\partial\eta_{\bar\mu}}Y_\ell^m(\arccos\eta_{\bar\mu},\phi_{\bar\mu})\frac{\partial\eta_{\bar\mu}}{\partial\xi}\Big]\Big\},
\end{aligned}
\tag{C.7}
$$

for a region i above the substrate and

$$
\begin{aligned}
\frac{\partial}{\partial\xi}\psi_{i+1}(\mathbf{r}) =\delta_{i,1}\frac{\partial}{\partial\xi}\psi_{tr}(\mathbf{r})
&+ \mathcal{T}_i E_0 \sideset{}{'}\sum_{\ell m}\Big\{R_{\perp,1}^{\ell+2}\widehat{A}_{\ell m}^{(i)}\Big[\frac{\partial}{\partial\xi_\mu}\widetilde{Z}_\ell^m(\xi_\mu,a)\frac{\partial\xi_\mu}{\partial\xi}Y_\ell^m(\arccos\eta_\mu,\phi_\mu)\\
&+ \widetilde{Z}_\ell^m(\xi_\mu,a)\frac{\partial}{\partial\eta_\mu}Y_\ell^m(\arccos\eta_\mu,\phi_\mu)\frac{\partial\eta_\mu}{\partial\xi}\Big]\\
&+ R_{\perp,1}^{-\ell+1}\widehat{B}_{\ell m}^{(i)}\Big[\frac{\partial}{\partial\xi_\mu}\widetilde{X}_\ell^m(\xi_\mu,a)\frac{\partial\xi_\mu}{\partial\xi}Y_\ell^m(\arccos\eta_\mu,\phi_\mu)\\
&+ \widetilde{X}_\ell^m(\xi_\mu,a)\frac{\partial}{\partial\eta_\mu}Y_\ell^m(\arccos\eta_\mu,\phi_\mu)\frac{\partial\eta_\mu}{\partial\xi}\Big]\Big\}.
\end{aligned}
\tag{C.8}
$$

for a region $i+1$ below the substrate.